KERNFORSCHUNGSANLAGE JÜLICH GmbH

Institut für Medizin

The Analysis of Auger Electrons Released Following the Decay of Radioisotopes and Photoelectric Interactions and their Contribution to Energy Deposition

by

J.L. Humm

Jül-1932
June 1984
ISSN 0366-0885

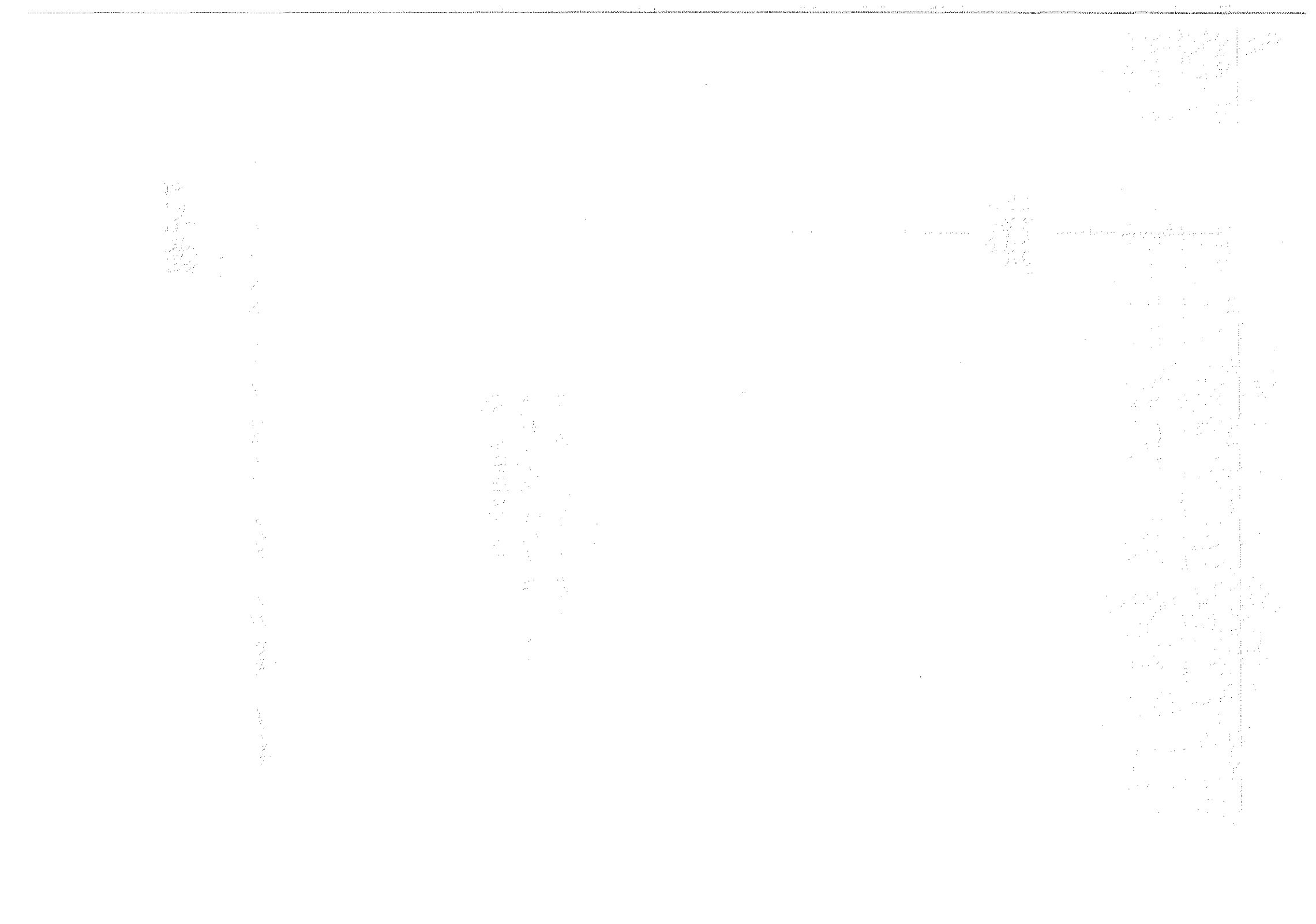

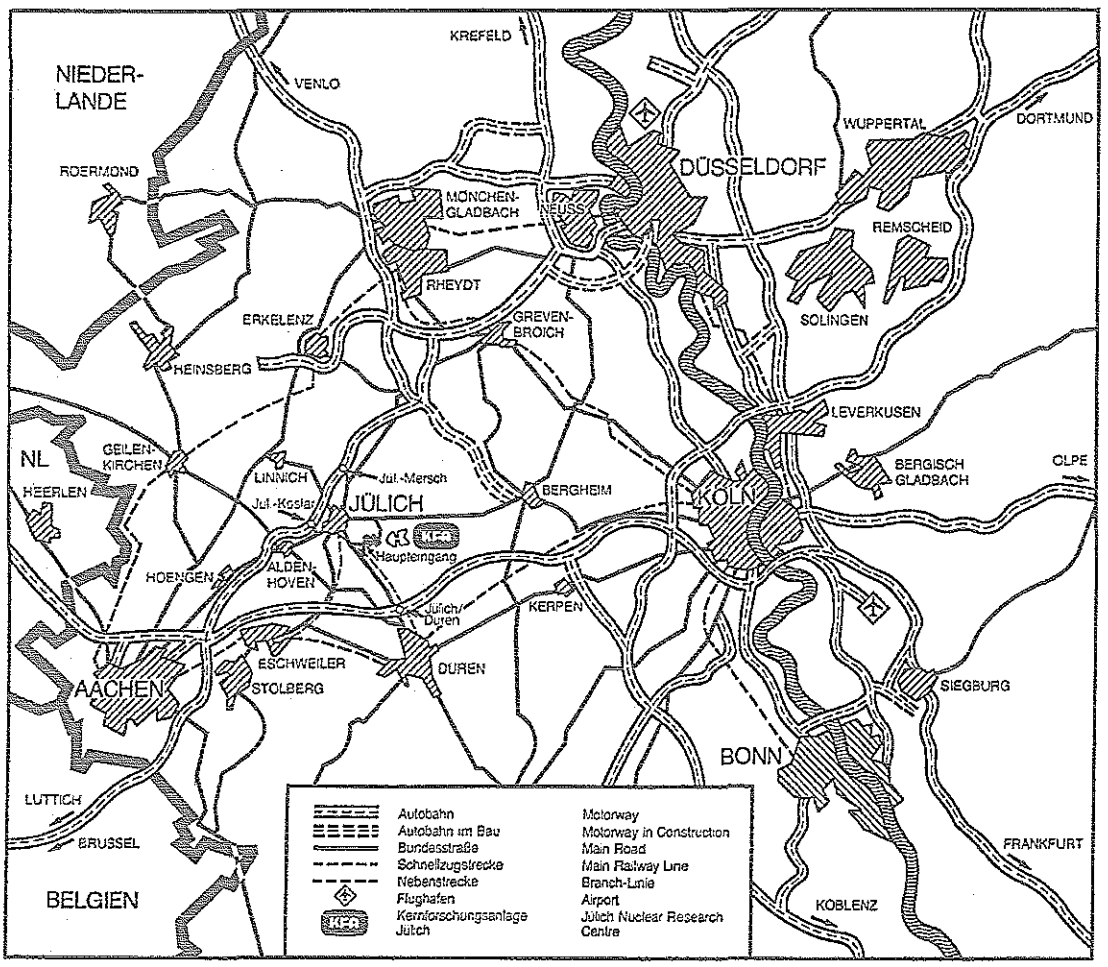

Als Manuskript gedruckt

Berichte der Kernforschungsanlage Jülich – Nr. 1932
Institut für Medizin Jül - 1932

Zu beziehen durch: ZENTRALBIBLIOTHEK der Kernforschungsanlage Jülich GmbH
Postfach 1913 · D-5170 Jülich (Bundesrepublik Deutschland)
Telefon: 02461/610 · Telex: 833556-0 kf d

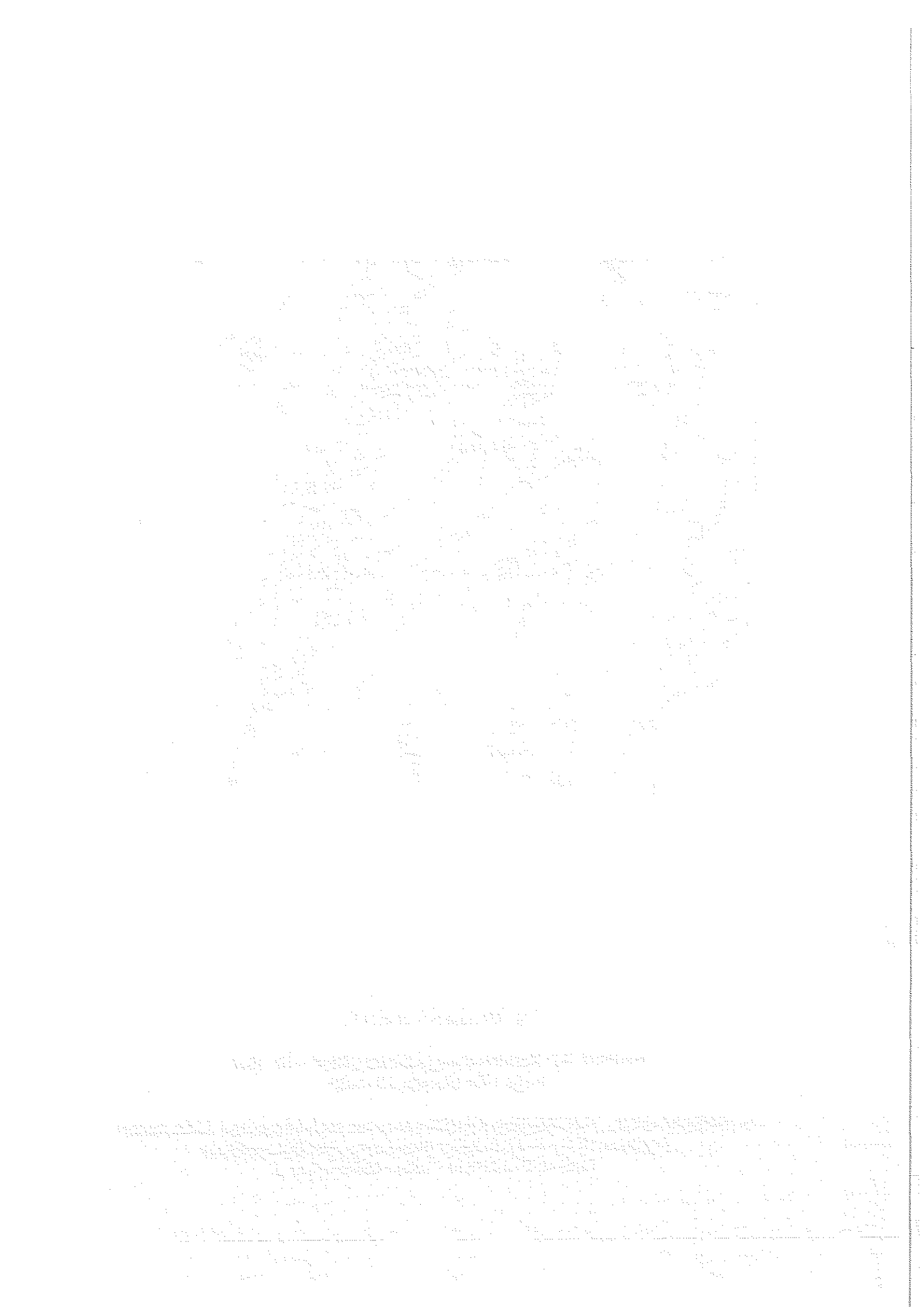

The Analysis of Auger Electrons Released Following the Decay of Radioisotopes and Photoelectric Interactions and their Contribution to Energy Deposition

by

J.L. Humm

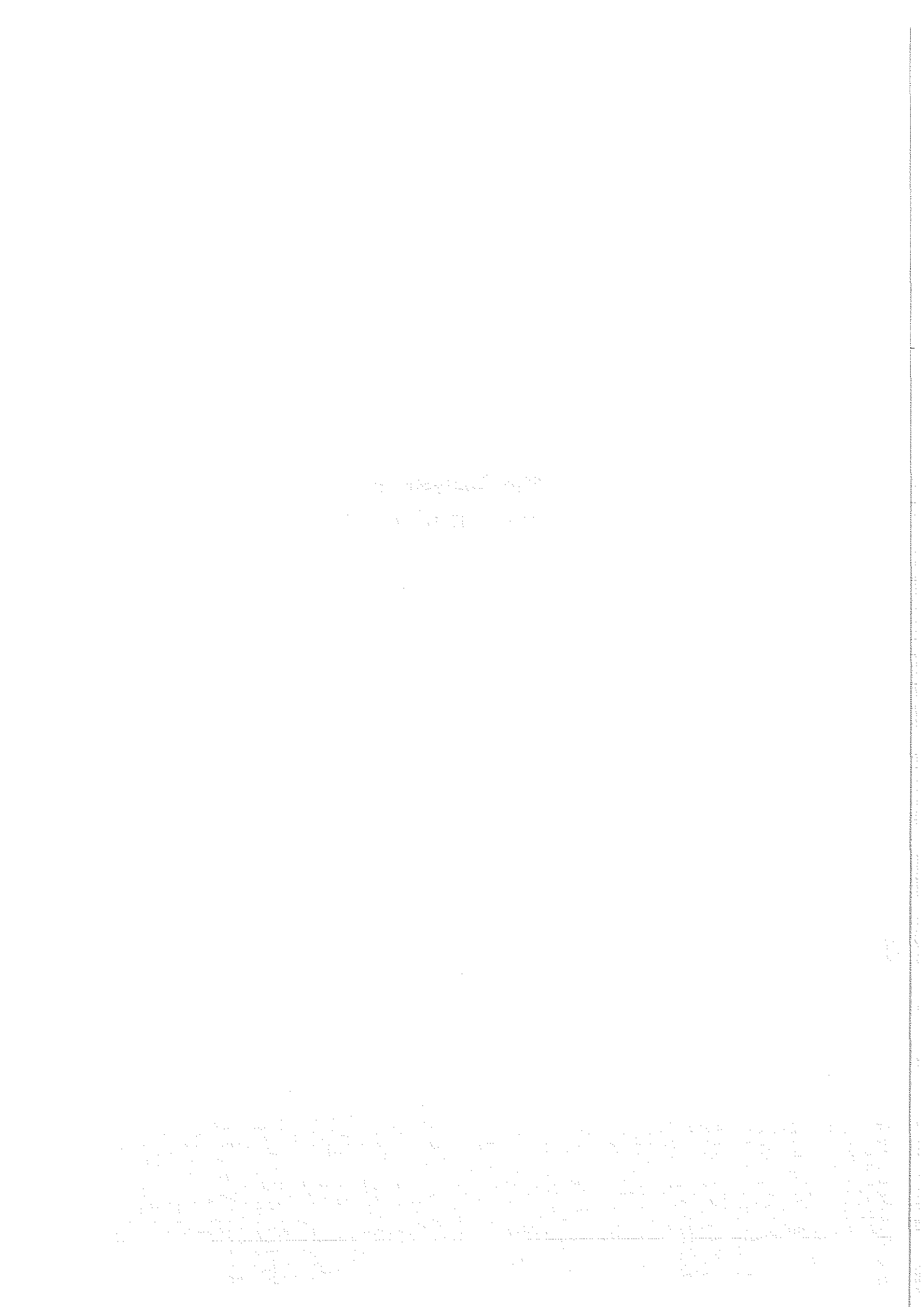

THE ANALYSIS OF AUGER ELECTRONS RELEASED FOLLOWING THE DECAY OF RADIOISOTOPES AND PHOTOELECTRIC INTERACTIONS AND THEIR CONTRIBUTION TO ENERGY DEPOSITION

J.L.HUMM

ABSTRACT

This work is a study of the microdosimetry of Auger electrons resulting from inner shell ionization phenomena in atoms of significance in radiation biology and medicine.

Inner shell atomic vacancies are produced in radionuclides which decay by electron capture or internal conversion or can be produced by the photoelectric effect. The result of creating an inner shell vacancy in an atom is a vacancy cascade process in which a large number of low energy Auger electrons are released. Auger emitters when present at the radiosensitive structures of biological materials have been shown to be highly radiotoxic, although little is known about the energy deposition around such sites.

The theoretical part of this work includes the use of a Monte-Carlo technique to calculate discrete Auger electron spectra for the electron capture decaying radionuclides: iodine-125, iodine-123, iron-55 and copper-64 and following photoelectric interactions in phosphorus and argon. The individual spectra for 10,000 photoelectric interactions were used as the basis for local energy deposition calculations. Not only the mean energy deposition has been calculated but also its fluctuation around the mean where it is shown that the mean energy deposited may be quite untypical of the energy deposition from single disintegrations.

Further the possibility of selective photoelectric absorption in phosphorus bound DNA and DNA labelled with cold iodine is investigated. Using argon as a substitute for phosphorus to study this problem further, energy deposition measurements have been performed to examine the pattern of energy deposition and the mean energy deposition, $\bar{\epsilon}_F$, at photon energies just above and below the K-edge of argon. The problems encountered in such microdosimetric measurements are discussed in detail and in particular an anomalous double peak phenomenon observed in proportional counters employing a helix grid electrode is reported.

LIST OF CONTENTS

A historical review of the effects of Auger electron cascades in biology and medicine

Although the Auger effect was discovered as early as 1925 by Pierre Auger it was not until fairly recently that the possible implications of Auger electron emission for radiation biology has been appreciated. In 1969 it was reported by Ertl and Feinendegen that the electron and internal conversion decaying radionuclide, iodine-125, when incorporated into the DNA in the form of the thymidine precursor IUdR, was found to exhibit a far greater radiotoxicity than to be expected from considerations of absorbed dose alone, (between 5-10 times higher than tritium labelled thymidine). Since this time a considerable amount of work investigating single and double strand breaks and cell death has been performed : Burki et al 1973, Krisch 1972, Krisch et al 1976, Tisljar et al 1978 etc. confirming the high effectiveness of ^{125}I when incorporated into the DNA of cells.

Considerable interest also quickly began to develop for other Auger emitting radionuclides which could be incorporated into the cell nucleus. Some work has already been performed with ^{64}Cu (Apelgot et al 1980), ^{55}Fe (Reincke et al 1978), ^{77}Br (Kassis et al 1982) and there have been proposals to use others, e.g. ^{123}I (L.E.Feinendegen - private communication).

Some experimental research has also been performed investigating the effects of Auger electron cascades induced by the photoelectric effect. Halpern and Stocklin 1974 irradiated the thymidine precursor BUdR with X-rays of energies just above and below the K-edge of bromine. Using ESR techniques they detected a marked increase in the radical concentration as the bromine edge was traversed. Further investigations carried out by Diehn,

Halpern and Stocklin 1976 using the metalloenzyme carbonic anhydrase, an enzyme which contains zinc as an active centre. Irradiating with photon energies above and below the K-edge of zinc showed a sudden increase in enzyme inactivation accompanied by an increase in the zinc release as the K-edge of zinc was traversed.

Goodhead, Cox and Thacker 1980, 1981 of the MRC, Harwell in their low energy X-ray work looked for a selective photoelectric effect in phosphorus. It was thought that because phosphorus is situated in the backbone of DNA, where it occupies about 10% by weight, that it might be a selective target for X-ray absorption and hence for the production of strand breaks and perhaps cell death. Irradiating several different mammalian cell lines with monochromatic photons of energies just above (titanium-K_α 4.55 keV) and below (aluminium-K_α 1.55 keV) the K-edge of phosphorus (2.145 keV) Goodhead and collegues did not detect a significant effect.

To summarize, several works have been concerned with the role of Auger electrons in radiation biology and medicine whether induced by radionuclide decay or by the photoelectric effect. Several questions remain unresolved regarding the contribution to biological damage from Auger electron cascades related to problems of local energy deposition and the sensitivity of the immediate neighbourhood of the cascade sites. It is clear that much work is still to be performed in this field if an exact quantitative understanding of the effects is to be achieved and it is hoped that this dissertation will provide a useful contribution to this complicated and much debated region of study.

Survey of the content of the thesis

Besides the detailed theoretical work on the energy deposition of ^{125}I by Charlton and Booz 1978, 1981, and Gavron and Feige 1975, very little information has been published on the microdosimetry of Auger electrons released by decaying radionuclides incorporated into biological matter or induced by photoelectric interactions. It was the aim of this thesis therefore to investigate relevant areas of this important field where present data is lacking.

To simplify presentation the thesis has been divided into three parts :

1/ Auger electron emission following the decay of radionuclides.
2/ Auger electron emission induced by the photoelectric effect.
3/ Energy deposition measurements for photoelectric induced vacancy cascades in argon.

Part I is concerned with the development and extention of the Monte-Carlo technique developed for ^{125}I by Charlton and Booz 1978, 1981 to calculate the electron and photon energy spectra for other radionuclides of importance in radiation biology and medicine. Here the computational techniques to calculate electron energy spectra for the radionuclides : ^{125}I, ^{123}I, ^{55}Fe and ^{64}Cu are described and used to provide new energy deposition data for these isotopes.

Part II is a continuation of this work for photoelectric induced cascades. Using atomic photoelectric cross section data and the atomic constitutions of DNA, cell nuclei and tissue equivalent materials, the possibility of selective absorption effects is discussed, with particular emphasis on the problems of DNA bound phosphorus. Using a Monte-Carlo method photon interactions in

phosphorus have been simulated, the Auger electron energy spectrum calculated and their local energy deposition evaluated for a series of photon energies. The results of additional calculations are presented for Monte-Carlo simulated photoelectric induced vacancy cascades in argon. It is shown that the Auger electron spectra produced by photoelectric interactions in the corresponding shells of argon and phosphorus are similar hence making argon a suitable model in experimental energy deposition studies for the radiation biologically relevant atom phosphorus.

Part III contains the experimental work performed in the thesis . Using an argon filled proportional counter, energy deposition spectra were measured for photoelectric interactions within the chamber with a series of photon energies above and below the K absorption edge of argon in simulated tissue equivalent volume diameters between 0.5 - 8 μm. The experimental techniques and difficulties are described in detail and an anomalous double peak phenomenon is reported when calibrating with low energy photons a spherical Rossi counter with helical grid electrode.

PART I

AUGER ELECTRON EMISSION FOLLOWING THE DECAY OF RADIONUCLIDES

1 Physical properties of radionuclide decay

1.1 Decay schemes

Incorporated radionuclides are at present of considerable interest in nuclear medicine because of their high radiotoxicity. Incorporation has a particular advantage over external irradiation in that the effect is localized and contained within a small region around the isotope. The discussion here will be limited to 4 radionuclides : ^{125}I, ^{123}I, ^{55}Fe, ^{64}Cu on which the bulk of the work in this part of the thesis has been concentrated.

1.1.1 Iodine-125

In figure 1 is the decay scheme for ^{125}I. The decay occurs in two stages : first a 100% transition by electron capture to a metastable state of tellurium (mean life 1.6×10^{-9} s) followed by gamma emission (7%) or internal conversion (93%) to the ground state.

In the process of electron capture an electron is taken from one of the atomic shells leaving on inner shell vacancy. The energy associated with this vacancy is lost by a series of inner shell atomic transitions. Figure 2 shows an example of one of the many de-excitation pathways of the tellurium atom following the decay of ^{125}I by K capture. Such an atomic de-excitation process results generally in the emission of many Auger electrons and possibly photons from electron transitions to the deeper lying shells particularly the K shell. After this atomic de-excitation, which is extremely rapid ($\simeq 10^{-15}$s, Cooper 1942), the tellurium nucleus is still in a highly excited state and decays after a further 10^{-9} s predominently by internal conversion producing another inner shell vacancy and hence a further cascade of Auger electron emission.

For 93% of the ^{125}I decays electron capture is followed by internal conversion and two vacancy cascades result. In the remaining 7% of decays corresponding to

Figure 1
Decay scheme for ^{125}I.

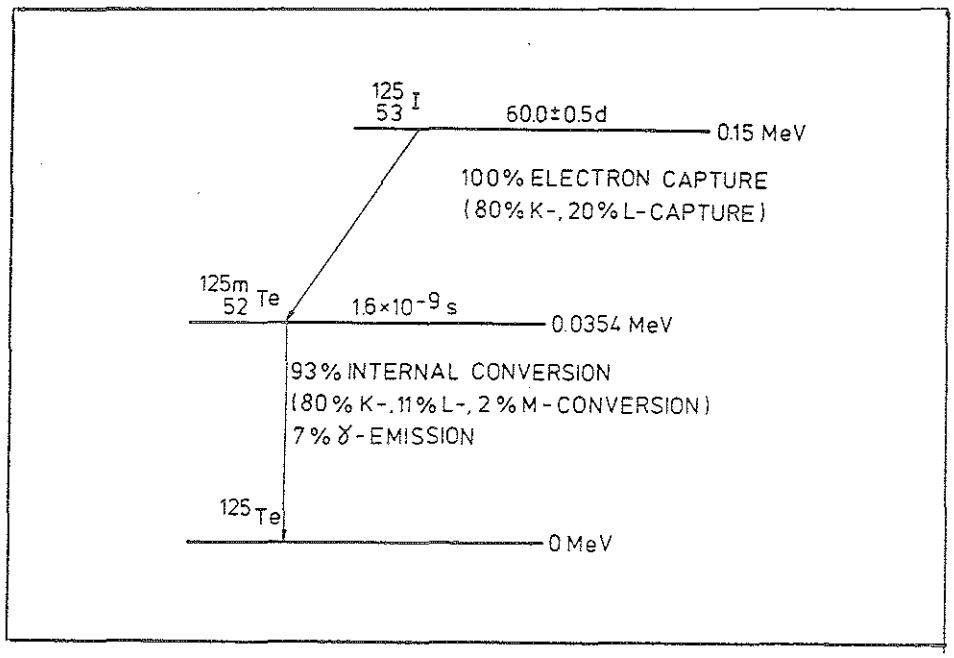

Figure 2
Electron cascade for tellurium following the decay by electron capture of ^{123}I or ^{125}I.

○ vacancy in the atom

⊗ filled vacancy

→ Auger electron emission

⇝ photon emission

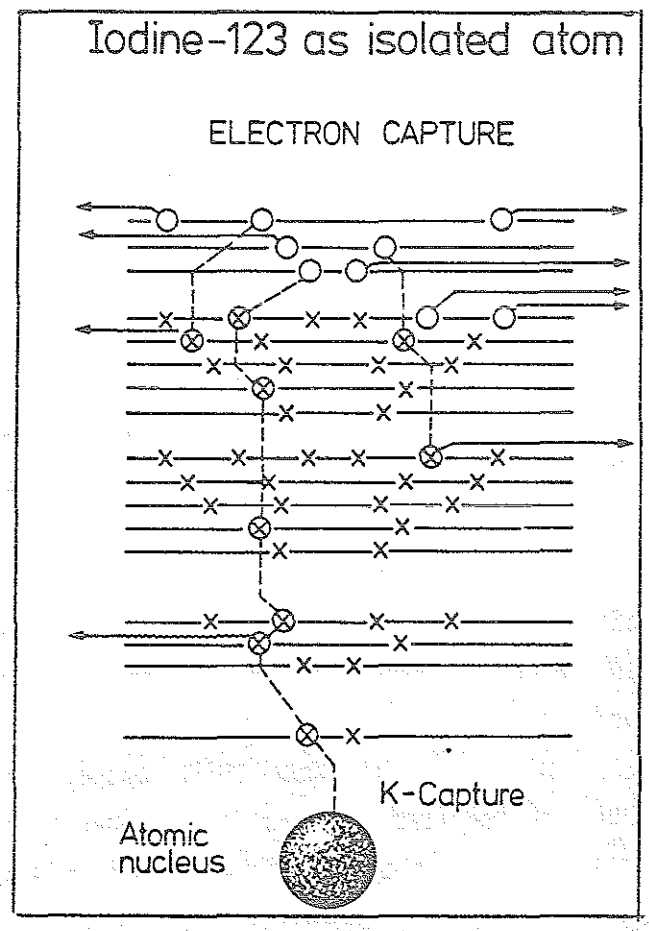

electron capture and gamma emission a single vacancy cascade occurs.

1.1.2 Iodine-123

The decay of ^{123}I resembles that for ^{125}I with the additional complexity that the electron capture decay branches to 7 possible metastable levels of the tellurium nucleus (figure 3). These metastable tellurium levels decay by either internal conversion or gamma emission, the relative proportions of which depend on the level of excitation and the multipolarity of the transition. The total percentage of internal conversion from all levels amounts to only 18% of all decays. Therefore the probability for a second vacancy cascade for the radioisotope ^{123}I is considerably smaller than for ^{125}I. This will be shown late to have an important effect on the Auger spectrum when compared to the case of ^{125}I.

1.1.3 Iron-55

^{55}Fe decays by 100% electron capture to the ground state of manganese, (see figure 4). For this radioisotope therefore all decays result in a single vacancy cascade process.

1.1.4 Copper-64

For ^{64}Cu there are two electron capture decay pathways, one directly to the ground state of nickel (40.5%) and a second to a metastable state of nickel (0.6%) which predominently de-excites by gamma emission. The remaining 58.9% of the decays are by beta ray emission.

Figure 3
Decay scheme for ^{123}I.

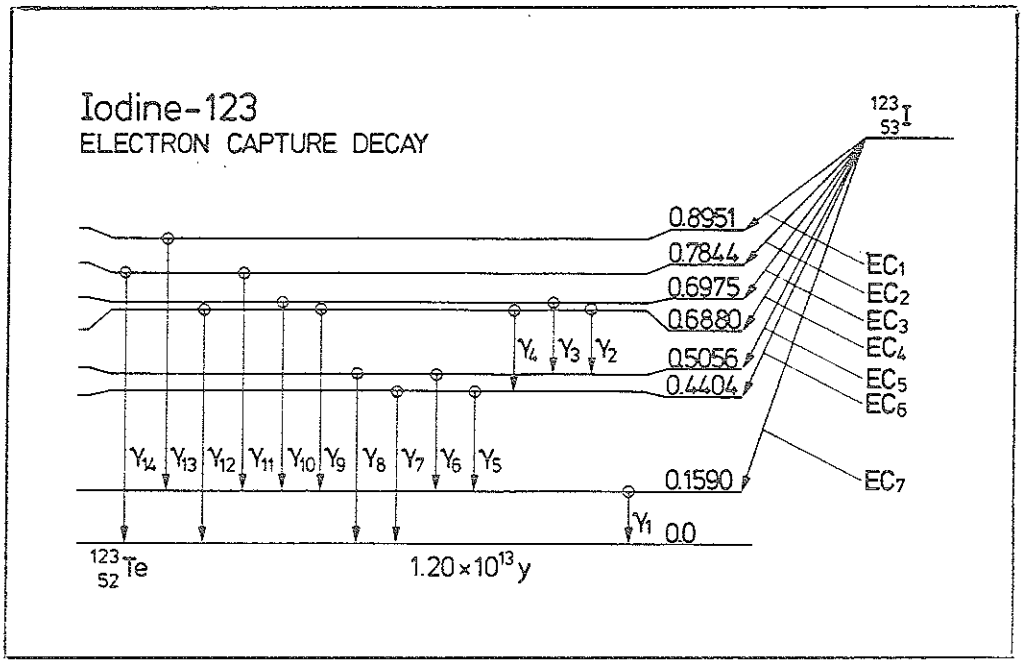

Figure 4
Decay scheme for ^{55}Fe.

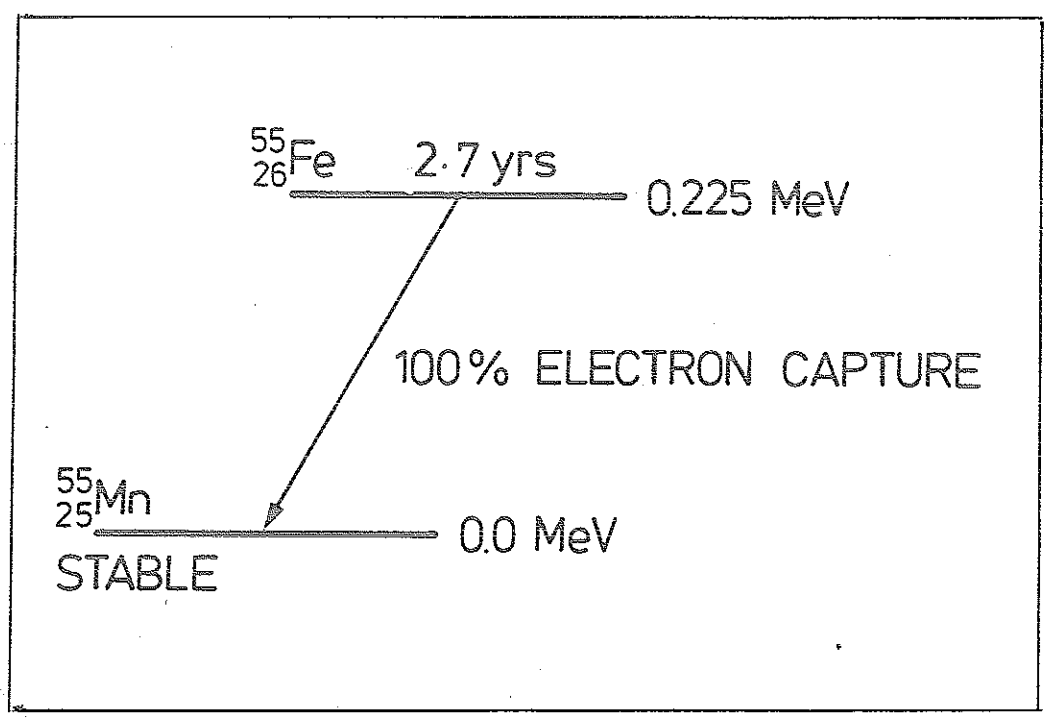

Figure 5
Decay scheme for ^{64}Cu

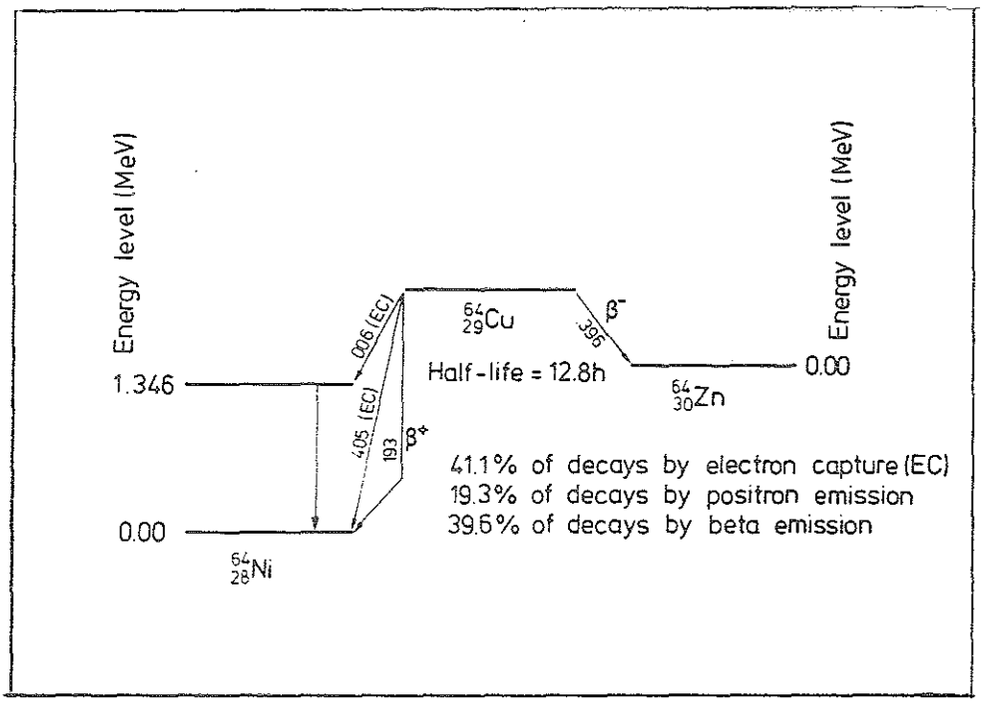

1.2 Beta decay

1.2.1 Type of processes

Under beta decay are included all those nuclear reactions in which the nuclear charge changes by one. This encompasses three types of decay : beta-minus where a neutron is converted to a proton with the emission of an electron and antineutrino, beta-plus (the reverse process) where a proton transforms to a neutron with the emission of a positron and a neutrino, and finally electron capture where an orbital electron is captured by a nuclear proton resulting in a neutron and the emission of a neutrino. In beta-minus decay the nuclear charge is increased by one, in beta-plus and electron capture it is reduced by one. The latter two processes are normally in competition. Electron capture becomes the only decay process when the mass difference between the mother and daughter nuclei is less than $2m_e$ where m_e is the electron mass, Evans 1955, as is the case for the radioisotopes : ^{125}I, ^{123}I and ^{55}Fe. For ^{64}Cu electron capture competes with beta-plus decay to the nickel daughter. Also a certain percentage of the disintegrations go by beta-minus decay to zinc (figure 5).

Radionuclides which decay 100% by electron capture produce an electron spectrum comparising of Auger electrons only. For ^{64}Cu the electron energy emission spectrum consists of the superposition of an Auger electron energy spectrum, a beta-plus spectrum and because of branching a beta-minus spectrum as well.

1.2.2 Shape of electron and positron spectra

Since for energy deposition purposes the charge difference between electron and positron can be neglected the beta-minus, beta-plus spectra have been combined.

The combination must be undertaken however after the spectra have been individually calculated since the nuclear Coulomb factor and electron screening factors

both introduce distortions which influence the beta-plus and beta-minus spectrum shapes differently.

For allowed transitions taking screening into account the shape of a beta spectrum [1] is given by

$$N(W) = F(Z, W-V_0) \left[(W-V_0)^2 - 1\right]^{1/2} \cdot (W-V_0)(W_0-W)^2 \quad (1)$$

where $N(W)$ = probability for the emission of a beta ray of total energy W,

W = total energy of the beta particle (in mc^2 units),

V_0 = screening potential due to atomic electrons

$V_0 = 1.13\,\alpha^2\,|Z|^{4/3}$ where α is the fine structure constant $1/137$,

W_0 = maximum total beta particle energy,

$F(Z, W-V_0)$ = Fermi function modified for screening potential due to the orbital electrons.

The beta-plus, beta-minus spectra for ^{64}Cu are calculated using equation 1., then combined to a single spectrum by adding the N(W) components at each energy interval W. For further details on the calculation of the beta spectra for ^{64}Cu the reader is referred to Appendix 1.

1.3 Electron capture

The orbital electron of an atom can be represented by a wavefunction, which partially overlaps with the nucleus. In electron capture an electron during its presence in the nucleus interacts with a nuclear proton to form a neutron, an antineutrino being emitted for energy conservation.

$$p^+ + e^- \longrightarrow n + \bar{\nu} \quad (2)$$

The probability of electron capture for an electron in a

[1] To calculate the shape of beta spectra see Marschall 1955 and Mantel 1972.

shell is a function of the degree of overlap between the electron from that shell with the nucleus. For the K shell electrons this overlap is greatest, the degree of overlap rapidly decreasing for the higher shells. The relative proportion of vacancies produced by electron capture in the individual sub-shells K, L1, L2, L3, M1 etc represent the distribution of initial vacancies in electron capture decaying radioisotopes and thus are needed to calculate the resulting Auger-electron cascades.

Relatively simple equations exist for the various electron capture ratios L1/K, L2/K, M1/K etc from which the relative electron capture probabilities of each sub-shell can be calculated, Bambynek et al 1977. Denoting the electron capture probabilities λ_K and λ_{L_1} for the K- and L1-shells, the probability ratio for L1 to K capture is given by equation (3)

$$\lambda_{L1}/\lambda_K = (n_{L1} q_L^2 \beta_{L1}^2 B_{L1}) / (n_K q^2{}_K \beta_K^2 B_K) \quad (3)$$

n_{L1} and n_K denote the relative occupation numbers of electrons in the L1 and K shells respectively where for closed shells n = 1,

$(q_{L1}/ q_K)^2 = \left(\frac{E_{EC} - E_{L1}}{E_{EC} - E_K} \right)^2$ where E_{EC}, the electron capture transition energy, is $Q_{EC} - E_y$ (for electron capture direct to the ground state $E_{EC} = Q_{EC}$)
E_y is the remaining excitation energy of the nucleus and E_K, E_{L1} are the electron binding energies of the K and L1 shells respectively.
β_x is the electron radial wavefunction amplitude
B_x is a correction factor taking into account effects of electron exchange and overlap.[2]
Equations for λ_{L1}/λ_K and all other ratios are entirely analogous.

[2]In this work all values used for β_x and B_x were from Bambynek et al 1977 and Behrens and Jänecke 1969.

For decay by 100% electron capture the sum of the probabilities for electron capture in each individual sub-shell is one.

$$\lambda_{EC} = \lambda_K + \lambda_{L1} + \lambda_{L2} + \ldots = 1 \qquad (4)$$

Using equations (3) and (4) the initial vacancy distributions for isotopes which decay by electron capture can be calculated. If the decay involves branching to different excitation levels of the daughter then each electron capture transition must be considered separately and normalized to the probability of their decay pathways.

1.4 Internal conversion

Internal conversion is a process whereby the excitation energy of a nucleus instead of being released in the form of gamma emission is transferred directly to an orbital electron, which is emitted with an energy E_{IC} equal to the excitation energy of the nucleus E_γ minus the binding energy of the released electron E_B, (Segre and Helmholz 1949, Emery 1975)

$$E_{IC} = E_\gamma - E_B \qquad (5)$$

The process of internal conversion occurs in competition with gamma decay the relative proportions of the two processes being given by the total conversion coefficient, α , where

$$\alpha = \frac{N_e}{N_\gamma} = \frac{\text{Total number of emitted electrons in filling}}{\text{Total number of emitted gamma rays in filling}}$$

$$\frac{\text{N vacancies}}{\text{N vacancies}} \qquad (6)$$

$$\text{and } \alpha = \alpha_K + \alpha_{L1} + \alpha_{L2} + \ldots \qquad (7)$$

where α_K, α_{L1} etc are the partial conversion coefficients for the individual sub-shells.

As with electron capture the magnitude of a vacancy cascade induced by internal conversion will depend on the individual sub-shell in which the initial vacancy is produced. It is therefore necessary to know the initial vacancy distribution for each internal conversion decaying radionuclide. The partial conversion coefficients are tabulated by Rösel & Fries 1978 and Hager & Seltzer 1968 per sub-shell according to the energy and multipolarity of the transition. The multipolarity of a transition is often given in tables of isotopes, Lederer and Shirley 1978, when known. Some transitions consist of admixtures of two different multipolarities, the most common of which is the admixture magnetic dipole (M1) and electric quadrupole (E2). In this case the sub-shell internal conversion coefficients can be obtained using the formula,

$$\alpha_K = \frac{\alpha_K (M1) + \delta^2 \alpha_K (E2)}{1 + \delta^2} \qquad (8)$$

where δ^2 is called the mixing ratio and is equal to the ratio E2/M1, Dillmann and Van der Lage 1975, Chu et al 1964.

Of particular concern here are the radioisotopes ^{125}I and ^{123}I which after decay by electron capture remain in a highly excited metastable state of tellurium. For ^{125}I this state is a singlet, for ^{123}I many excitation levels exist (figure 3). In both cases the excited tellurium nucleus can decay by either gamma emission or internal conversion. For ^{125}Te the total conversion coefficient $\alpha = 93/7$, Dillmann and Van der Lage 1975. For ^{123}Te the value of α depends on the excitation energy and multipolarity of each level, therefore the partial conversion coefficients must be calculated separately for each excitation level.

1.5 Radiative transitions

A radionuclide which has undergone electron capture or internal conversion will be left with an inner shell vacancy. This vacancy represents a high atomic excitation energy which can be decreased by an electron transition from any higher shell to fill the deeper lying vacancy. If the energy of this transition is emitted as an X ray photon it is called a radiative transition. If the energy gained by the transition is emitted in the form of an electron it is referred to as a non-radiative transition (see section 1.6).

In a radiative transition the energy of the emitted photon $h\nu$ is

$$h\nu = \Delta E = E_1 - E_2 \qquad (9)$$

where E_1 is the energy level of the filled vacancy and E_2 the energy level from which the electron has come to fill it. A list of the probabilities and energies of radiative transitions for all elements is given in Storm and Israel 1970. Since the speed of radiative transitions is proportional to $(\Delta E)^{-3}$ and non-radiative transition proportional to ΔE, (Marmier 1965), the former predominate when ΔE is large i.e. for transitions to the deepest inner shell vacancies, in particular the K shell. Once the vacancies have reached the higher shells and the difference in energy levels become small non-radiative transitions are the faster and hence more probable.

A measure of the probability of radiative transitions to a vacancy in shell X is given by the fluorescence yield ω_X. For a vacancy in the K shell,

$$\omega_K = \sum \frac{(n_K)_i}{N_K} = \frac{n_{K_{\alpha_1}} + n_{K_{\alpha_2}} + n_{K_{\beta_1}} + \ldots}{N_K} \qquad (10)$$

where $(n_K)i$ = the number of photons of spectral line i emitted and N_K = the total number of vacancies created

and filled in the K shell.

The fluorescence yield depends on atomic number Z, becoming greater with increasing Z, e.g., for tellurium $\omega_K = 0.877$ whereas for phosphorus $\omega_K = 0.060$. Since for increasingly higher shells the fluorescence yield rapidly decreases, for inner vacancies in phosphorus radiative transitions are less important than non-radiative transitions. The same is true for the higher shells of tellurium, e.g., once the inner-shell vacancy of tellurium has reached the L shell, the fluorescence yields for L_1, L_2 and L_3 sub-shells are $\omega_1 = 0.041$, $\omega_2 = 0.074$ and $\omega_3 = 0.074$ respectively[3] (Krause 1979). In general radiationless transitions therefore form the predominant mechanism of atomic de-excitation once an inner shell vacancy has been introduced into an atom.

1.6 Non-radiative transitions [4]

A non-radiative transition is one where the energy gained by an electron transition, instead of being emitted as photon energy, is used for the emission of an electron. This process is known as the Auger effect and the emitted electron an Auger electron in honour of the discoverer Pierre Auger, 1921. The Auger process plays a particularly important role in the de-excitation of atoms after electron capture, internal conversion or the photoelectric effect (part II). Whereas the effect of a photon transition is to shift the initial K vacancy to a higher shell, an Auger transition in filling one vacancy produces another two, i.e. increases the charge on the atom by one. This progression of vacancies to the outer shells of an atom is a statistical process depending on the relative transition probabilities of all allowed radiative and radiationless transitions to each initiated

[3] It is usual to drop the L in the subscript when expressing fluorescence yields for the L sub-shells.

[4] Appendix 2 summarizes the conventional notation to classify Auger electrons.

vacancy. The relative Auger transition rates are given by Mc Guire 1975 and Chen, Crasemann and Mark 1979. Auger transitions are extremely fast (approx. 10^{-15} - 10^{-14}s) and vary only slightly with the transition energy ΔE. For $\Delta E \geq 10$ keV radiative transitions are of the same order of magnitude as non-radiative ones. However, for transitions between the outer shells of atoms where ΔE is small, they approach the rates of optical transitions (approx. 10^{-8}s) which are negligible in comparison with Auger-transition rates. Hence, for all shells except the K shell, radiationless transitions are in general the predominant processes of de-excitation for atoms with inner-shell vacancies.

The probability of an Auger transition to a K-shell vacancy is given by the Auger yield, a_K, which is defined in an analogous way to the fluorescence yield, i.e. by the number of Auger transitions to the K shell relative to the number of K-shell vacancies filled, Krause 1979. Together the sum of the fluorescence and Auger yields for the K shell is one, i.e., the Auger yield is given by $1-\omega_K$.

Above the K shell it is usual to distinguish between Auger and Coster-Kronig transitions. The Coster-Kronig effect is an Auger process in which the electron transition occurs between two sub-shells of the same principal shell. For example, in the Coster-Kronig transition $L_1L_3M_1$, an electron from the sub-shell L_3 fills a vacancy in L_1 and an electron is released from M_1. The sum of the fluorescence yield, ω , Auger yield, a , and Coster-Kronig yield, f, to any primary vacancy is unity

$$\omega + a + f = 1 \qquad (11)$$

The value of f can be close to one, especially for a vacancy in the first sub-shells, such as L_1, M_1, etc.. Krause 1979 gives values of the Auger and Coster-Kronig yields for the L sub-shells for elements from Z = 1 to Z = 59.

Although Auger and Coster-Kronig transitions together form the predominant means of atomic relaxation,

there are other competing processes which play a small role in the de-excitation process, Sevier 1972.

1/ Double Auger effect, Carlson and Krause 1965, Larkins 1972

2/ Inter-atomic Auger effect, Citrin et al 1976

3/ Electron shake-up and shake-off, Larkins 1972, Carlson 1975a

4/ Autoionization, Sevier 1972, Carlson 1975b

5/ Plasma excitations, Sevier 1972

For this dissertation, being concerned with energy-deposition calculations following inner-shell ionization, such processes make a very small contribution and therefore have been neglected.

2 The incorporation of radionuclides in biological material

2.1 The site of incorporation

Incorporated radionuclides which decay by electron capture, internal conversion or beta decay produce several consequences to the biological medium with which they are bound. The list of influences which result in a biological effect are: transmutation, nuclear recoil, beta-ray energy deposition, Auger-electron energy deposition and the charge build-up on the daughter product, many of which produce only local effects. A discussion of the physical consequences of each of these will be given in section 2.2. This section discusses the biological sensitive structure, the DNA, and on the incorporation of radionuclides into the cell nucleus and the DNA.

The DNA molecule (figure 6) contains the genetic code of a cell by the sequence of 4 nucleic acid bases: adenine, guanine, cytosine and thymine. For review of the chemical structure of DNA see Kronberg 1974. The incorporation of radionuclides in the DNA can take place via thymidine precursor which is built into the DNA during synthesis, Wilson 1966. The halogen analogues of thymidine, e.g. iododeoxyuridine -IUdR and bromodeoxyuridine-BUdR, where the iodine atom may be ^{125}I, ^{123}I, or ^{131}I and the bromine ^{80m}Br, differ from thymidine through a replacement of the methyl group in position 5 of the pyrimidine ring by the hot halogen atom (figure 7). Using a thymidine precursor has the advantage of a specific incorporation in DNA and hence in the cell nucleus, but no incorporation in the cellular cytoplasm or the cell membrane.

DNA is perhaps not the only radiosensitive structure of the cell but it is by far the most sensitive. The high toxicity of radionuclides incorporated into the DNA suggests a strong correlation between damage to the DNA and cell death. Such effects as transmutation, charge build-up and atomic recoil when occurring in the DNA may

Figure 6
Illustration of the chemical single and spatial double strand structure of the DNA molecule.

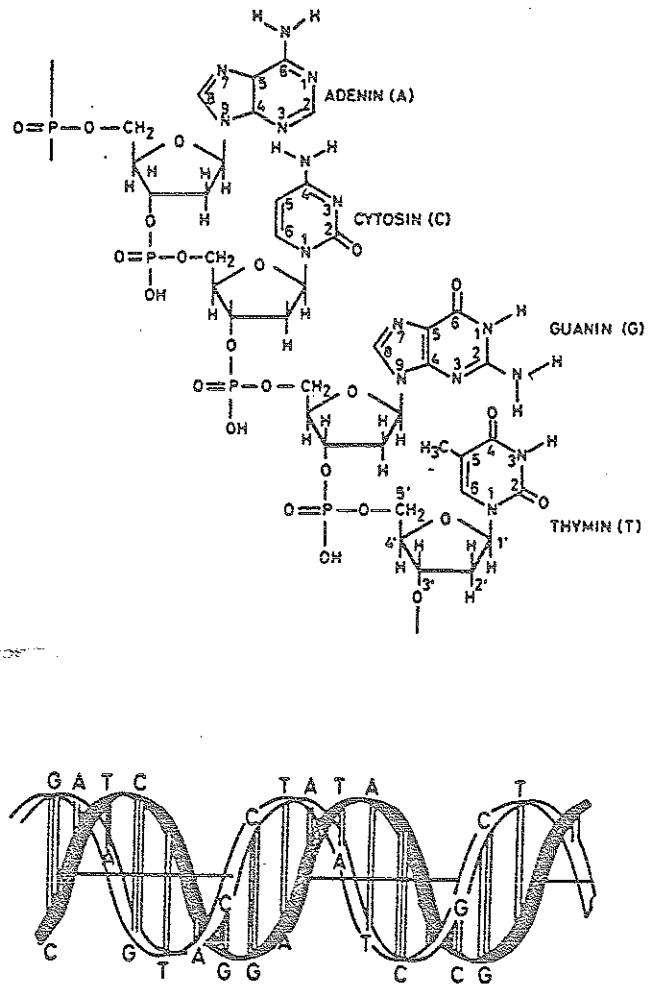

Figure 7
Thymidine and iodine labelled thymidine (IUdR).

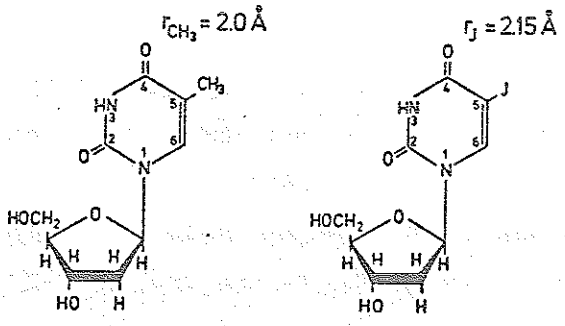

be important for the induction of single strand breaks, nucleotide base alteration leading possibly to cell mutation. The possibility of energy deposition by Auger electron emission at sites of the DNA other than the direct location of the radionuclide may lead to double strand break production with a decisive influence on a cells chance for survival. It is for this reason that the deposition in volumes of 1 nm - 10 µm diameter is a significant parameter with which to relate the probability for double strand break production and therefore cell death.

For electron capture decaying radionuclides such as ^{125}I which deposit a high concentration of energy by an intense flux of low energy electrons it is essential to get these isotopes in the sensitive DNA targets. This was demonstrated for example by Hofer et al 1977 who compared cell survival curves[5] for ^{125}I incorporated in the DNA and the cell membrane of mammalian cells. The membrane case gave a normal shouldered survival curve corresponding to the dose induced by the X- and gamma-rays of ^{125}I. But for ^{125}I bound directly to the DNA in the form of IUdR, a steep shoulderless curve was obtained. Thus it can be concluded that the radiotoxicity of incorporated radionuclides depends not only on the nature of the decay but also on their microdistribution in relation to the sensitive areas of the cells. The same type of effect is to be expected from the radionuclide ^{123}I with its similar mode of decay.

Studies of tritium incorporation have shown that the effectiveness of this isotope may even depend on its position of uptake in the DNA: for mutation induction ^{3}H incorporated in the 5 position of the pyrimidine ring of cytosine was found to be between 3-6 times more effective

[5] A "survival curve" is generally a plot of the logarithm of the relative frequency of biological entities not showing the particular end-point under observation as a function of absorbed dose, (see Alper 1979). Mostly the term "cell survival" is not intended to describe survival probabilities of individual cells but is related to non-inactivation of the colony forming ability of cells in culture or even to other cellular end-points.

than when incorporated in the 6 position or into the methyl group of thymidine, Feinendegen and Cronkite 1977.

Other experimental incorporation work in the DNA has been performed where the phosphorus atom in the backbone structure (figure 6) has been replaced by the radioactive phosphorus isotopes ^{32}P and ^{33}P, Apelgot and Adloff 1978 (in part II of this thesis the prospect of photoelectric induced Auger emission from phosphorus bound DNA is discussed). Apelgot et al 1980 have also published results on double strand break production for cell incorporation experiments using ^{64}Cu. The high effectiveness of ^{64}Cu in creating biological damage, (about one double strand break per disintegration) is unexpected since little is known about the microdistribution of copper in relation to the DNA. The existence of copper ion - nucleic acid complexes is described in the literature and therefore a chemical bond with the DNA may be possible, Bandekar and Sathyanarayana 1979, although the bond might be formed first after the decay.

Another radionuclide of relevance to this thesis is ^{55}Fe for which investigations have been made on the susceptibility of reticulocytes to ^{55}Fe- loaded bone marrow, Reincke et al 1978. The uptake of the ^{55}Fe is mainly in the haem which becomes incorporated in the haemoglobin in the cytoplasm of red blood cells, i.e. the quantity of ^{55}Fe in the cell nucleus is likely to be quite small, Reincke et al 1975.

2.2 The physical consequences of radionuclide decay

The chemical and biological effects produced by incorporated radionuclide decay are the result of several simultaneous mechanisms of local energy deposition where the independent weight to be attached to each contribution is still a matter of debate, Ertl et al 1977, Martin and Haseltine 1981. The most important of these mechanisms is the subject of this section.

2.2.1 Transmutation

The chemical transmutation of an incorporated radionuclide occurs whenever the decay is by beta emission including electron capture [6]. The effect of radionuclide transmutation in the DNA is to lead to possible molecular alterations due to the altered chemical relation of the transmuted atom to its immediate enviroment. As examples are the phosphorus radionuclei ^{32}P and ^{33}P which after decay become sulphur. Apelgot and Adloff 1978 have shown that such a transmutation occurring in the DNA strand can contribute greatly to the production of single strand breaks.

With the principal radionuclides under discussion in this work, namely ^{125}I, ^{123}I, ^{55}Fe and ^{64}Cu, only the former two are incorporated directly into the DNA. Both ^{125}I and ^{123}I decay by electron capture the iodine atom transforming to tellurium which may feasibly contribute to a harmful effect. For ^{55}Fe and ^{64}Cu which are probably not connected to any sensitive cellular target a noticeable transmutation effect is unlikely.

Some mention should be made of the processes shake-up and shake-off which usually accompany transmutation. As a result of transmutation the atomic electrons must readjust to the sudden change in nuclear charge. Electronic rearrangement produces a small excess of free energy which transferred to a single outer-shell electron is sometimes sufficient to secure its release. An electron released or excited in this way is referred to as a shake-off or shake-up electron respectively.

2.2.2. Nuclear recoil

The emission of any particle from the nucleus produces a nuclear recoil necessary for the conservation of

[6] In isomeric transitions such as ^{80m}Br no transmutation takes place.

momentum. The magnitude of this recoil increases with decreasing mass of the radionuclide and increasing energy of the emitted particles. For beta emission there is a spectrum of recoil energies constituted of the vector addition of the electron-neutrino recoils. The recoil energy of a beta emitter can be of the order of several electron volts and may therefore be sufficient to cause bond breakage, e.g. by the decay of ^{32}P the average recoil energy of the ^{32}S nucleus is 38.7 eV, Apelgot and Adloff 1978.

Decay by electron capture and internal conversion also produces a recoil due to the neutrino and gamma ray or internally converted electron respectively supplemented by a very small atomic recoil momentum from the emitted Auger electrons. The recoil in this case is however usually too small to cause bond breakage. For example, Ertl et al 1970 calculated the nuclear recoil due to neutrino emission after electron capture for ^{125}I. The average recoil energy is a mere 0.1 eV

2.2.3 Beta-ray energy deposition

A beta-emitting radionuclide incorporated in the DNA or somewhere in the cell nucleus will, depending on the energy of the beta particle, deposit only a small fraction of that energy inside of the sensitive DNA target or of the cell nucleus. The DNA molecule is a long supercoiled double helix structure of 2 nm strand width within a cell nucleus of about 8 μm diameter. The fractions of the initial beta-ray energy remaining in both the DNA and the cell nucleus depend on the ranges of the beta particles. For beta energies greater than about 17 keV the range becomes larger than the diameter of the cell nucleus, and hence one may consider the radiation source to be homogeneous. For beta particles of short range the radionuclide microdistribution becomes more important as the energy deposition becomes increasingly localized at the incorporation sites.

Such a inhomogeneity is of particular significance for radionuclide which emit electrons of very low energy, i.e. Auger electrons, whereby the local energy density in the nanometer range can be extremely high. In this case the absorbed dose when averaged over the entire cell population could lead to a considerable underestimation of the biological consequences of that incorporated radionuclide.

2.2.4 Auger-electron cascade

Radionuclides which decay by electron capture or internal conversion i.e. in which inner-shell atomic vacancies are produced, emit cascadewise a number of Auger and Coster-Kronig electrons. Since most of the emitted electron energies are below 100 eV, the ranges of these particles are often extremely short. Hence they deposit most of their energy in the near vicinity of the decay site, which is important for radionuclides incorporated in the DNA.

The energy deposition resulting from the emission of Auger electrons in a vacancy cascade is possibly one of the most significant factors in causing the high radiotoxicity of electron capture and internal conversion decaying radionuclides and for a radioisotope such as ^{125}I largely outweighs the effect produced by transmutation or nuclear recoil.

2.2.5 Charge build-up and neutralization

For the release of each Auger electron during a vacancy cascade one positive charge is left on the decay product. An Auger cascade therefore produces a rapid build-up of charge at the decay site. This can create a local disruption of the molecule since electrons from the valence band of other atomic constituents which participate in chemical bonding may be drawn to neutralize the charge on the daughter atom. This latter process is

referred to as charge neutralization and can have considerable molecularly destructive consequences, Carlson and White 1963.

In conclusion, the extent to which the five factors above play a role in creating molecular and subsequent biological damage depends on the nature of the radionuclide decay and its incorporation site. For electron capture and/or internal conversion decaying radionuclides incorporated in the DNA the Auger cascade and the thereby arising charge effect are likely to be the dominant modes in which damage is inflicted. For beta emitters in the DNA transmutation and recoil may be accredited an important significance. Radionuclides elsewhere in the cell produce their effect by the longer range Auger electrons or beta particles.

Using a new Monte-Carlo approach energy deposition calculations have been performed for the radionuclides ^{125}I, ^{123}I, ^{55}Fe and ^{64}Cu. The technique and results of this work occupy the rest of part I.

3 Monte-Carlo calculations for Auger electron cascades following the decay of radionuclides

3.1 Introduction to Monte-Carlo methods

The Monte-Carlo method is a technique particularly suitable for obtaining approximate solutions to problems containing a number of random processes with a large number of possible outcomes, Sobol 1974. A typical example of a Monte-Carlo type problem is the simulation of an electron track through a medium, where different interactions are possible and the path has the nature of a random walk.

The application to which Monte-Carlo methods are applied here is the simulation of electron capture/internal conversion or beta-decay processes together with the random vacancy-cascade process, in order to obtain statistical data about the electron and photon emission spectra for the decay of radionuclides.

A Monte-Carlo code developed by Charlton and Booz 1978, 1981, to calculate the electron and photon spectra of ^{125}I has been modified and applied, as part of this thesis, to the radiobiologically relevant isotopes : ^{123}I, ^{55}Fe, ^{64}Cu.

The programme consists of a large set of input data consisting of initial vacancy distributions after electron capture and internal conversion, photon, Auger and Coster-Kronig relative transition probabilities and energies, and also of a beta spectrum in the case of ^{64}Cu. The characteristic of a Monte-Carlo code is that at each stage of the calculation a transition is forced to occur. In other words at any stage in the programme the sum of all transition probabilities is always one. The programme is then brought to an end when a particular set of criteria have been fulfilled, (see section 3.3). Using the random number generator GGUW, Learmonth and Lewis 1973, a pool of numbers between 0 and 1 are generated which are selected at random and which determine successive transitions to be taken. In this way a series of individual disintegrations

can be simulated. By repeating this process a large number of times, a good statistical distribution of the electron and photon emission spectra can be obtained. In this section the entire input data and finally the structure of the Monte-Carlo programme will be discussed.

3.2 The input data

3.2.1 The initial vacancy distributions

The relative probability of creating a vacancy in each individual sub-shell of an atom by electron capture or internal conversion, referred to here as the initial vacancy distribution, can be calculated using the methods described in sections 1.3 and 1.4. For the decay 100% electron capture the sum of the probabilities to create a vacancy in each sub-shell is normalized to give a probability of one. If the decay scheme has branching, for example ^{123}I, then the initial vacancy distribution must be calculated for each decay pathway seperately and subsequently normalized to the branching frequency. In this way a correct number of vacancies are initiated in each individual sub-shell from Monte-Carlo calculations simulating the process of electron capture radionuclide decay. The treatment of initial inner shell vacancies produced by internal conversion is analogous.

Tables 1 and 2 give the calculated initial vacancy distribution data for the isotopes ^{123}I, ^{125}I, ^{55}Fe and ^{64}Cu. The lines "Te level" in table 1 and "Ni level" in table 2 specify the levels of the excited states of the nuclei after disintegration of ^{123}I and ^{64}Cu respectively.

Table 1

Initial vacancy distributions for ^{123}I

	EC [7]				IC [7]			
Te level MeV	.159	.440	.506	.693 [8]	.159	.440	.506	.693 [8]
K	.797	.004	.003	.014	.146	-	-	.001
L1	.104	-	-	.002	.017			-
L2	.003				.002			
L3	.007				.001			
M1	.022				.003			
M2	.001				-			
M3	.038							
N1	.005							
Sum	.977	.004	.003	.016	.169			.001

Total electron capture probability = 1.0

Total internal conversion probability = 0.17

Table 2

Initial vacancy distributions for ^{125}I, ^{55}Fe and ^{64}Cu

	I-125 [9]		Fe-55		Cu-64	
Ni level MeV	EC	IC	EC	EC 0	EC 1.346	IC 1.346
K	.808	.795	.885	.359	.005	-
L1	.154	.095	.097	.039	.001	
L2	.004	.007	.00	-	-	
L3	-	.004	.002	.001		
M1	.035	.019	.015	.006		
M2	.001	.004	-	-		
M3	-	.001				
N1		.004				
N2		.001				
Sum	1.0	.930	1.0	.405	.006	0.0

[7] Electron capture = EC, internal conversion = IC

[8] The .693 MeV level is an average of the two levels .688 MeV and .698 MeV.

[9] From Charlton and Booz 1981.

3.2.2 Transition probabilities for radiative and non-radiative transitions

One important set of input data is the one desribing the relative probabilities of electron transitions to the inner shell vacancies produced in the atom. The number of possible transitions to an inner shell vacancy is in general quite large, depending on the size of the atom and the position of the vacancy, (see for example the number of electron transitions for tellurium, appendix 3). The nature of the transition can be either radiative when a photon is released or non-radiative resulting in Auger electron emission. Experimental and theoretical data are available on the photon transition probabilities : Storm and Israel 1970, Salem, Panossian and Krause 1974. For the Auger and Coster-Kronig transition probabilities the data is largely from quantum mechanical calculations of oscillator strengths, experimental data being far less complete. In this work the K-Auger transition probabilities were taken from Asaad and Burhop 1958, Chen, Crasemann and Mark 1979 and Casey and Albridge 1969. For the L-, M- and N- shell transitions the data of McGuire 1972, 1975 and 1977 was used.

Since the form of the transition probability data is generally relative to a single established strong transition the photon, Auger and Coster-Kronig transition probabilities were renormalized to the fluorescence, Auger and Coster-Kronig yields, the sum of which are one for each individual sub-shell. For all sub-shells higher than M_1 the fluorescence yield becomes so low, for the elements of concern here, (less than 0.001) that radiative transitions have been neglected.

For decay by electron capture the nuclear charge is decreased by one. Therefore all electron transition probabilities were taken from the element having one nuclear charge less than the decaying radionuclide, i.e. for the decay of ^{123}I and ^{125}I the transition data for tellurium were used.

Appendix 3 gives further details on the form the

electron transition probabilities to single vacancies in K and L_1 sub-shells of tellurium in the normalized form used in this work.

3.2.3 Photon and Auger energies

In the data set presented in table 3a, appendix 3 are given the photon and Auger electron energies resulting from electron transitions to vacancies in the K and L_1 sub-shells of tellurium. The photon energies are available from experimental sources, Storm and Israel 1970, or can be calculated from atomic energy levels, Bearden and Burr 1967, using equation (12) (see section 1.5).

For the Auger and Coster-Kronig electrons no precise analytical formula is known and experimental sources are scarce and incomplete. In many text books on atomic physics Auger electron energies are given by the equation,

$$E_A = E_1(Z) - E_2(Z) - E_3(Z+\Delta Z) \qquad (12)$$

where E_A = kinetic energy of the emitted Auger electron,
$E_1(Z)$ = binding energy of the vacancy level
$E_2(Z)$ = binding energy of the vacancy filling electron from the neutral atom and
$E_3(Z+\Delta Z)$ = binding energy of the emitted electron of the atom with a single vacancy in the E_3 level.

The specification of Z is not easy, however, the relation which gives reasonable agreement with experimental values is referred to as the modified Z+1 approximation, Chung and Jenkins 1970.

$$E_A = E_1 - \{1/2[E_2(Z)+E_2(Z+1)] + 1/2[E_3(Z)+E_3(Z+1)]\} \qquad (13)$$

In this equation average values are taken for the energy levels between the element with a nuclear charge Z and the

element with a nuclear charge Z+1 thereby partly compensating for the change in the screening factor involved in the Auger process.

A catalogue of Auger electron energies have been calculated in this way by Coghlan and Clausing 1973. In this work the values of Coghlan and Clausing were used, for those transitions for which data was available. The rest were calculated using equation (12)

Lastly with reference to chemical shifts in the electron energy levels, Sevier has published tables with electron binding energies for different chemical phases, Sevier 1979. The effect of phase is small, at most about 20 eV and therefore only the energy levels for atoms have been used in this work.

3.3 The Monte-Carlo code

The computer code developed to simulate, using Monte-Carlo methods, radionuclide decay is a single programme consisting of more than 1000 internal statement numbers (approx. 130K bytes). The structure of the programme is given in flow chart form in appendix 4, a summary of which is presented here.

The input step in the code contains the various input parameters such as the electron occupation numbers of the individual sub-shells for the atom in the ground state, all transition probabilities and their respective photon and Auger electron energies in the format of table 3a, appendix 3, the initial electron capture vacancy distribution and other relevant data for the atom.

A random number is selected using the fortran library sub-routine GGUW, Learmonth and Lewis 1973, which is used to determine the mode of decay. If electron capture as opposed to beta decay is chosen, then the random number generated is used to produce a vacancy in one of the inner atomic sub-shells. If beta decay, then a beta particle energy is chosen from the spectrum (see appendix 1) and the first disintegration is finished, i.e. the programme goes on to the next disintegration.[10] The

electron vacancy produced by electron capture is recorded, i.e. the electron occupation for the corresponding shell reduced by one and the charge on the atom set at +1.

This leads to a loop of electron capture produced vacancy cascades. First the relevant block of transition probabilities to the electron capture initiated vacancy must be addressed. Then a renormalization of the transition probabilities is carried out (see later for explanation). With a further random number one of the possible electron transitions is chosen. For an Auger transition the value the number of electrons released and the charge on the atom are increased by one and the kinetic energy of the Auger electron stored. For a photon transition the value of the number of photons emitted, is increased by one and its energy stored. The charge on the atom remains unchanged in a photon transition. The atom must now be readjusted for the new electronic arrangement within each sub-shell.

Consider the case of the first transition being an Auger transition. The new state of the atom contains 2 inner-shell vacancies. The assumption has been made that the vacancy cascade proceeds so that the deepest lying vacancy in the atom is filled first. Before choosing a transition in an atom with more than one vacancy, the transition probabilities are corrected for the changing occupation numbers of each individual sub-shell. The assumption has been made that the probability of any electron shell participating in a transition must be reduced in proportion to the fraction of electrons remaining in that shell. After this correction the transition probability data must be renormalized to one. In this way the whole process of the vacancy cascade is simulated continuing until one of two criteria is fulfilled. Either so many vacancies have been produced in the atom that the sum of the unnormalized transition probabilities to the

[10] Beta decay only occurs for the radioisotope ^{64}Cu in the scope of this work.

deepest lying vacancy is zero or extremely small, (less than 10^{-6}) or all the vacancies have reached the outer shells of the atom.

After completion of the process of atomic de-excitation following electron capture, a conditional statement in the computer code asks whether the radionuclide has reached the ground state. If the answer is yes then the disintegration ends and the programme goes on to treat the next disintegration. Otherwise the atom returns to the ground state either by internal conversion or gamma emission. The decision on the type of process is again made by the random-number generator. For gamma decay the gamma energy is stored, i.e. the difference in energy between the excitation level and the ground state.[11] If internal conversion is chosen then the random number determines the inner shell vacancy. This vacancy is recorded, the internal conversion electron energy calculated and stored and the values of the electron emission number and atomic charge increased by one. This new inner shell vacancy initiates a second cascade (the internal conversion loop), which runs analogous to the electron capture loop with the same escape criteria. Once the second cascade is finished the programme returns to the start to simulate the next decay.

The calculations performed in this work were for the simulation of 10,000 disintegrations per radioisotope.

3.4 Assumptions in the Monte-Carlo calculation

In most scientific models, simplifying assumptions have to be made in order that a solution to the problem set is at all possible. Before finishing this section, therefore some of the presuppositions of the vacancy-cascade model, used in those calculations, will be discussed and their relation to reality clarified.

[11] For ^{123}I various combinations of gamma routes to the ground state are possible.

There have been 4 major assumptions made in this work which contribute to systematic uncertainty of the calculation.

1/ The first major difficulty is that the electron transition probabilities are only known for singly ionized atoms. In a vacancy cascade where several vacancies arise nearly simultaneously within the atom one has no clear knowledge about the changes in the relative transition probabilities. In these calculations the relative probabilities have been used for a singly ionized atom adjusted to take into account the positions of all the atomic shell vacancies, whereby the probability of an individual electron shell participating in a transition is reduced in proportion to the number of electrons remaining in that particular shell.

2/ Only photon, Auger and Coster-Kronig transitions have been considered. All other atomic de-excitation mechanisms have been neglected.

3/ The vacancy cascade has been treated stepwise i.e. the transitions follow chronologically one after another. In reality the cascade process is so fast (approx.10^{-14}s) that the electronic rearrangement for different transitions are interwoven with one another.

4/ Also during the vacancy cascade the atomic energy levels will not be constant. The assumption of constant energy levels or of the modified Z+1 approximation means that the uncertainty in the photon and electron energies increases, the greater the number of steps in the cascade.

4 Results of Monte-Carlo calculations for iodine-123 and iodine-125

In this section the results of new Monte-Carlo calculations for ^{123}I and repeated calculations for ^{125}I, (first performed by Charlton et al. 1978) are presented. The section is divided into 3 sub-sections. The first contains electron number distributions and electron and photon spectra for the decays of ^{123}I and ^{125}I as isolated atoms. The second considers similar calculations for ^{123}I and ^{125}I incorporated within a medium, in which a simple model is used to simulate the process of neutralization of the charge build-up during the vacancy cascade. The effect of charge neutralization on the number of emitted electrons and energy spectra is examined on hand of new calculations. Thirdly the results of calculations are presented for ^{123}I and ^{125}I in form of the molecule methyl iodide. These results provide an opportunity to test the accuracy of the Monte-Carlo calculational approach with the experimental measurements of Carlson and White, 1963, who measured the charge distribution on the fragmented CH_3I^{125} molecule after the decay of ^{125}I.

4.1 ^{123}I and ^{125}I as isolated atoms

4.1.1 Electron number distribution

For each individual disintegration of ^{123}I and ^{125}I a number M of electrons and N photons are emitted. The distribution of the number of electrons emitted per disintegration is shown in figure 8 for ^{123}I in comparison with the number for ^{125}I per electron capture event and per complete disintegration. The range of the number distributions for both isotopes is from 0 - 25 electrons, i.e. in a single decay between 0 - 25 electrons can be released. The shape of the distribution for ^{123}I, however resembles more that for ^{125}I per electron capture event, i.e. from the first cascade only. This is because the isotope ^{123}I only has 0.16% chance of undergoing a second vacancy cascade due

to internal conversion. The small percentage of disintegrations in which a double cascade occurs extends the maximum of the distribution up to 25 electrons.

Figure 8

Electron number distribution for ^{123}I and ^{125}I after a single cascade and a double cascade process.

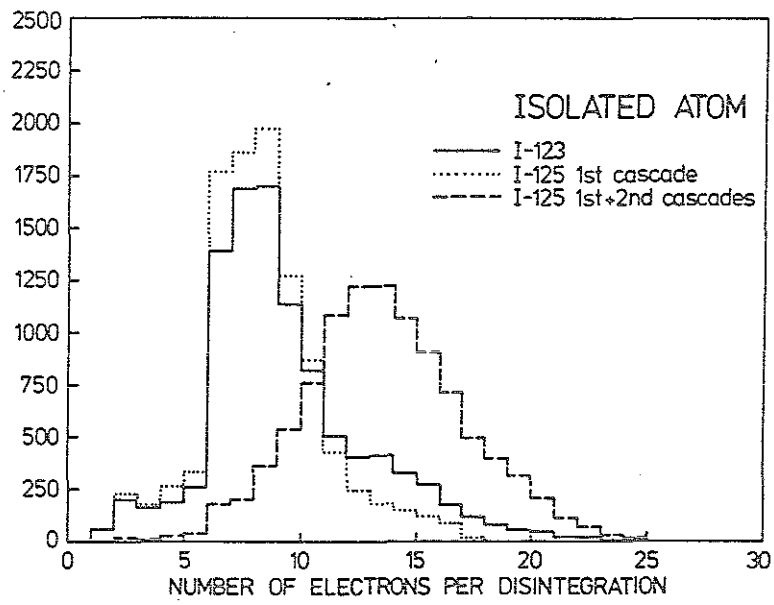

The average number of electrons emitted per disintegration $\bar{n}$ are given in table 3 for both isotopes after complete decay as well as per electron capture event. The values of $\bar{n}$ for both isotopes are the following : after

electron capture almost identical, 7.9 for ^{123}I and 7.8 for ^{125}I. [2] For the full decay, however the high probability of a second internal conversion induced cascade for ^{125}I increases the average number of emitted electrons to 13.2, whereas for ^{123}I the increase is only by a single electron to 8.9. These numbers agree with about 5.5 to 6 electrons emitted during the second cascade, because for ^{125}I $\bar{n}=13.2 \simeq 7.8+0.93x5.5$ and for ^{123}I $n=8.9 \simeq 7.9+0.16x6$; in other words, the difference in the number of electrons emitted is mainly influenced by the different internal conversion probabilities of 0.93 and 0.16 for ^{125}I and ^{123}I respectively.

4.1.2 Electron energy spectra

Each individual disintegration of ^{123}I or ^{125}I produces an individual electron and photon spectrum, a fingerprint of the electron transitions which have taken place in the process of nuclear and atomic de-excitation.

Two examples of individual electron spectra for ^{123}I are shown in figure 9, the first one following a single vacancy cascade after electron capture only in which 8 electrons were emitted, the second a double vacancy cascade after both electron capture and internal conversion in which 14 electrons were emitted. The high energy electron in the lower figure at 127 keV is due to an internal conversion electron in the tellurium K shell.

10,000 such individual electron spectra were generated for both isotopes and stored on magnetic tape. Using the individual electron spectra, the average electron spectra could be calculated for ^{123}I (figure 10) and ^{125}I (figure 11), showing the emission probability of individual electron energies. The two spectra are similar since the inner-shell atomic transitions are of the same

[12] For ^{123}I the value of $\bar{n}$ is fractionally greater than for ^{125}I after the first cascade. This comes from the slightly higher K shell electron capture probability for ^{123}I (see tables 1 and 2).

Figure 9
Two individual electron spectra produced by ^{123}I after a single cascade and a double cascade process.

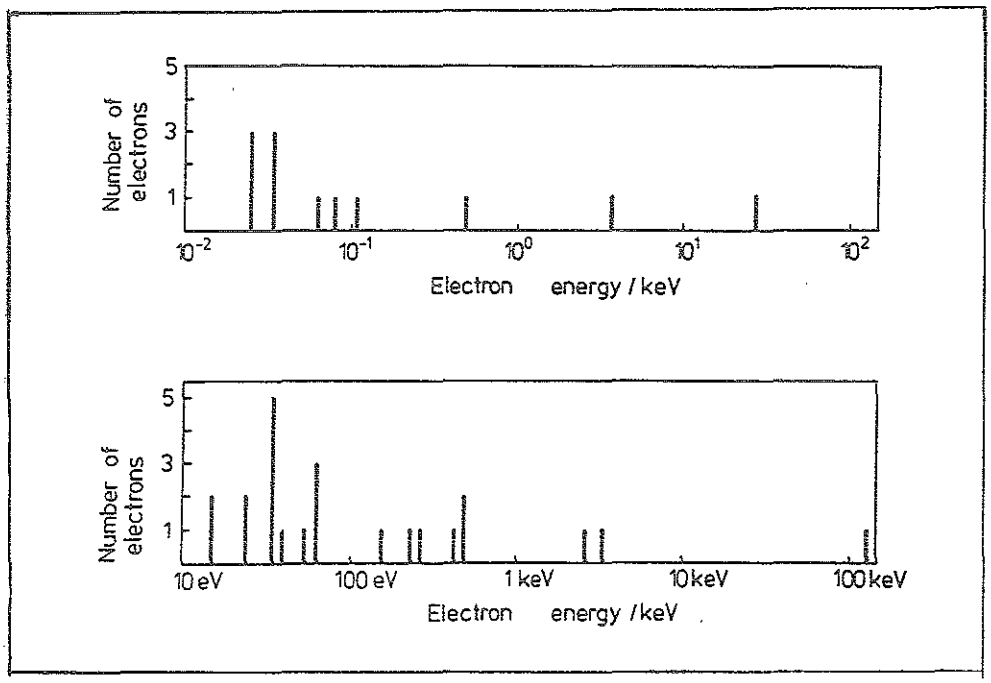

Figure 10
Average individual electron spectrum for ^{123}I.

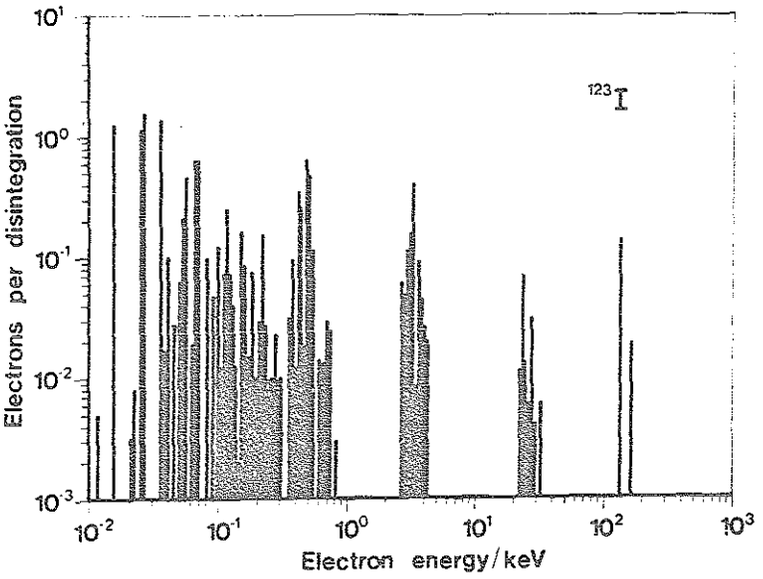

Figure 11
Average individual electron spectrum for ^{125}I.

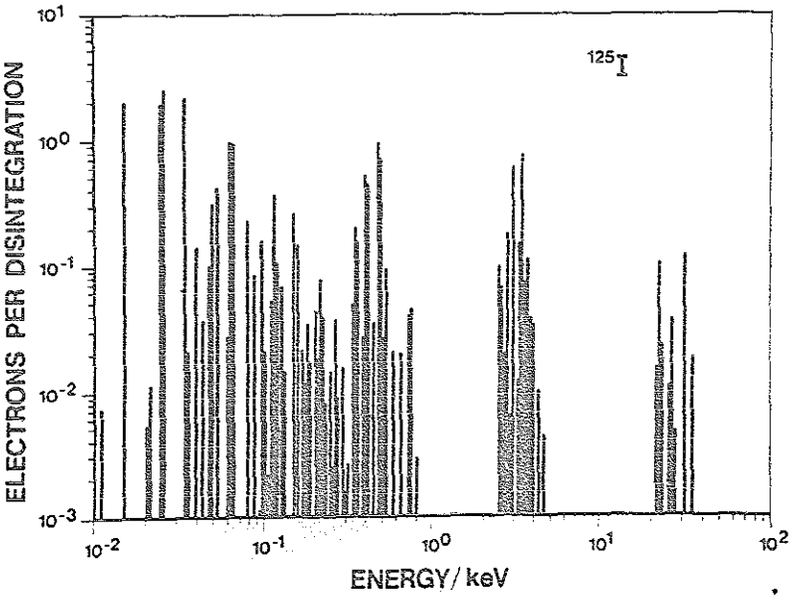

tellurium daughter product. The two spectra differ, however, in the energy range of the spectra, i.e. for ^{123}I the internal conversion electrons are of much greater energy than for ^{125}I, and secondly in the frequency of electron emission per disintegration which for ^{125}I is between 50 - 100% higher than for ^{123}I. This higher frequency of electron emission for ^{125}I is the result of the high internal conversion probability for this isotope, (see table 1, section 3.2.1).

4.1.3 Photon energy spectra

In the process of radionuclide decay it is the emission of electrons which are responsible for the high local energy deposition around the decay site. However photons are also released and although their contribution to the local energy deposition is negligible the properties of the photon spectra for ^{123}I and ^{125}I are mentioned here for completeness.

The average number of photons emitted per disintegration for ^{123}I is only 1.86 and for ^{125}I 1.69, i.e. very low in comparison to electron emission. However, it is still possible to calculate average individual photon energy spectra for ^{123}I (figure 12) and ^{125}I (figure 13) with sufficiently large numbers of Monte-Carlo histories. Both spectra consist of two distinguishable components. Firstly, the gamma-ray component (from the alternative decay mechanism to internal conversion) which for ^{123}I represents an intense line at 159 keV together with a series of higher energy lines of low probability due to decay from the various metastable tellurium levels whereas for ^{125}I there is only a single line at 35.4 keV. Secondly there is the same characteristic X-ray spectrum from tellurium due to inner shell transitions after electron capture or internal conversion. The higher intensity of this part of the spectrum for ^{125}I (by about 75%) results from the greater internal conversion probability, which induces more inner shell vacancies and hence photon transitions for ^{125}I than ^{123}I.

Figure 12
Average individual photon spectrum for ^{123}I.

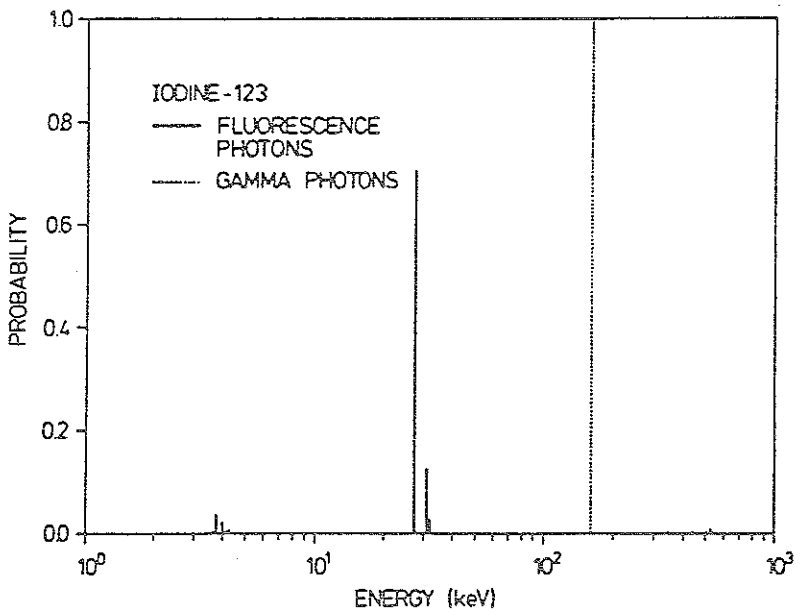

Figure 13
Average individual photon spectrum for ^{125}I.

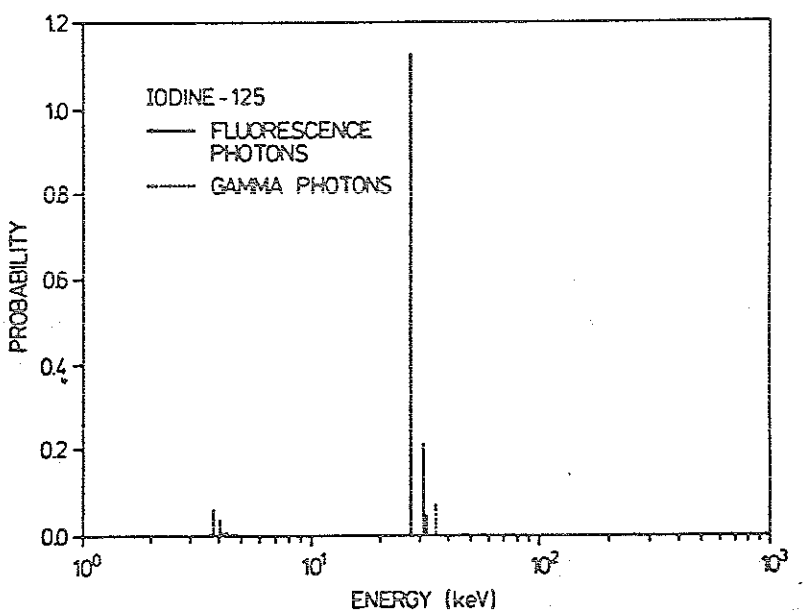

4.1.4 Energy fractions

The total energy emitted in radionuclide decay is equal to the sum of the energies of all emitted particles plus the potential energy remaining in the form of charge on the daughter atom. In the beta decay processes not all the energy released potentially contributes to the absorbed dose since a certain fraction of the decay energy is emitted as neutrino kinetic energy. Therefore in this work the total energy per decay refers to the sum of the energy depositing components i.e. electrons, photons and potential energy.

From the simulation of 10,000 disintegrations per isotope, the average values for the energy per disintegration emitted in the form of electron and photon energy as well as average potential energy of the multiple charged atom were calculated. The values are tabulated together with their sum, the average total energy release per decay, in table 4.

The results show that a greater average electron energy, $\bar{E}$, is emitted per disintegration for ^{123}I (27.62 keV) than for ^{125}I (18.1 keV) although the average number of electrons per decay, $\bar{n}$, is lower for ^{123}I. The average photon energy per decay, $\bar{P}$, for ^{123}I is also larger. Both result from the higher nuclear excitation levels of tellurium involved in the decay of ^{123}I where the emission of high energy gamma-rays or internal conversion electrons considerably weight the calculated averages.

Lastly a small fraction of decay energy remains as potential energy on the atom. The average potential energy per decay, $\overline{IP}$, is proportional to the average charge, $\bar{q}$, produced on the atom by the vacancy cascades. This energy is equal to the sum of the ionization potentials for a tellurium atom of charge q. For ^{125}I where more electrons are emitted per decay, the average potential energy produced is 2.1 keV, whereas for ^{123}I it amounts to slightly less than 1 keV.

4.2 Iodine-123 and iodine-125 incorporated in a medium

4.2.1 The neutralization process

The discussion in 4.1 considered the decay of the iodine radionuclides as isolated atoms, i.e. where the process of atomic de-excitation remains uninfluenced by any enviromental charge exchange effects. For radionuclide incorporation in biological tissue the build-up of positive charge during a vacancy cascade produces an increasingly strong attractive Coulomb force on electrons in surrounding atoms of the medium. Electrons from neighbouring atoms will then be torn from their bonds to neutralize this charge build-up on the tellurium daughter atom.

For this work a simple charge neutralization model was applied in which it was assumed that at all times a sufficient number of free or weakly bound electrons available to rapidly neutralize charge arising on the tellurium atom. This assumption is perhaps more suitable for a radionuclide incorporated in a condensed medium rather than a typical biological one. Nevertheless the condensed phase model used is representative in the sense that the charge on the tellurium will eventually be dispersed in a biological medium also. Both sets of calculations for the isolated radionuclide and the condensed phase model represent two extremes i.e. the bounds between which a real situation will lie.

The neutralization code works as follows. The charge on the tellurium atom is recorded throughout the vacancy cascade. Once this charge becomes greater than +1 an electron from the medium is assumed to be drawn by the charge on the tellurium into the outer orbital region of that atom, thus becoming able to participate in Auger transitions within the tellurium atom itself. The transition probabilities for tellurium are then so adjusted that transitions to inner shell vacancies from the outermost shell (which are proportional to the number of electrons in that shell) become increasingly more probable. The consequences of this neutralization are the subject of

the next section.

4.2.2 Influence of neutralization on electron number

The effect of charge neutralization during a tellurium vacancy cascade significantly increases the number of electrons emitted per disintegration. This is because for an isolated radionuclide the outer shells of the atom become depleted during the cascade thus continually reducing the number of possible transitions, whereas with neutralization the source of outer shell electrons is never depleted, being constantly replenished by electrons from the medium.

Electron number distributions for both ^{123}I and ^{125}I calculated using the assumptions of the condensed phase model are given in figure 14. The average of the distributions, n, are 12.3 for ^{123}I and 21.1 for ^{125}I in comparison to 8.9 and 13.2 respectively for the isolated atom calculations (table 3).

The effect of neutralization on the electron number distribution is more clearly shown in figure 15 where a comparison is made between ^{125}I as an isolated atom, in condensed phase and in the form of methyl iodide [13]. The broadness of the distribution as well as the average electron emission number $\bar{n}$ depends on the maximum number of participant neutralization electrons.

4.2.3 Electron number, electron energy and their frequency

The effect of charge neutralization is not only to increase the number of Auger electrons emitted per disintegration but also the electron energy per disintegration. Because the photon energy remains unaltered irrespective of phase,[14] the increase in electron energy comes from a transfer from atomic potential energy.

[13] In the case of methyl iodide the extent of charge neutralization is limited by the number of electrons available on the ligand (see section 4.3).

[14] Radiative transitions occur in general only between inner shell orbits and then at a time before any charge build-up.

Table 3

Average number of electrons emitted after electron capture and after the complete decay of ^{123}I and ^{125}I

	$\bar{n}$			
	Iodine-123		Iodine-125	
	first cascade	full decay	first cascade	full decay
Isolated atom	7.9	8.9	7.8	13.2
Methyl iodide	9.5	10.5	9.4	15.4
Condensed phase	10.5	12.3	10.4	21.1

Table 4

Average electron, photon and potential energy following the decay of ^{123}I and ^{125}I

	Iodine -123			Iodine-125		
	Isolated atom	Condensed phase	Dillman & Van der Lage	Isolated atom	Condensed phase	Dillman & Van der Lage
$\bar{E}$	27.62	28.36	28.25	18.1	19.9	19.5
$\bar{P}$	168.0	168.0	168.9	41.5	41.5	42.4
$\overline{IP}$	0.74	-		1.8	-	
$\bar{T}$	196.36	196.36		61.4	61.4	

$\bar{E}$ = average electron energy per disintegration

$\bar{P}$ = average photon energy per disintegration

$\overline{IP}$ = average potential energy of the atom per disintegration

$\bar{T}$ = average total energy released per disintegration

In the condensed phase model, since the total charge on the tellurium is neutralized the entire potential energy of the atom is released in the form of additional low energy electrons.

Average values of the electron energy for ^{123}I and

Figure 14
Comparison of the electron number distributions for ^{123}I and ^{125}I.

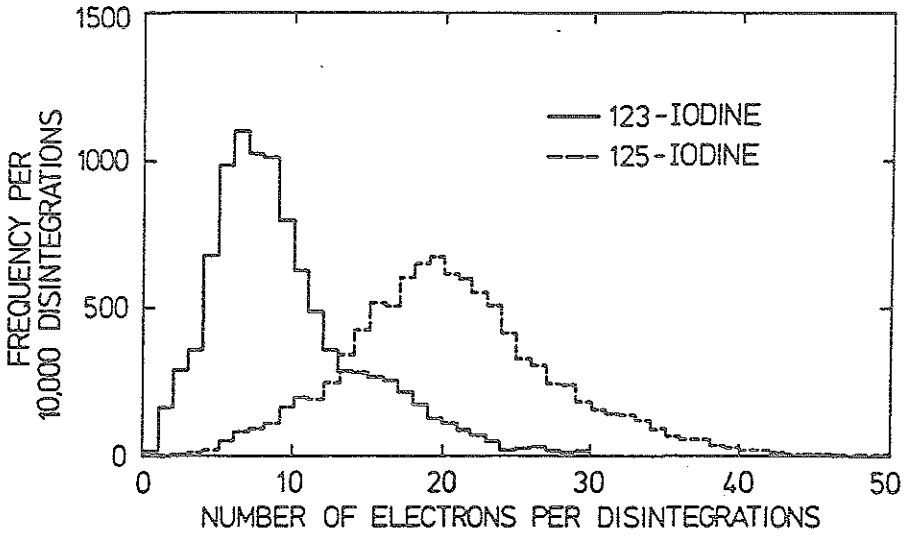

Figure 15
Electron number spectra for ^{125}I for 3 different phases: as an isolated atom, as methyl iodide and in the condensed phase.

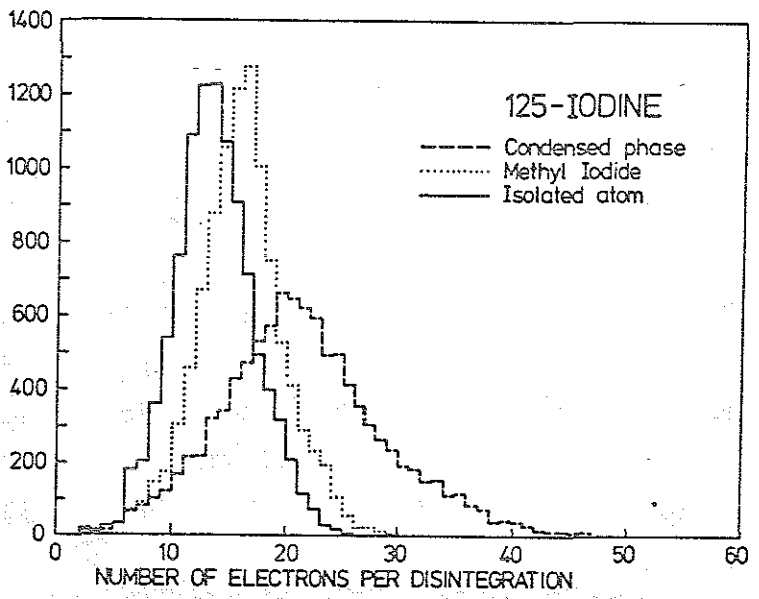

^{125}I (condensed phase calculations) are given in table 4. The effect of neutralization on the electron spectra is to increase the intensity of the low energy Auger and Coster-Kronig electrons.

For energy deposition calculations statistical information about the number of electrons and the amount of electron energy released for single disintegrations is required. This information is presented for 10,000 simulated decays of ^{123}I and ^{125}I in form of a 3 dimensional plot of frequency against electron number and energy (figure 16 and 17). For example if in the first cascade 8 keV is emitted as electron energy distributed among 10 electrons, then the first point would be (8, 10, 1) where the z coordinate represents the frequency of occurrence of this event. The index z is increased by one each time a decay is repeated in which 10 electrons are emitted carrying an energy of 8 keV. Figures 16 and 17 give therefore a relative frequency distribution of the different decay possibilities for ^{123}I and ^{125}I respectively.

The data in both graphs are arranged in various discrete groups representing the most probable de-excitation pathways through the tellurium atom after the decay of ^{123}I and ^{125}I. The highest energy group corresponds to those disintegrations in which the maximum electron energy is emitted, i.e. a double cascade with no fluorescence escape. The lower groups arise from both single and double cascades with various possible combinations of escape peaks, e.g. a single cascade with and without X-ray fluorescence escape, a double cascade with fluorescence escape in a single or in both cascades, electron capture in the L shell and a second cascade or gamma emission instead etc.

Such a representation of the data although relatively complex gives a more realistic picture of that to which the immediate enviroment of a decaying radionuclide is exposed. Individual cases can vary enormously but it is the individual spectra which lead to the biological effect.

The average values for the number of electrons and

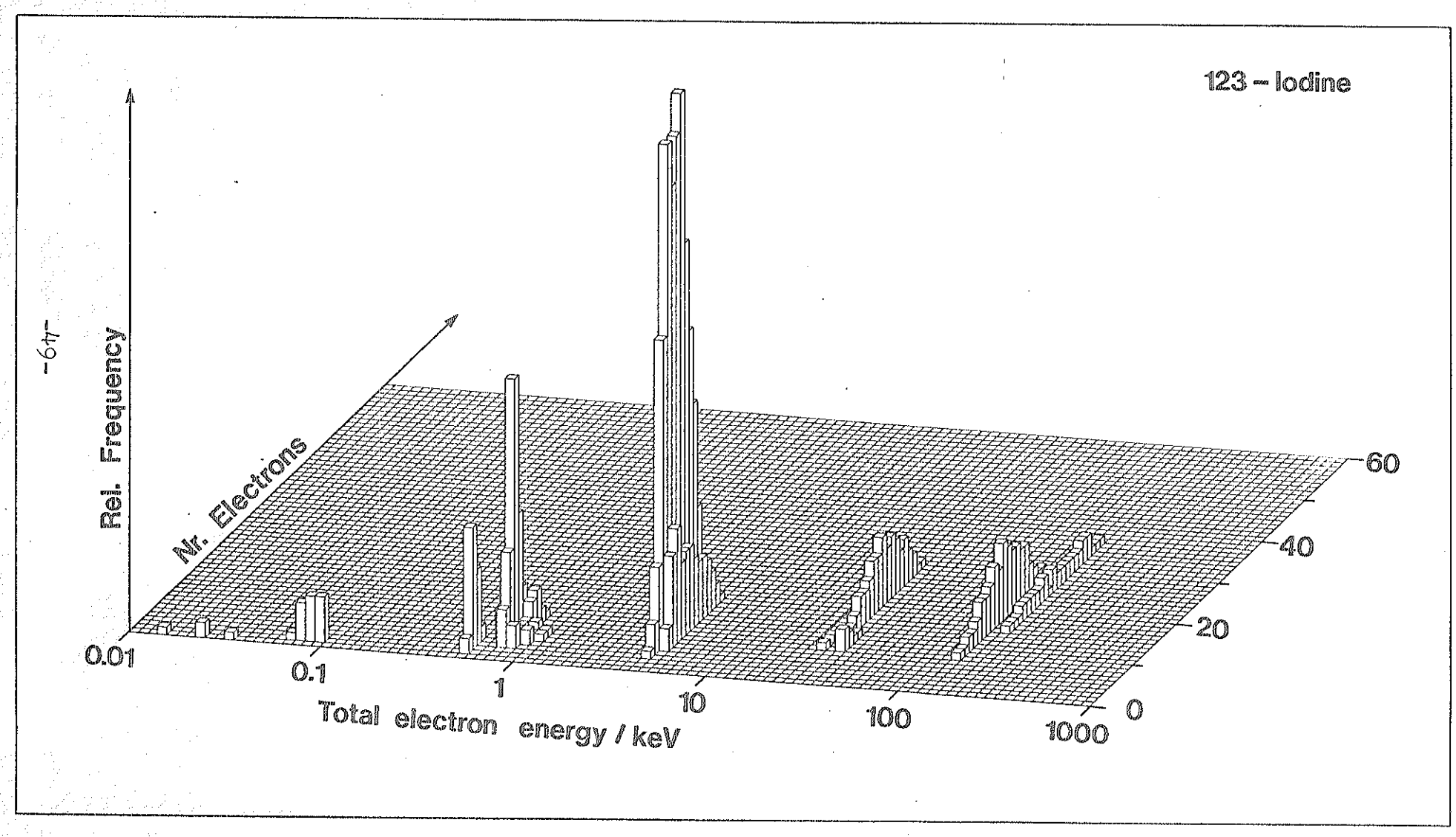
123 - Iodine
Rel. Frequency
Nr. Electrons
0.01
0.1
1
10
100
1000
Total electron energy / keV
0
20
40
60

Figure 16 (previous page)
3D histogram for ^{123}I of the relative frequency for the emission of M electrons with an energy E per decay.

Figure 17
3D histogram for ^{125}I of the relative frequency for the emission of M electrons with an energy E per decay.

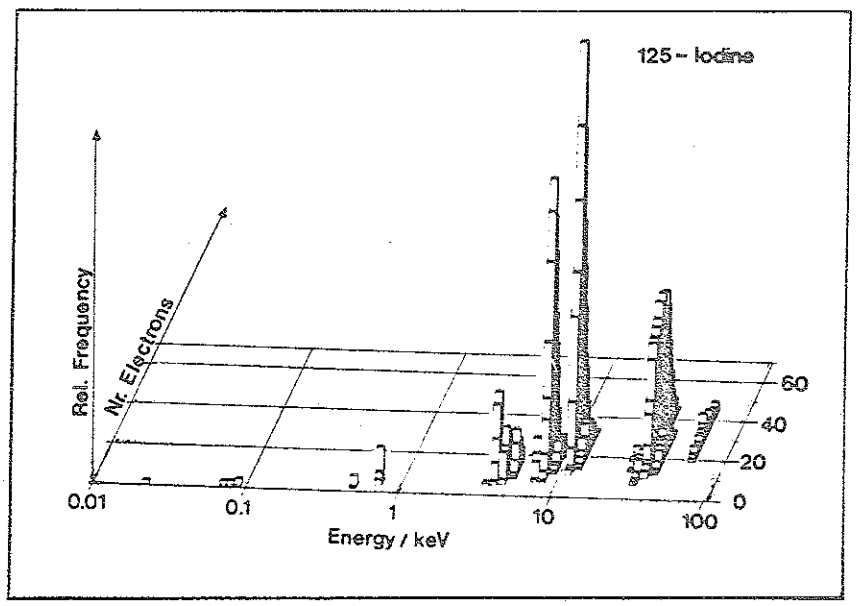

the electron energy per disintegration, $\bar{n}$ and $\bar{E}$, may represent a completely untypical disintegration. For the case ^{123}I, not even a single disintegration in 10,000 produces an electron number or energy which approximates the average value $\bar{n}$=12.3, $\bar{E}$=28.36.

In conclusion it has been shown that considerable care must be taken when using average values for energy deposition calculations from the decay of radionuclides since the response of a biological system will depend on the characteristics of the individual decays.

4.2.4 Energy deposition events around a decaying iodine radionuclide

Each individual disintegration produces a number of electrons M of energies E_1 to E_M. These electrons converge from the decay site (almost a point source) and undergo a series of interactions with the medium until their energy is reduced to the point where they are no longer able to produce any further ionizations or excitations. Using the electron energy data from individual decays track structure calculations can be performed giving the spatial structure of energy deposition events in the medium.

Figure 18 shows an example of the electron tracks produced by a disintegration of iodine in which 13 electrons were emitted [15, 16]. The centre of the picture is the position of the iodine. The concentric circles around the source depict a logarithmic scale with the inner ring enclosing all events which occur within a one nanometer radius of the iodine atom. The ionization events are represented by squares, the excitations by crosses. The biological effect is the result of a chain of processes which begin with the ionization and excitation events such as those

[15] Calculation of electron tracks performed by H.Paretzke, GSF Neuherberg, München

[16] In figure 18 the 3 dimensional track has been projected into a 2 dimensional plane

I - 125

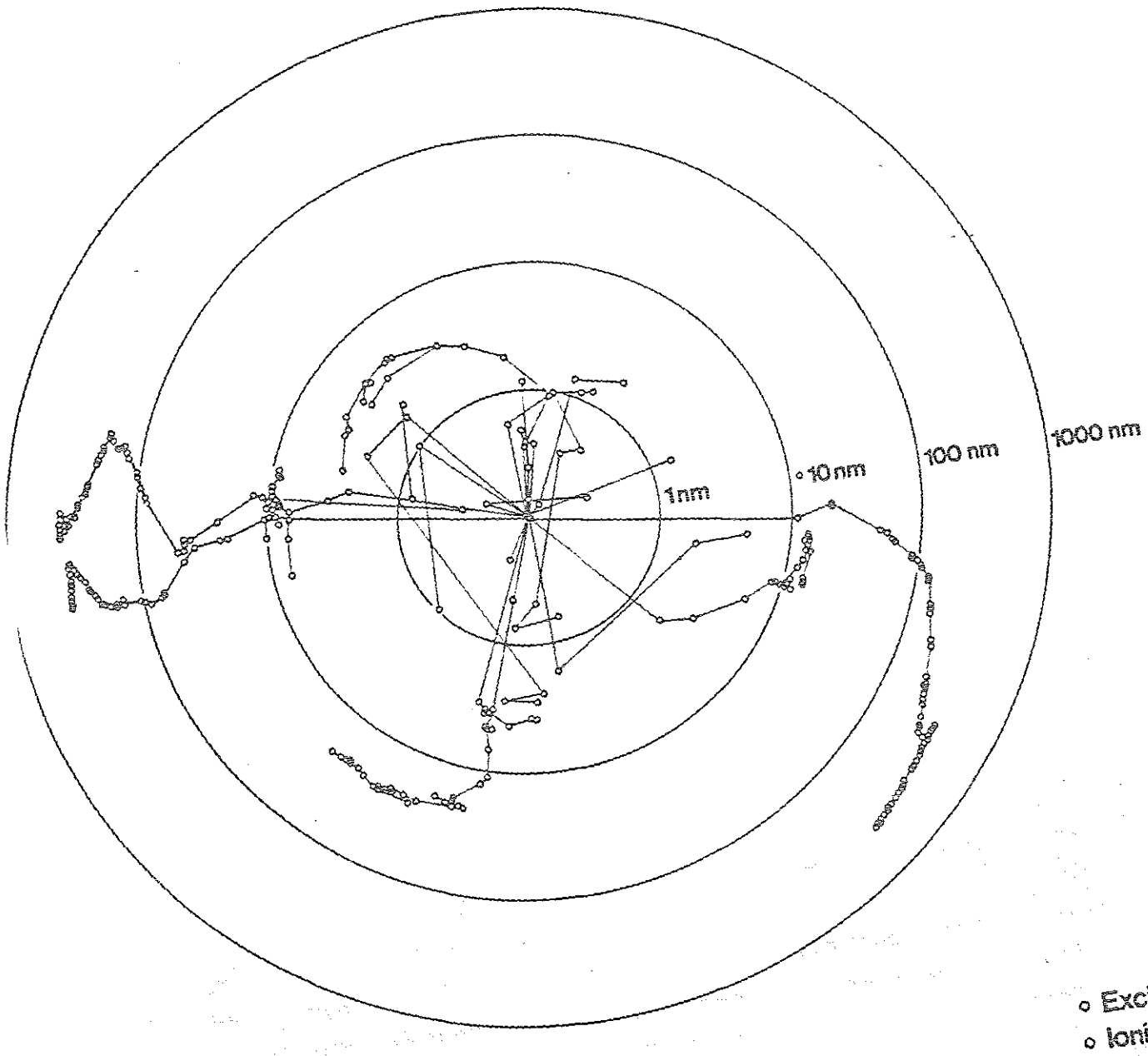

in figure 18.

4.3 The case of the molecule : a test of the Monte-Carlo calculations and the neutralization model

4.3.1 The Carlson and White experiment with CH_3I^{125}

So far the results have been presented for the radioisotopes ^{123}I and ^{125}I as isolated atoms and in the condensed phase. The average electron and photon energies obtained are in close agreement with the values of Dillmann and Van der Lage (table 4). However, a further important test would be with regard to the number of electrons emitted and the charge remaining on the tellurium daughter atom.

Fortunately some experimental data is available from Carlson and White, 1963, who measured the charge distribution on the molecular components of CH_3I^{125} after the decay of ^{125}I. They found the decay of ^{125}I extremely molecularly destructive, only 1% the molecules remaining intact after the decay. Using a specially designed mass spectrometer they were able to measure the charge abundance of the various ionic fragments. The charge distribution they obtained on the tellurium daughter is shown in figure 19 in comparison with the results from Monte-Carlo calculations with a neutralization treatment now to be described.

4.3.2 Calculation of the charge distribution on the tellurium after decay of CH_3I^{125}

The process of neutralization when a radionuclide is bound to a molecule is different from the condensed phase situation in two ways. Firstly the charge build-up on the tellurium atom is not dispersed into a medium but becomes shared with the ligand. This means that a certain balance is maintained between the positive charge on the tellurium atom and the rest of the molecule. Secondly since a positive charge builds up on both the tellurium

and the ligand eventually the molecule will fragment due to charge repulsion and the source of neutralization electrons for the tellurium ion will be cut off.

In the calculations presented here for CH_3I^{125} the neutralization programme was modified to consider both the above mentioned points in the following way. Once the charge difference between the tellurium atom the ligand is greater than one a neutralization electron is transferred from the ligand to an outer shell of the tellurium. For example at the start of the vacancy cascade the charge on the molecule is zero. The charge then begins to build-up on the tellurium. When it reaches +2 an electron is transferred from the ligand to maintain a charge balance on the molecule. The charge is now distributed on the molecule being equal to +1 on both tellurium and ligand. Further charge build-up occurs on the tellurium until +3 when the charge difference is again two, therefore once again there is neutralization and so the process repeats until at some point the molecule ruptures. This cut-off criteria defining the maximum number of electrons which can be used for neutralisation before molecular fragmentation has been set at a constant value of 7. Although the methyl group CH_3 consists in total of 9 electrons, (6 associated with the carbon atom and 1 with each hydrogen atom) the 2 inner shell 1s electrons of carbon were assumed not available to participate in any neutralization.

This neutralization model is of course a very simple representation of what in reality is an extremely complex process. Nevertheless the results thereby obtained for the charge distribution on the tellurium are in extremely good agreement to the experimental distribution measured by Carlson and White (figure 19). The peaks of both distributions differ by a charge of only one i.e. in the programme neutralization is slightly overestimated. However the averages of the distributions are in close agreement, the Monte-Carlo calculations yield 11.1 to Carlson 11.3. Attempts to improve agreement by the use of an alternative cut-off limit to 7, such as 6, or to use a

variable limit determined by a binomial function, did not improve agreement.

Further tests of the programme calculations were performed with data for photoelectric induced inner shell vacancies in the iodine of methyl iodide for which also experimental data is available. This is a more appropriate test since in this case there is only a single cascade in an iodine atom. Since the details of photoelectric induced vacancy cascades is primarly the subject of Part II of this thesis, to avoid a lack of continuity these results and their comparison with experiment are presented in appendix 5.

Figure 19
Comparison of the charge distribution on tellurium following the decay of CH_3I^{125} with the experimental results of Carlson and White.

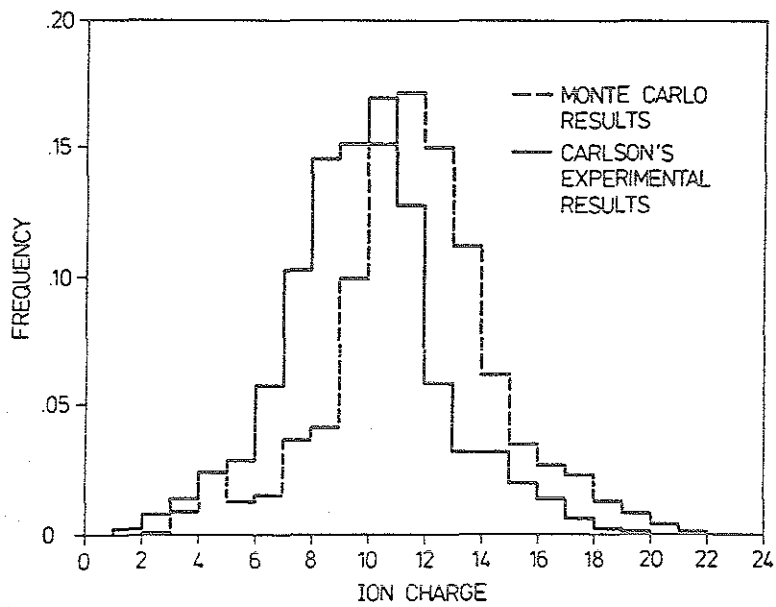

5 The radionuclides iron-55 and copper-64

The decay schemes of ^{55}Fe and ^{64}Cu were discussed in section 1.1 and the general method of computation of the electron and photon spectra the subject of section 3. This chapter will therefore be devoted to a presentation and discussion of the results obtained from calculations for these two isotopes. Section 5.1 is concerned with the number of electrons and photons emitted per disintegration and section 5.2 concentrates on their energies.

5.1 Electron and photon numbers

5.1.1 Iron-55

The radioisotope ^{55}Fe decays 100% by a single electron capture pathway to the ground of manganese. The electron and photon output data are therefore the result of a single electron capture induced vacancy cascade. The number of electrons which can be released in a single disintegration of ^{55}Fe ranges from 0 - 13 and the average number released per disintegration $\bar{n}$ amounts to 4.75 electrons. A frequency distribution of the electron number for 10,000 Monte-Carlo simulated disintegrations of ^{55}Fe is given in table 5 and in figure 20 in graphical form.

Most notable is that the number of electrons released after the decay of ^{55}Fe is far less than for ^{123}I or ^{125}I, even if the comparison is made with the results of the first cascade only. This results from the smaller size of the iron daughter manganese (atomic number 25) with filled orbitals up to the N_1 sub-shell. The iodine electron capture daughter tellurium possesses over twice as many electrons (atomic number 52) and has electrons in orbitals up to the O_3 sub-shell. It is the Coster-Kronig transitions between the outer sub-shells which produce a significant rise in the electron emission intensity.

Also the effect of chemical phase is important for the electron emission spectrum of an iodine radioisotope,

yet for ^{55}Fe and ^{64}Cu the influence of neutralization is very small (the difference in the average electron number $\bar{n}$ between the isolated atom and the condensed phase is a mere fraction of an electron). For this reason all results presented in this chapter are for the condensed phase situation i.e. the case of radionuclide incorporation.

Finally the average number of photons emitted per ^{55}Fe disintegration is 0.26. This results from the product of the fluorescence yields of the K and L shells for manganese (ω_K = 0.308 and ω_L = 0.011, Krause, 1979) to the probability of electron capture in those shells (see table 2, section 3.2.1).

5.1.2 Copper-64

The average number of electrons released per ^{64}Cu decay is determined by two factors. Firstly in 41.1% of the disintegrations decay is by electron capture resulting in a statistical distribution in the number of emitted electrons. Secondly the other 59.9% of the disintegrations are by beta decay where just one electron is emitted. From Monte-Carlo calculations an average number of Auger electrons 3.9 per electron capture event was obtained. Therefore the average number of electrons per ^{64}Cu decay is (3.9 x 0.411) + (1.0 x 0.589) which equals 2.2. The frequency distribution of the number of electrons emitted for 10,000 simulated decays of ^{64}Cu is given in table 5 for comparison with ^{55}Fe and again in figure 20 in graphical form. The large number of disintegrations in which only one electron is emitted is predominently the result of the beta decay component.

The photon emission frequency for ^{64}Cu is determined primarily by the number of X-ray transitions in the nickel daughter atom when decay is by electron capture and amounts to 0.137 photons per decay.Not all the electron capture decays of ^{64}Cu however fall directly to the ground state but a small fraction 0.006 arrive at a highly excited metastable level of nickel. Therefore to the

Figure 20

Electron number distributions for ^{55}Fe and ^{64}Cu.

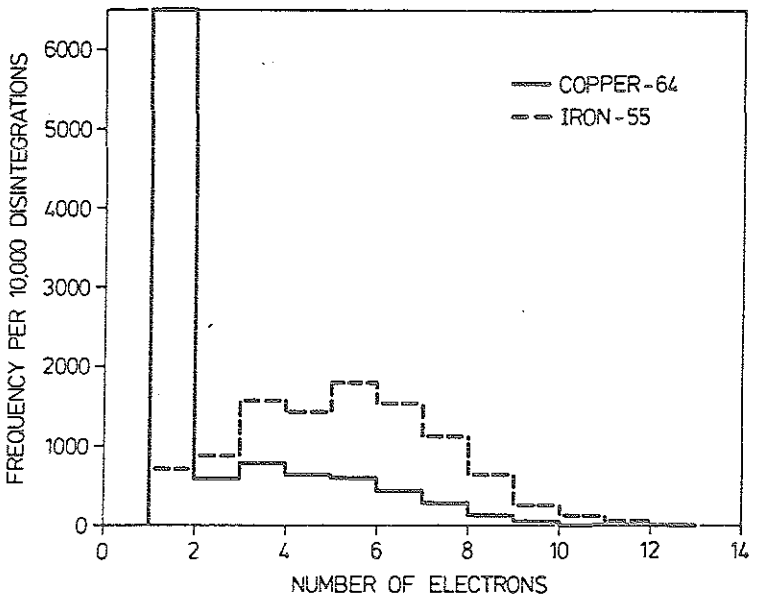

photon number there is a small additional gamma contribution (0.006 per decay) accounting for the de-excitation of the nickel nucleus.

Table 5
Frequency per 10,000 disintegrations of the electron emission number for ^{55}Fe and ^{64}Cu in condensed phase.

m	^{55}Fe	^{64}Cu
0	3	0
1	706	6498
2	864	584
3	1552	781
4	1427	628
5	1778	599
6	1521	432
7	1110	278
8	624	126
9	253	49
10	113	16
11	37	5
12	9	4
13	3	0

5.2 Electron and photon energies

5.2.1 Iron-55

The electron and photon energy contributions for the decay of ^{55}Fe are the statistical result firstly of the probability of electron capture in the various electron orbitals (this determines the maximum energy ejected in a vacancy cascade) and secondly the course of the vacancy cascade process itself. The average total energy released per decay of ^{55}Fe has been calculated from 10,000 simulated disintegrations and amounts to 5.70 keV (see table 6). This total energy released is composed of the energy emitted in form of Auger electrons and from X-ray photons. From calculations the average energy released as Auger electron energy per decay is 4.04 keV and as X-ray photon energy 1.66 keV per decay (table 6). Important is, for the biological enviroment, that a greater proportion of the electron capture decay energy for ^{55}Fe is

emitted in form of Auger electrons i.e. short range densely ionizing particles and only about 30% as photon energy.

Once again as for ^{123}I and ^{125}I in order to visualize better the number of electrons and the electron energy released for 10,000 individual ^{55}Fe electron capture events a 3 dimensional representation of frequency versus electron number and energy is presented (figure 21). This figure shows the statistical distribution of the electron spectra to which the local medium around an incorporated ^{55}Fe radionuclide is subject. For ^{55}Fe three discrete electron energy groups are distinguishable : between 5.5 - 6.6 keV corresponding to electron capture in the K-shell followed by a completely non-radiative de-excitation of the atom, between 600 - 700 eV corresponding to either electron capture in the L-shell or K-capture with KL fluorescence escape and finally a very low probability group between 35 - 55 eV from electron capture in the M-shell or K-capture with KM fluorescence escape.

The photon spectrum for ^{55}Fe consists of the characteristic X-ray spectrum for the iron daughter manganese and is basically only the K_α and K_β lines of that element, (average photon energy per decay 1.66 keV).

Table 6
Data for the decay of iron-55

Average No. of Auger electrons per electron capture event 4.75
Average Auger electron energy per electron capture event 4.04 keV
Average photon energy per electron capture event 1.66 keV
Average total energy emitted per electron capture event 5.70 keV

Figure 21
3D histogram for ^{55}Fe of the relative frequency for the emission of M electrons with an energy E per decay.

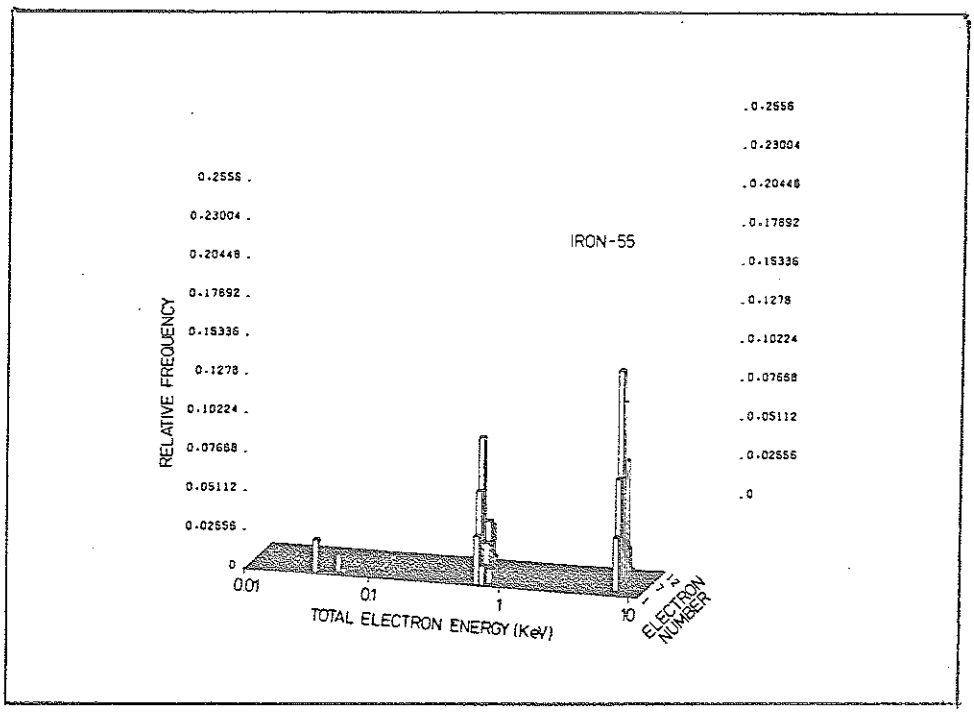

Figure 22 (next page)
3D histogram for ^{64}Cu of the relative frequency for the emission of M electrons with an energy E per decay.

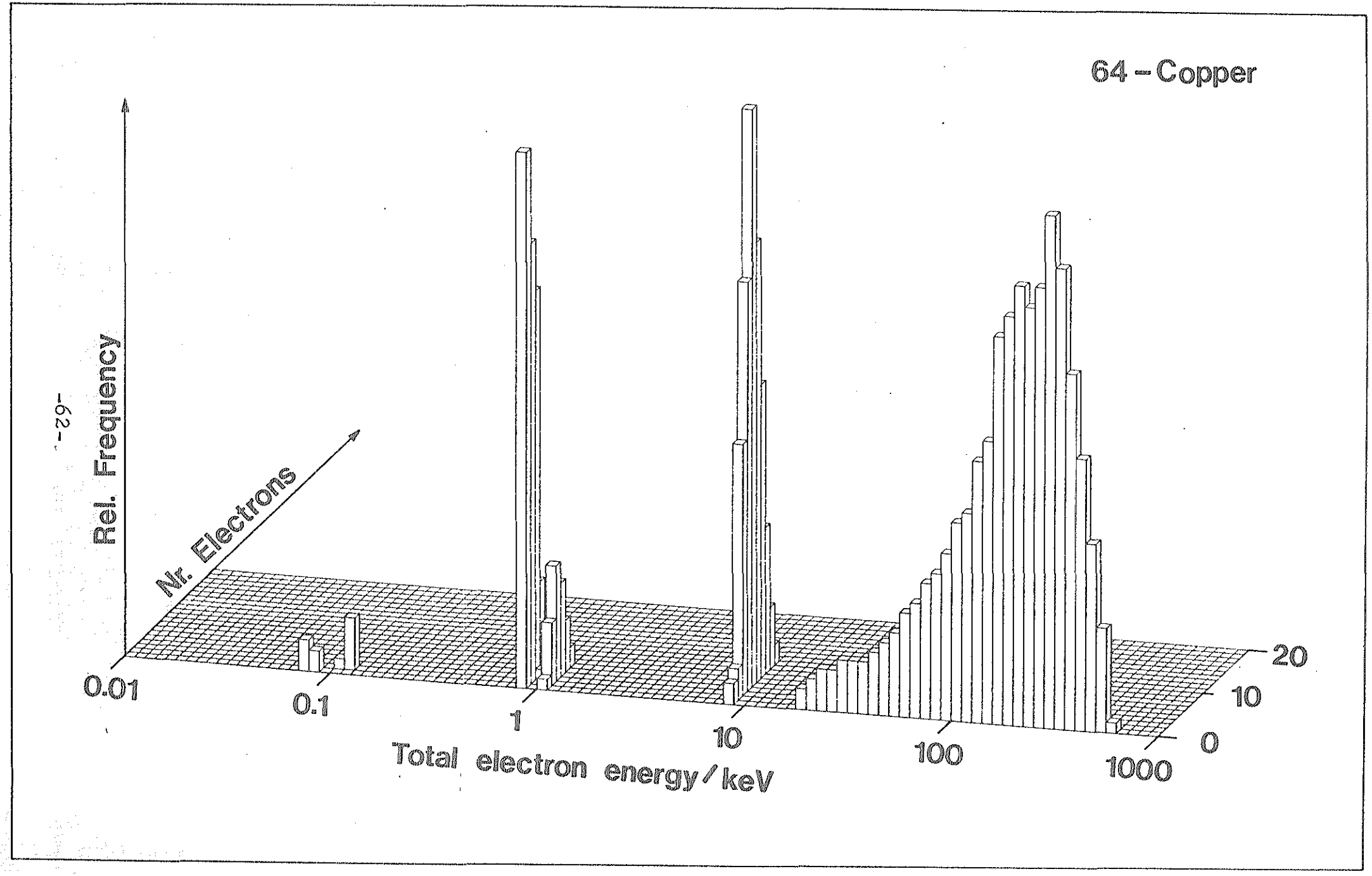
64 – Copper
Rel. Frequency
Nr. Electrons
0.01
0.1
1
10
100
1000
Total electron energy / keV
0
10
20

5.2.2 Copper-64

The electron and photon spectra for ^{64}Cu are slightly more complicated than for ^{55}Fe since both are composed of two components. For ^{64}Cu the electron spectrum consists of the relatively low energy Auger electrons which are emitted when the copper decays by electron capture (41.1%) together with a beta spectrum produced by the other 58.9% of the decays. The average Auger electron energy per electron capture induced vacancy cascade has been calculated as 4.68 keV and the average beta energy 218.2 keV. This data has been combined as in table 7 to give the average total electron energy per ^{64}Cu disintegration. However an average electron energy per disintegration for a radionuclide with a branched decay scheme can for energy deposition purposes lead to a misleading estimation of the radiotoxicity of such a radionuclide. Therefore once again a 3 dimensional representation of 10,000 ^{64}Cu disintegrations of electron number and energy against decay event frequency is given in figure 22 demonstrating the wide variation in electron energy release from such a radionuclide. The discrete energy groups below 10 keV are the result of decays by electron capture and the continuous spectrum between 118 - 600 keV the combined electron-positron spectrum.

As mentioned above the photon energy spectrum ^{64}Cu also consists of two components : the characteristic X-ray spectrum of nickel (average energy 3.1 keV) plus a 1.346 MeV gamma photon due to de-excitations of 0.6% of nickel nuclei. The two together yield an average photon energy per decay of 9.35 keV (table 7).

Table 7

Data for the decay of copper-64

Electron capture events (probability 0.411)
Average no. of Auger electrons per electron capture event
3.9
Average Auger electron energy per electron capture event
4.68 keV
Average photon energy per electron capture event
3.1 keV
Average gamma energy per electron capture event
19.65 keV
$Beta^+$ - $Beta^-$ events (probability 0.589)
Average no. of betas per beta event
1.0
Average beta energy per beta event
218.2 keV

The data given above are now combined to give values per disintegration.

Per disintegration
Average no. of electrons
3.9 x 0.411 + 1.0 x 0.589 = 2.2
Average total electron energy
4.68 x 0.411 + 218.2 x 0.589 = 130.4 keV
Average total photon energy
3.1 x 0.411 + 1346 x 0.006 = 9.35 keV
Average total energy
130.4 + 9.35 = 139.8 keV

6 Calculation of the energy deposition from Auger emitting radionuclides

A Monte-Carlo programme was developed to calculate the Auger electron energy spectra emitted from individual disintegrations of the radioisotopes ^{123}I, ^{125}I, ^{55}Fe and ^{64}Cu. 10,000 decay spectra were recorded on magnetic tape for each isotope. These spectra were used to calculate the energy deposition for a homogenous source distribution in spherical volumes of variable diameter between 1 nm and 10 µm.

6.1 Energy imparted, lineal energy and their averages

In the new ICRU report on Microdosimetry the energy imparted E to matter in a volume V is defined as the summation of all individual energy deposits ϵ_i in that volume.

$$\epsilon = \sum_i \epsilon_i \qquad (14)$$

In figure 23 a volume V is illustrated in which a radioisotope has been randomly placed (incorporated). As a result of the decay of this radioisotope electrons and photons are emitted which create ionizations, i.e. deposit energy, both within the sensitive volume V and outside of it. As given by equation 14 the energy imparted in V is the sum of the individual energy deposits within V.

Figure 23
Schematic diagram of the radionuclide ^{123}I decaying within a sensitive volume.

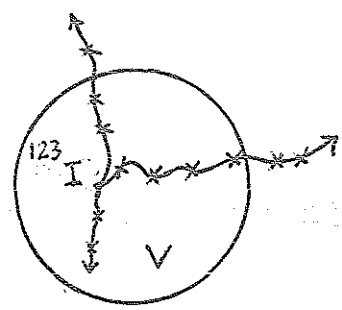

Inherent in the statistical nature of decay and the spatial distribution of the radionuclide in V, there is a certain statistical fluctuation in the energy imparted to the volume V. The mean energy imparted for n decaying radionuclides is then,

$$\bar{\epsilon} = \frac{1}{n} \sum_{x=1}^{n} \epsilon_x \qquad (15)$$

A further important quantity in microdosimetry is the lineal energy y which is defined as the ratio of the energy imparted in a volume V to the mean chord of the volume [17] (ICRU Microdosimetry).

$$y = \frac{\epsilon}{\bar{d}} \qquad (16)$$

Like energy imparted, ϵ, the lineal energy is also a stochastic quantity, i.e. is independent for each decay. For n source decays the mean lineal energy is,

$$\bar{y}_F = \frac{1}{n\bar{l}} \sum_{x=1}^{n} \epsilon_x \qquad (17)$$

where y_F is denoted the frequency-mean lineal energy and $\bar{l}$ is the mean chord length of V.

6.2 Calculation of $\bar{\epsilon}_f$ and $\bar{y}_F$

The calculation of the mean energy imparted and lineal energy for a homogeneous radioisotope distribution in a spherical volume V, mean chord length $\bar{l}$, has been performed with the aid of Bergers point kernel data. A point kernel is a differential function representing the distribution of absorbed dose around isotropic point sources of electrons as a function of distance from the source, where to assist interpolation the distance is scaled in terms of the mean

[17] The mean chord length of a spherical volume is 2/3 d where d is the sphere diameter (ICRU Microdosimetry).

(c.s.d.a.) [18] range r_o at the source energy E_o (Berger 1973, Berger 1974). The mathematical definition of a scaled point kernel $F(r/r_o, E_o)$ as given by Berger is

$$F(r/r_o, E_o)\, d(r/r_o) = 4\pi\rho\bar{\phi}(r, E_o)\, r^2\, dr \qquad (18)$$

where $\bar{\phi}(r, E_o)$ is the fraction of emitted energy E_o absorbed per unit mass of the medium in a spherical shell between r and r+dr and $4\pi r^2 dr\rho$ is the mass of the spherical shell. Then the fraction $\epsilon/E_o(d, E_o)$ of emitted energy absorbed in a sphere [19] of diameter d is given by the integral over the point kernel between 0 and d multiplied by the geometric reduction factor [20].

$$\frac{\epsilon}{E_o}(d, E_o) = \frac{1}{r}\int_o^d \left[1 - \frac{3}{2}\left(\frac{r}{d}\right) + \frac{1}{2}\left(\frac{r}{d}\right)^3\right] F\left(\frac{r}{r_o}, E_o\right) dr \qquad (19)$$

Berger 1974, has given a tabulation of ϵ/E_o for electron energies from 0.5 keV - 10 MeV and for site diameters from 2 - 14 µm. Using the data of Berger, Charlton et al 1978, have plotted ϵ/E_o as a function of $R/\bar{l}$ (95% electron range in proportion to the volume mean chord length) and made a best fit with third order polynomials in 3 sections.

$$\left(\frac{\epsilon}{E_o}\right)^{-1} = c_o + c_1\left(\frac{R}{\bar{l}}\right) + c_2\left(\frac{R}{\bar{l}}\right)^2 + c_3\left(\frac{R}{\bar{l}}\right)^3 \qquad (20)$$

where

$c_o = 1.000582435$, $c_1 = 0.517285702$, $c_2 = 0.281280963$, $c_3 = 0.135740727$ for $0 \leq R/\bar{l} \leq 1$;

$c_o = 2.326798619$, $c_1 = -2.48168182$, $c_2 = 2.485804861$, $c_3 = -0.36473284$ for $1 \leq R/\bar{l} \leq 3$;

$c_o = -2.23591098$, $c_1 = 3.35376742$, $c_2 = 0$, $c_3 = 0$ for $3 \leq R/\bar{l} \leq 30$

[18] c.s.d.a. continuous slowing down approximation.

[19] In Bergers notation ϵ/E_o (d, E_o) is written $A(d, E_o)$.

[20] The geometric reduction factor, U(x), for internal source randomess in a sphere is $[1-3/2\ (r/d)+1/2\ (r/d)^3]$ Kellerer 1981.

The value of $\bar{\epsilon}_F$ and $\bar{y}_F$ can then be calculated for each radioisotope separately by summing over all the stored individual decay spectra.

$$\bar{\epsilon}_F = \sum \frac{\epsilon_i}{E_o} \cdot E_o \qquad (21)$$

and

$$\bar{y}_F = \frac{1}{l} \sum \frac{\epsilon_i}{E_o} \cdot E_o \qquad (22)$$

6.3 Results of energy deposition calculations

When considering local energy deposition the influence of chemical phase is once again important. Of prime concern in radionuclide incorporation are the results for the condensed phase situation where the potential energy build-up on the decaying atom is rapidly dispersed in the medium in the form of additional electron energy. For the isolated atom the charge produced on the atom following a vacancy cascade can represent a large potential energy which since located at the site of decay represents a considerable contribution to the local energy deposition. However the case of the isolated atom is rather artificial since by definition no molecular damage can be produced. Nevertheless a certain charge build-up may occur when the radionuclide decays in a medium in which electron transport is difficult, with the potential of producing severe local damage to the immediate enviroment. Damage from the charge effect differs from that produced by Auger electron energy deposition in that it occurs directly at the site of incorporation whereas Auger electrons can produce molecular damage at some distance from the decay site.

To be discussed here are primarily the results for the condensed phase situation i.e. the Auger contribution to energy deposition. However for both radioisotopes ^{123}I and ^{125}I isolated atom data is given with the inclusion of the atomic potential energy remaining at the decay site.

In tables 8 and 9 and graphically in figures 24 and 25 are given the results of calculations for the mean

energy deposition $\bar{\epsilon}_F$ for ^{123}I, ^{125}I and ^{55}Fe, ^{64}Cu respectively (condensed phase) in site diameters from 1 nm - 10 µm. Also given are the standard deviations of ϵ as a measure of the broadness of the energy deposition distribution and the frequency mean lineal energy $\bar{y}_F$ in units of keV/µm.

The local energy deposition is highest for ^{125}I at all site diameters ranging from 113 eV at a site diameter of 1 nm i.e. biomolecular dimensions, to nearly 12 keV at 10 µm i.e. the order of magnitude of a cell nucleus. The energy deposition per ^{123}I decay is only about one half that of ^{125}I in site sizes to 10 µm. However the distribution of ϵ for ^{125}I is broader as can be ascertained from the higher standard deviation about the mean energy deposition for this isotope.

The average energy deposition per ^{55}Fe or ^{64}Cu disintegration is considerably smaller than for the iodine radioisotopes. For ^{55}Fe $\bar{\epsilon}_F$ is 24 eV for a 1 nm site diameter and goes up to 3.81 keV for a diameter of 10 µm. For ^{64}Cu $\bar{\epsilon}_F$ is even smaller being only 3 eV for 1 nm and 2.861 keV for 10 µm site diameters respectively. The influence of the copper beta rays is to produce a much broader energy deposition distribution for this radioisotope where the standard deviation of ϵ is even greater than its mean value at the smaller site diameters.

For all ϵ_F values the corresponding $\bar{y}_F$'s are also given calculated by multiplying the $\bar{\epsilon}_F$ value by the mean chord length of a sphere (2d/3).

In table 10 and then graphically in figure 26 isolated atom data for the radionuclides ^{123}I and ^{125}I is also presented. For each site size the electron energy deposition is given separately together with the total energy deposition i.e. the electron contribution plus the average potential energy of the remaining charged atom (0.74 keV for ^{123}I and 1.8 keV for ^{125}I).

Table 8

Energy deposition data for ^{123}I and ^{125}I condensed phase

	Iodine-123			Iodine-125		
d/um	$\bar{\epsilon}_f$/keV	σ_ϵ	y_F/keVum^{-1}	$\bar{\epsilon}_f$/keV	σ_ϵ	y_F/keVum^{-1}
0.001	0.066	0.035	99.4	0.113	0.038	169.3
0.0018	0.123	0.066	104.0	0.211	0.072	177.9
0.0032	0.202	0.111	95.9	0.347	0.123	164.6
0.0056	0.301	0.168	80.2	0.517	0.188	137.8
0.010	0.423	0.238	63.4	0.729	0.267	109.3
0.018	0.604	0.335	51.0	1.046	0.372	88.21
0.032	0.879	0.475	41.7	1.531	0.521	72.63
0.056	1.158	0.624	30.89	2.045	0.683	54.56
0.100	1.406	0.768	21.09	2.540	0.847	38.11
0.178	1.722	0.968	14.53	3.226	1.088	27.21
0.316	2.279	1.339	10.81	4.537	1.557	21.52
0.562	3.023	1.839	8.065	6.487	2.226	17.30
1.000	3.600	2.250	5.401	8.099	2.791	12.15
1.778	3.994	2.566	3.369	9.178	3.198	7.742
3.102	4.297	2.872	2.038	9.948	3.548	4.718
5.623	4.639	3.355	1.237	10.712	4.079	2.856
10.000	5.214	4.397	0.782	11.914	5.324	1.786

Table 9

Energy deposition data for ^{55}Fe and ^{64}Cu

	^{55}Fe			^{64}Cu		
d/um	$\bar{\epsilon}_f$/keV	σ_ϵ	y_F/keV/um^{-1}	$\bar{\epsilon}_f$/keV	σ_ϵ	y_F/keVum^{-1}
0.001	0.024	0.011	35.56	0.003	0.006	5.124
0.0018	0.047	0.021	39.26	0.007	0.011	5.554
0.0032	0.077	0.034	36.32	0.012	0.021	5.765
0.0056	0.108	0.047	28.92	0.019	0.033	5.198
0.010	0.150	0.062	22.52	0.029	0.047	4.422
0.018	0.229	0.092	19.34	0.047	0.070	3.924
0.032	0.394	0.156	18.67	0.084	0.123	3.971
0.056	0.610	0.243	16.27	0.155	0.229	4.135
0.100	0.787	0.324	11.81	0.234	0.346	3.508
0.178	0.944	0.410	7.96	0.305	0.446	2.576
0.316	1.140	0.543	5.41	0.389	0.558	1.802
0.562	1.528	0.844	4.08	0.528	0.752	1.409
1.000	2.248	1.416	3.37	0.802	1.152	1.203
1.778	2.944	1.969	2.48	1.252	1.811	1.056
3.102	3.395	2.333	1.61	1.703	2.375	0.808
5.623	3.660	2.549	0.976	2.184	2.826	0.583
0.000	3.810	2.671	0.572	2.861	3.363	0.429

Table 10

Energy deposition data for ^{123}I and ^{125}I isolated atom

	Iodine-123		Iodine-125	
d/ um	$\bar{\epsilon}_F$/keV	$\bar{\epsilon}_T$/keV	$\bar{\epsilon}_F$/keV	$\bar{\epsilon}_T$/keV [21]
0.0010	0.042	0.782	0.068	1.868
0.0018	0.081	0.821	0.131	1.931
0.0032	0.145	0.885	0.234	2.034
0.0056	0.233	0.973	0.379	2.179
0.0100	0.368	1.088	0.576	2.376
0.0181	0.525	1.265	0.885	2.685
0.032	0.797	1.537	1.366	3.166
0.056	1.076	1.836	1.878	3.678
0.100	1.324	2.064	2.374	4.174
0.178	1.642	2.382	3.067	4.867
0.316	2.202	2.942	4.398	6.198
0.562	2.952	3.692	6.380	8.180
1.000	3.533	4.273	8.019	9.819
1.778	3.929	4.669	9.113	10.913
3.162	4.233	4.973	9.890	11.690
5.623	4.575	5.315	10.654	12.454
10.000	5.147	5.887	11.847	13.647

[21] $\bar{\epsilon}_T$/keV is the total energy deposition including potential energy remaining on the charged atom.

Figure 24

Mean energy deposition $\bar{\epsilon}_F$ for ^{123}I and ^{125}I (condensed phase) as a function of the sensitive site diameter.

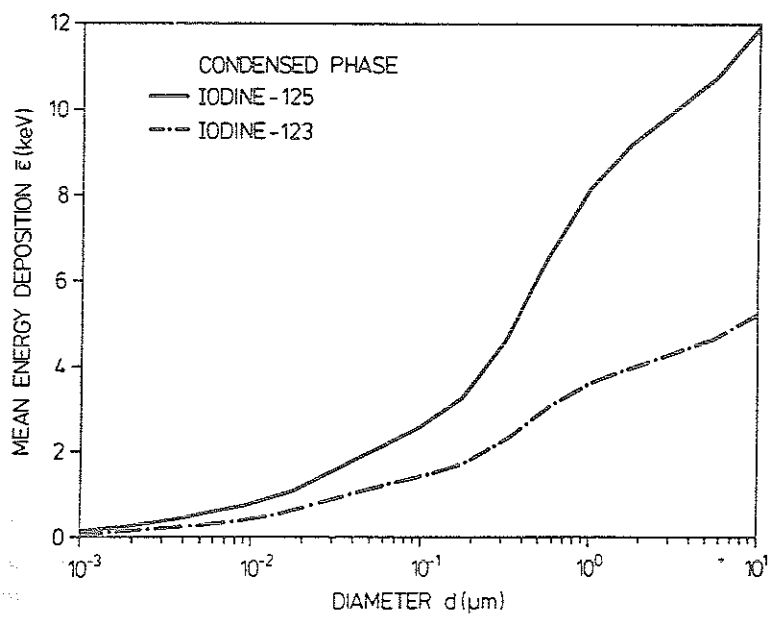

Figure 25
Mean energy deposition $\bar{\epsilon}_F$ for ^{55}Fe and ^{64}Cu (condensed phase) as a function of the sensitive site diameter.

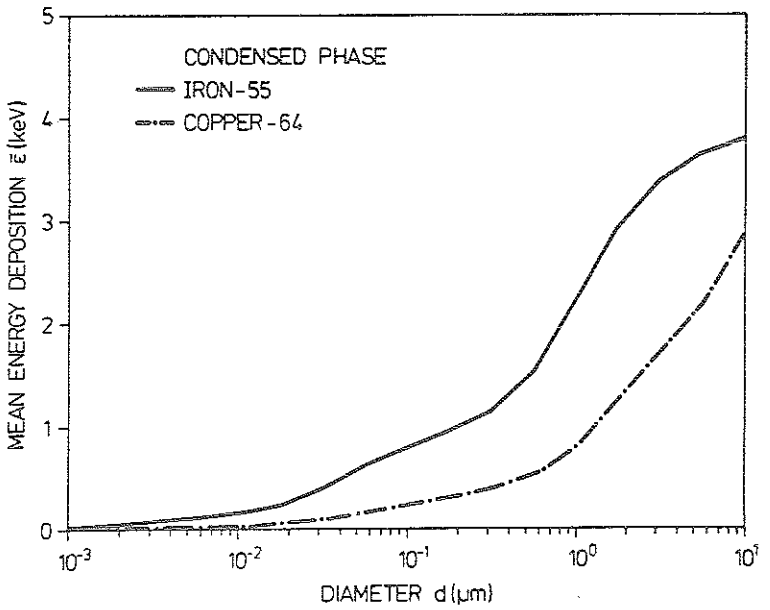

Figure 26
Mean energy deposition $\bar{\epsilon}_F$ for ^{123}I and ^{125}I as isolated atoms as a function of the sensitive site diameter; the electron contribution and the electron with potenial energy contribution.

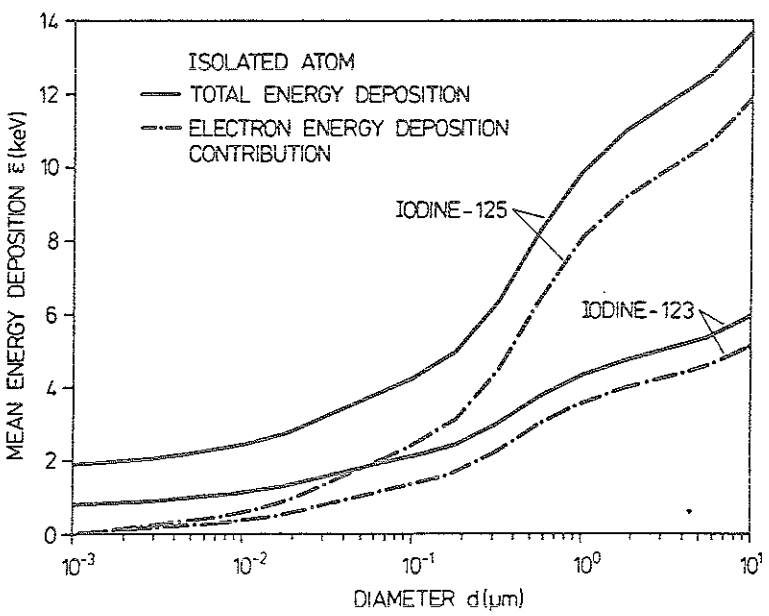

PART II

AUGER ELECTRON EMISSION INDUCED BY THE PHOTOELECTRIC EFFECT

7 Photon interactions in matter

Electromagnetic radiation in the energy range between 0 - 1 MeV interacts with matter by one of the three principal mechanisms.

1. Photoelectric effect
2. Compton or inelastic scattering
3. Raleigh or elastic scattering

The first results in a total absorption of the photon energy, the second in only partial absorption and a change in the photon direction and the third to only a change in photon direction with no energy absorption.

7.1 Photoelectric effect

The predominant form of photon absorption in biological media at energies below 200 keV is by photoelectric interaction. In a photoelectric interaction the incident photon energy $h\nu$ is totally absorbed by an atomic electron, binding energy B_e, which as a result is ejected with a kinetic energy T where

$$T = h\nu - B_e \qquad (23)$$

The emitted photoelectron, can only be released from a shell for which $h\nu > B_e$.

A monoenergetic photon flux incident on any element Z will interact predominantly with electrons in the most strongly bound shell for which $h\nu > B_e$.[22]
For example, for photons of energies above the K shell binding energy about 80% of the photoelectric interactions occur with K shell electrons and only 20% with all other shells. The distribution of inner shell vacancies produced by photoelectric interactions is important for determining the subsequent de-excitation steps in the atom and will be treated in detail in section 11.2.1.

[22] This results from the principle of conservation of momentum where the more weakly bound an electron, the less probable energy transfer becomes.

Once an inner shell vacancy has been produced in an atom a vacancy cascade process proceeds in the same way as in electron capture or internal conversion decay (see part I). Whereas Auger emission spectra are, for radionuclide decay, characteristic of the de-excitation process in the daughter product, for photoelectric interactions in a biological medium each individual spectrum depends on the atom of interaction and on the incident photon energy.

For a single atom the probability of photoelectric interaction is given by the photoelectric absorption cross section [23] which depends on the atomic number Z of the atom and on the photon energy $h\nu$ in approximately the following way.

$$\tau \simeq \text{const.} \frac{Z^4}{(h\nu)^3} \qquad (24)$$

In reducing the incident photon energy the photoelectric cross section increases very rapidly until the K shell binding energy of the atom. If the photon energy is reduced further, to energies below the K shell binding energy of Z, there is a sudden decrease in the photoelectric cross section due to the inability of photoelectric interactions with the K shell. The discontinuous decrease in the photoelectric cross section is referred to as an absorption edge or more specifically, the K, L, M edge etc.

The photoelectric cross section also increases very rapidly with increasing atomic number Z of the absorbing substance (equation 24). Since biological media consist predominantly of low Z elements : hydrogen, carbon, nitrogen and oxygen, a selective absorption effect may be possible if a high Z element is incorporated within the low Z medium. Therefore the problem under investigation was if such an effect could have important consequences in the case of high Z element incorporation in the sensitive targets e.g. DNA, of biological matter.

[23] The photoelectric absorption cross section of an atom is given by the sum of the photoelectric absorption cross sections for the individual electron shells.

7.2 Compton or inelastic scattering

In Compton scattering a photon interacts with a lightly bound (assumed free) electron transferring a certain fraction of its energy to it. As a result the photon undergoes a change in direction and a loss of energy. From the principles of conservation of energy and momentum it is possible to calculate a relation between the scattered photon energy, the energy transferred to the electron and the scattering angle of the photon (Evans 1955).

$$\frac{h\nu'}{h\nu} = \frac{1}{1 + \frac{h\nu}{m_e c^2}\left(1 - \cos\theta_p \right)} \qquad (25)$$

where $h\nu'$ = photon energy after interaction
$h\nu$ = incident photon energy
θ_p = photon scattering angle
m_e = electron mass
and c = velocity of light

In the forward direction $\theta_p = 0$ only elastic scattering is possible. The fraction of energy transferred increases with the photon scattering angle, reaching a maximum at 180° (back scattering). At energies between 200 keV and 5 MeV Compton scattering is the predominant means of photon energy absorption in media. Further the probability of Compton interaction with an atom is proportional to the number of atomic electrons i.e. increases with increasing atomic number Z. The Compton collision cross section, giving the probability of inelastic interactions, is defined in section 9.4.

7.3 Rayleigh or elastic scattering

Rayleigh scattering is a process whereby a photon is elastically deflected from a tightly bound electron. In this process no energy loss occurs therefore Rayleigh scattering contributes only to beam attenuation and not to energy absorption which is of concern in dosimetry.

The above effects account for the principal photon interaction mechanisms at low photon energies (below 1 MeV). Other interactions are either too infrequent,e.g. Thomson scattering, or arise only at energies greater than 1 MeV, e.g. pair production etc.

7.4 Photon cross sections

When N_0 photons are incident perpendicular to an absorber of thickness x, the number transmitted N is given by the relation,

$$N = N_0 e^{-\mu x} \qquad (25)$$

where μ is the linear attenuation coefficient and is a measure of the photon beam attenuation per centimetre in the absorber material.

A more fundamental quantity than the linear attenuation coefficient is the mass attenuation coefficient defined as the linear attenuation coefficient per unit density (μ/ρ). This quantity has the advantage of being independent of the state of the absorber. The units of (μ/ρ) are usually given in cm^2/g. The mass attenuation coefficient has been defined for each photon interaction mechanism separately. However before defining them here it is important first to distinguish between absorption and attenuation. During absorption a photon actually imparts, (deposits) energy in the absorber. Attenuation is when photons are removed from the primary beam by absorption or by scattering.

The total mass attenuation coefficient (μ/ρ) for a photon beam incident on an absorber is given by the sum of the mass attenuation coefficients for the individual interaction mechanisms.

$$\frac{\mu}{\rho} = \frac{\tau}{\rho} + \frac{\sigma_c}{\rho} + \frac{\sigma_R}{\rho} \qquad (26)$$

where τ/ρ is the photoelectric mass attenuation coefficient,
σ_c/ρ is the Compton mass attenuation coefficient,

and σ_R/ρ is the mass attenuation coefficient for Rayleigh scattering.

For low Z materials the photoelectric mass attenuation coefficient (τ/ρ) and the photoelectric mass absorption coefficient (τ_a/ρ) are approximately equal. In other words each photoelectric interaction results in total absorption of the incident photon energy in the irradiated object. For photon interactions in the K-shell of high Z materials the equivalence of photoelectric attenuation and absorption coefficients can no longer be assumed since the probability of radiative transitions in the absorber atoms increases together with the photon energies involved. This means fluorescence escape from the irradiated target becomes less and less negligible. For biological matter, consisting primarily of carbon, nitrogen and oxygen, internal fluorescence transitions are of very low probability (< 0.01) and also of such low energy when they occur (< 600 eV) that in most cases they are absorbed within the sample.

The Compton process on the other hand does not result in the total photon energy being absorbed in the target material. In this case the Compton mass attenuation coefficient contains two components : the Compton mass absorption coefficient (σ_a/ρ) which relates to the actual photon energy lost to the absorber and the Compton scattering mass attenuation coefficient (σ_s/ρ) giving the energy loss due to photons being scattered out of the primary beam.

$$\frac{\sigma_c}{\rho} = \frac{\sigma_a}{\rho} + \frac{\sigma_s}{\rho} \qquad (27)$$

The Rayleigh mass attenuation coefficient (σ_R/ρ) is a small contributing factor and has been added for completeness to the total mass attenuation coefficient in equation (26). Rayleigh interactions contribute nothing to the absorption in the irradiated sample.

From the above, the expression for the total absorption coefficient (μ_a/ρ) relating the incident photon energy converted to electron kinetic energy is

$$\frac{\mu_a}{\rho} = \frac{\tau_a}{\rho} + \frac{\sigma_a}{\rho} \qquad (28)$$

So far only the cross sections for single elements have been discussed. For a biological media (or any chemical compound) comprising of several element constituents the total mass absorption coefficient is equal to the sum of the mass absorption coefficients for each individual element i multiplied by their fraction per weight w present in the medium.

$$\frac{\mu_a}{\rho} = \sum_i \frac{\mu_{a,i}}{\rho} \cdot w_i \qquad (29)$$

Formula (29) enables the mass absorption coefficient to be derived for target materials of interest in radiation biology and dosimetry.

8 Cross section calculations for biological and tissue equivalent material

8.1 Description of the programme

A computer programme has been written to calculate and plot the total mass attenuation and absorption coefficients for photons in the energy range from 100 eV - 1 MeV for biological and tissue equivalent media, on the basis of equations (26), (28) and (29). As input data each element constituent of the medium is given in percentage by weight together with its atomic number Z and atomic number A.

The photoelectric attenuation coefficient for each individual element is obtained using the following equation

$$\tau = 10^{a+b\log E} \qquad (30)$$

in which a and b are interpolation constants obtained by a least squares fit to the data of Veigele 1973. The agreement with Veigele' s data is better than 2% over the whole range of interest. A library of interpolation constants has been stored on magnetic tape in small files for those elements of particular importance in tissue equivalent materials. Each file of interpolation data is labelled by means of the atomic number corresponding to the element data it contains i.e. file 1 contains the data for hydrogen, file 6 for carbon etc. In this fashion it is possible to address the data sets directly from the input conditions. First the individual photoelectric mass absorption cross sections are interpolated at the required energies. Then using the analogous equation to (29) for (τ/ρ) the total photoelectric absorption coefficient for the material of interest is calculated.

For the Compton mass absorption, scattering and attenuation coefficients the Klein-Nishina formulae were used in the following numerical forms.

$$\sigma_a = 2\pi r_o^2 \left[\frac{2(1+\alpha)}{2(1+2\alpha)} - \frac{(1+3\alpha)}{(1+2\alpha)^2} - \frac{(1+\alpha)(2\alpha^2-2\alpha-1)}{\alpha^2(1+2\alpha)^2} - \frac{4\alpha^2}{3(1+2\alpha)^3} - \left(\frac{1+\alpha}{\alpha^3} - \frac{1}{2\alpha} + \frac{1}{2\alpha^3} \right) \ln(1+2\alpha) \right] \frac{cm^2}{electron} \qquad (31)$$

and

$$\sigma_s = \pi r_o^2 \left[\frac{\ln(1+2\alpha)}{\alpha^3} + \frac{2(1+\alpha)(2\alpha^2-2\alpha-1)}{\alpha^2(1+2\alpha)^2} + \frac{8\alpha^2}{3(1+2\alpha)^3} \right] \frac{cm^2}{electron}$$

where $\alpha = \frac{h\nu_o}{m_o c^2}$ (32)

with $h\nu_o$ = incident photon energy
$m_o c^2$ = rest energy of electron (0.511 MeV)
r_o = classical radius of the electron (2.818×10^{-13} cm)

The Compton mass attenuation coefficient is obtained from the sum of the above two expressions. The units for σ_a, σ_s and σ_{c_2} in the above equations are cm^2/electron. To convert to cm^2/g multiply through by the number of atoms per gram. Since the Compton interaction is one with atomic electrons it is also necessary to multiply by Z, the number of electrons per atom. Again with the application of equation (29) the Compton cross sections can be calculated for any desired material.

As output the programme calculates at each input energy the mass absorption and attenuation coefficients for the individual interaction mechanisms as well as the total mass absorption and attenuation coefficients with the aid of equations (26) and (28).

8.2 Selective photon absorption in the phosphorus and iodine in biological media

The photon absorption cross section is a rapidly decreasing function of photon energy up until about 100 keV after which loss by Compton absorption produces a further

slight increase in the cross sections. Figure 27 shows the photon mass absorption coefficient (μ/ρ) for phosphorus as a function of energy plotted with the cross section programme described in section 8.1. The photoelectric absorption component has been shown separately and can be seen to constitute virtually all photon interactions up to about 100 keV. Of particular importance are photon energies encompassing the electron binding energies of the irradiated medium (for phosphorus below 2.5 keV). Here due to the various absorption edges the photoelectric cross section is a sensitive function of the incident photon energy and becomes considerably more complicated when phosphorus is a constituent within a biological medium, where the absorption edges of different elements overlap. Since the Auger electron spectrum resulting from a photoelectric interaction will depend on the atom and shell in which the interaction takes place the local distribution of energy deposition may also be a sensitive function of photon energy. Experiments in which biological matter is exposed to low energy monochromatic X-rays may therefore lead to novel results e.g. Goodhead, Thacker and Cox 1981, Halpern and Stöcklin 1976.

One interesting and much debated idea is the possibility of using the photon energy range just above the K shell absorption edge, where the photoelectric cross section of certain constituent atoms in the sensitive regions of cell nuclei is high. It is of interest to secure a preferential photoelectric absorption at those sites and hence an enhanced biological effect. In this work two target elements have been under investigation : phosphorus and iodine are both particularly interesting candidates for a possible selective absorption effect with biological consequences. Phosphorus is chosen because it is the heaviest natural constituent of DNA (and therefore has the highest photoelectric cross section) being present directly in the DNA backbone structure and iodine because it can be incorporated into one of the DNA bases in the form IUdR and as a high Z element possesses a correspondingly favourable larger photoelectric cross section.

Figure 27

Photoelectric mass absorption coefficient (τ/ρ) and the total mass absorption coefficient (μ_a/ρ) for phosphorus.

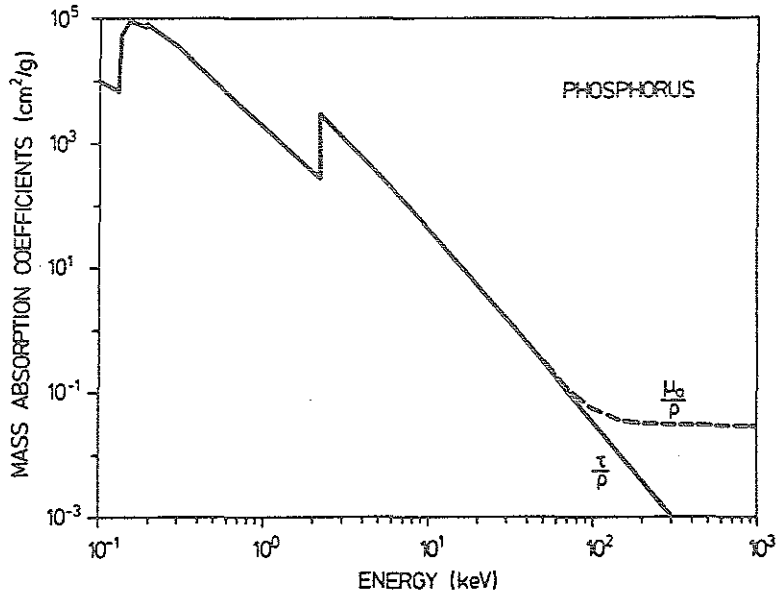

8.2.1 Phosphorus as a target in DNA

Phosphorus constitutes about 10% by weight of the DNA molecule. The percentages by weight of the other elements in DNA : hydrogen, carbon, nitrogen and oxygen are given in table 11 as obtained from the chemical formula for DNA with the assumption that all four nucleosides are present in the DNA in equal quantity.

Using the cross section programme (section 8.1) with the constituent input data of table 11 the photoelectric absorption cross section was calculated for a DNA molecule for photon energies from 100 eV - 100 keV. The calculated values for photoelectric mass absorption coefficients are given in table 12 and represented graphically in figure 28. The photoelectric K absorption edges of carbon, nitrogen, oxygen and phosphorus are well visible at energies 283 eV, 401 eV, 531 eV and 2.145 keV respectively. Of particular interest here is the sharp reduction in the phosphorus K edge against a medium of pure phosphorus (figure 27). A measure of magnitude of an absorption edge is given by the so called " jump ratio " which is the ratio of the absorption coefficients at the upper edge to that at the lower. The jump ratio for pure phosphorus is 10.78 and falls to 1.81 for phosphorus when a constituent of the DNA.

The DNA molecule however represents only a small component of a cell nucleus. Further calculations were therefore performed in which the compositional ingredients of a cell nucleus were studied. Using data on the relative DNA, RNA, protein and histone contents (dry weight) of HeLa cell nuclei [24] from Altman and Katz Eds. 1976, it was possible to estimate the relative weight percentage of each individual nuclear element constituent (table 11).

[24] The relative individual element weight percentages were also examined for other mammalian cell nuclei. Variations in the nuclear constitution were found to be quite small.

Figure 28
Photoelectric mass absorption coefficient (τ/ρ) for DNA as a function of the incident photon energy.

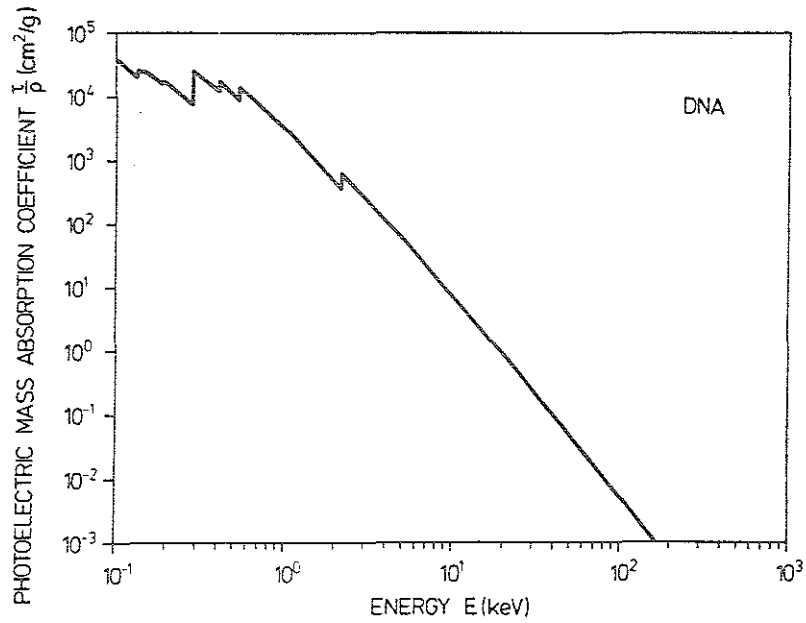

Figure 29
Photoelectric mass absorption coefficient (τ/ρ) for a cell nucleus, (constituents given in table 11) as a function of the incident photon energy.

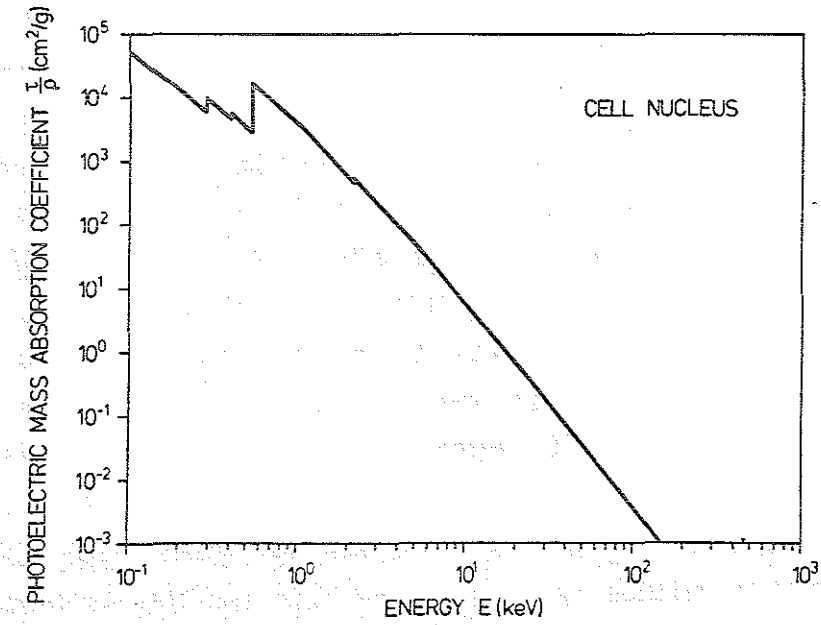

Table 11

Percentage by weight of the atomic constituents in biological matter

Atom	DNA	Cell nucleus [25]
H	3.86	10.64
C	40.10	9.02
N	17.99	3.22
O	27.42	74.11
P	10.63	2.64 [26]
S	-	0.37

[25] The relative weights of the constituent elements of the cell nucleus were calculated using the following DNA, RNA, protein and histone relative weight fractions: RNA/DNA = 0.29, protein/DNA = 6.90 and histone/DNA = 3.6 (for HeLa cell nuclei from Altman and Katz Eds. 1976). This gives the following percentage dry weights DNA = 8.5%, RNA = 2.5%, protein = 58.4% and histone = 30.6%. These values were renormalized to include a percentage by weight of 80% water.

[26] The value for phosphorus was obtained from an experimental work by Mehard and Volcani 1976 for rat liver cell nuclei, in which they found from studies using X-ray microanalysis 165.4 µg phosphorus/mg protein.

From this nuclear constitution the photoelectric cross sections were calculated (table 12, figure 29). The result shows a further decrease in the magnitude of the phosphorus K-edge, (the jump ratio reduces to 1.15) due to the even lower phosphorus content 2.4% in the cell nucleus. It must also be emphasized that only about one tenth of this 2.4% phosphorus stems actually from the DNA, the rest is present as non-DNA bound phosphorus in the nucleus. Thus these results tend to indicate that a selective absorption effect at the K-edge of phosphorus in the cell nucleus is, from a consideration of cross section data, unlikely to produce an enhanced bilogical effect. Nevertheless, monochromatic photons of energy just above the K-edge of phosphorus might still induce per photon interaction in a phosphorus atom, a different local energy deposition

Table 12

Photoelectric mass absorption coefficients for phosphorus, DNA and the cell nucleus

Energy(keV) Photoelectric mass absorption coefficient(cm^2/g)

	Phosphorus	DNA	Cell nucleus
1.000E-1	1.010E 4	3.729E 4	5.174E 4
1.220E-1	7.455E 3	2.395E 4	3.308E 4
1.230E-1	7.363E 3	2.352E 4	3.248E 4
1.310E-1	6.687E 3	2.041E 4	2.819E 4
1.330E-1	5.393E 4	2.476E 4	2.850E 4
1.500E-1	8.867E 4	2.390E 4	2.300E 4
1.850E-1	7.434E 4	1.689E 4	1.515E 4
1.880E-1	7.329E 4	1.646E 4	1.466E 4
1.900E-1	7.953E 4	1.692E 4	1.453E 4
2.831E-1	3.868E 4	7.421E 3	5.839E 3
2.845E-1	3.833E 4	2.564E 4	9.886E 3
3.000E-1	3.475E 4	2.288E 4	8.773E 3
4.009E-1	1.828E 4	1.238E 4	4.585E 3
4.023E-1	1.812E 4	1.743E 4	5.468E 3
5.313E-1	8.980E 3	8.728E 3	2.734E 3
5.327E-1	8.921E-3	1.388E 4	1.679E 4
6.234E-1	5.999E 3	9.473E 3	1.158E 4
6.250E-1	5.960E 3	9.414E 3	1.151E 4
7.000E-1	4.478E 3	7.151E 3	8.808E 3
8.920E-1	2.429E 3	3.906E 3	4.958E 3
8.940E-1	2.415E 3	3.884E 3	4.932E 3
1.070E 0	1.535E 3	2.573E 3	3.330E 3
1.073E 0	1.524E 3	2.552E 3	3.304E 3
1.500E 0	6.544E 2	9.620E 2	1.261E 3
2.000E 0	3.166E 2	4.169E 2	5.513E 2
2.145E 0	2.654E 2	3.403E 2	4.508E 2
2.147E 0	2.861E 3	6.154E 2	5.181E 2
2.470E 0	1.956E 3	4.142E 2	3.473E 2
2.475E 0	1.946E 3	4.118E 2	3.534E 2
3.000E 0	1.154E 3	2.393E 2	2.042E 2
4.556E 0	3.715E 2	7.362E 1	6.200E 1
4.558E 0	3.711E 2	7.353E 1	6.193E 1
4.850E 0	3.136E 2	6.167E 1	5.187E 1
4.853E 0	3.130E 2	6.156E 1	5.178E 1
5.187E 0	2.585E 2	5.037E 1	4.188E 1
5.189E 0	2.583E 2	5.031E 1	4.183E 1
7.000E 0	1.089E 2	2.059E 1	1.665E 1
1.000E 1	3.889E 1	7.066E 0	5.551E 0
1.500E 1	1.145E 1	2.031E 0	1.575E 0
2.000E 1	4.768E 0	8.318E-1	6.418E-1
3.316E 1	1.023E 0	1.708E-1	1.260E-1
3.318E 1	1.021E 0	1.705E-1	1.257E-1
5.000E 1	2.809E-1	4.615E-2	3.353E-2
7.000E 1	9.744E-2	1.573E-2	1.123E-2
1.000E 2	3.172E-2	5.035E-3	3.530E-3
1.500E 2	8.854E-3	1.380E-3	9.475E-4
2.000E 2	3.581E-3	5.521E-4	3.749E-4
3.000E 2	9.996E-4	1.518E-4	1.015E-4
5.000E 2	2.003E-4	2.986E-5	1.959E-5
7.000E 2	6.941E-5	1.028E-5	6.632E-6
1.000E 3	2.261E-5	3.293E-5	2.104E-6

around the target atom (with possible biological consequences) than photons of energy just below the edge. For a detailed analysis of this problem see Booz, Humm et al 1983.

8.2.2 Iodine in the DNA

In a further calculation the possibility of selective absorption in iodine incorporated in the form of IUdR in the DNA was studied. At the outset the most beneficial situation possible for selective absorption was assumed i.e. that 100% replacement of the thymidine in DNA by IUdR is attainable [27]. This would mean 9.3% by weight of iodine in the DNA and about 0.29% in the cell nucleus.

With such an incorporation the magnitude of the iodine K shell jump ratio would be 1.60 i.e. higher than that obtainable for phosphorus. However this K edge reduces in proportion to the percentage of iodine present in the DNA. If replacement of only one in ten thymidine takes place (10% incorporation) then the iodine K edge jump ratio is correspondingly smaller.

Calculated results for the total mass absorption coefficients for DNA and the cell nucleus, with 100% IUdR replacement of thymidine, are tabulated in table 13. Figures 30 and 31 give the values of table 13 in a graphical representation. The results of this study show that the possibility of a selective photoelectric absorption in the sensitive targets of biological material are in general limited by the small fractional weight of the selective target atom in the irradiated medium. The advantage of the high jump ratio of a pure element is lost when only a small fraction of the photon interactions in the medium actually take place in the target atom.

[27] This work was purely concerned with the photon absorption cross sections for the extreme case where selective absorption would be a maximum. The detrimental effects of such a high incorporation are recognised but of no concern here.

Table 13

Total mass absorption coefficient for 100% replacement of thymidine by IUdR in DNA and the DNA of a cell nucleus as a function of the incident photon energy.

Energy(keV)	DNA with IUdR	Cell nucleus with IUdR
1.000E-1	3.614E 4	5.125E 4
1.220E-1	2.288E 4	3.277E 4
1.230E-1	2.245E 4	3.217E 4
1.310E-1	1.963E 4	2.793E 4
1.330E-1	2.332E 4	2.834E 4
1.500E-1	2.223E 4	2.298E 4
1.850E-1	1.579E 4	1.517E 4
1.880E-1	1.560E 4	1.469E 4
1.900E-1	1.598E 4	1.458E 4
2.831E-1	7.198E 3	5.881E 3
2.845E-1	2.286E 4	1.029E 4
3.000E-1	2.044E 4	9.134E 3
4.009E-1	1.119E 4	4.790E 3
4.023E-1	1.554E 4	5.781E 3
5.313E-1	7.917E 3	2.900E 3
5.327E-1	1.324E 4	1.668E 4
6.234E-1	9.118E 3	1.150E 4
6.250E-1	9.058E 3	1.143E 4
7.000E-1	8.110E 3	8.786E 3
8.920E-1	4.483E 3	4.943E 3
8.940E-1	4.700E 3	4.925E 3
1.070E 0	3.355E 3	3.331E 3
1.073E 0	3.375E 3	3.306E 3
1.500E 0	1.323E 3	1.263E 3
2.000E 0	5.941E 2	5.526E 3
2.145E 0	4.892E 2	4.520E 2
2.147E 0	7.249E 2	5.245E 2
2.470E 0	4.924E 2	3.518E 2
2.475E 0	4.897E 2	3.577E 2
3.000E 0	2.882E 2	2.068E 2
4.556E 0	9.141E 1	6.292E 1
4.558E 0	1.429E 2	6.444E 1
4.850E 0	1.203E 2	5.400E 1
4.853E 0	1.458E 2	5.470E 1
5.187E 0	1.207E 2	4.433E 1
5.189E 0	1.356E 2	4.474E 1
7.000E 0	5.846E 1	1.794E 1
1.000E 1	2.146E 1	6.049E 0
1.500E 1	6.825E 0	1.744E 0
2.000E 1	3.042E 0	7.235E-1
3.316E 1	7.404E-1	1.559E-1
3.318E 1	3.785E 0	2.501E-1
5.000E 1	1.190E 0	8.402E-2
7.000E 1	4.693E-1	4.352E-2
1.000E 2	1.850E-1	3.106E-2
1.500E 2	7.527E-2	2.919E-2
2.000E 2	4.914E-2	3.021E-2
3.000E 2	3.610E-2	3.191E-2
5.000E 2	3.182E-2	3.280E-2
7.000E 2	3.039E-2	3.229E-2
1.000E 3	2.863E-2	3.082E-2

Figure 30
Total mass absorption coefficient (μ_a/ρ) for DNA, with 100% replacement of thymidine with IUdR, as a function of the incident photon energy.

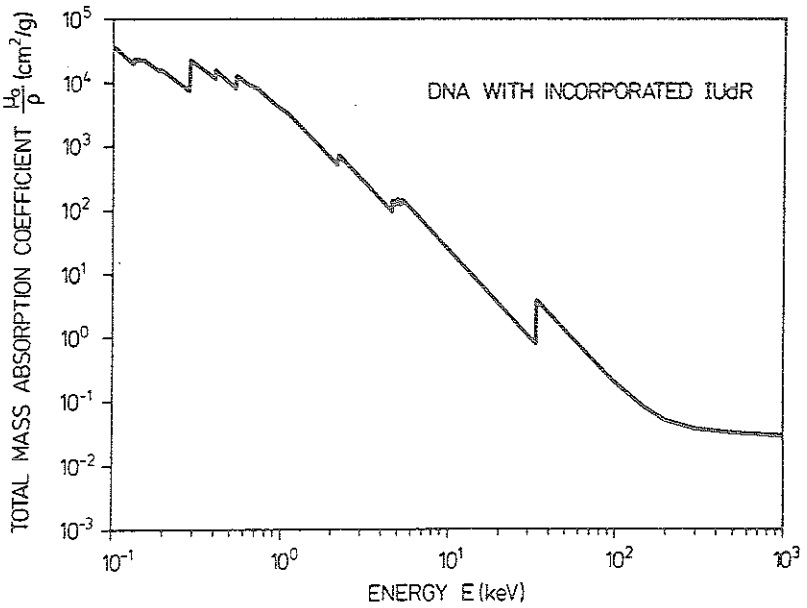

Figure 31
Total mass absorption coefficient (μ_a/ρ) for the cell nucleus, with 100% replacement of thymidine in the nuclear DNA with IUdR, as a function of the incident photon energy.

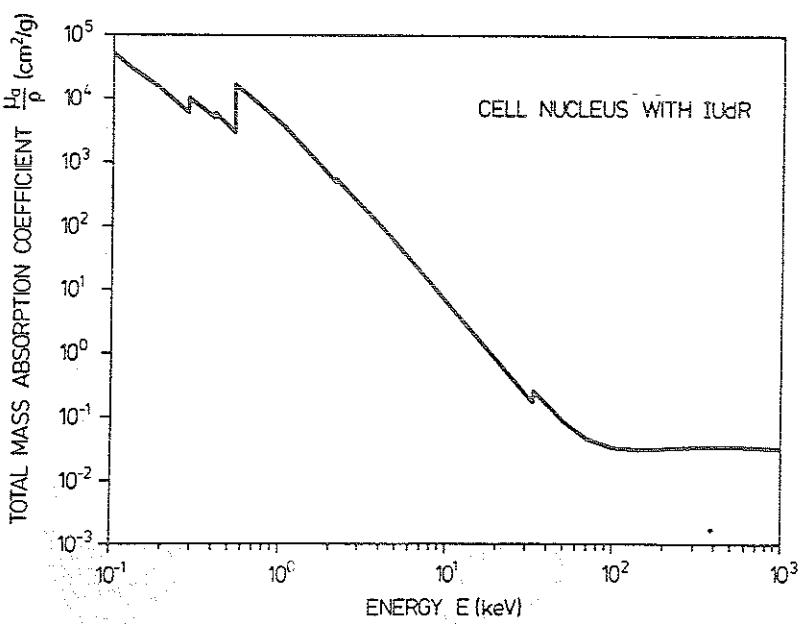

Nevertheless certain factors other than the cross section data also require consideration. Namely, the energy deposition per interaction in the selective target atom, since it may be that a photoelectric interaction in a phosphorus or iodine atom alone is sufficient to inflict considerable local damage. For iodine this question has already been largely dealt with in Part I of this thesis since the results for electron capture induced vacancy cascades in ^{123}I and ^{125}I resemble closely the situation of a monochromatic photon irradiation with photons of energy just above the iodine K edge. The next section therefore treats in detail photoelectric interactions in phosphorus and examines the Auger electron spectra and their respective energy deposition for computer simulated irradiations with monochromatic photons of different energies.

Before this, however, the attention remains in the next section with photon cross sections but for tissue equivalent media.

8.3 Photoelectric absorption cross sections for tissue equivalent media

In experimental microdosimetry special proportional counters have been developed which simulate biological tissue in order to make energy deposition measurements relevant to studies in radiation biology and related subjects. These counters, usually referred to as " Rossi counters " in honour of their innovator, comprise of walls made from tissue equivalent plastic and operate with a tissue equivalent gas as a counting gas. Obviously there are practical limitations to the exactness of the simulation i.e. for operation of the counter the wall must be of conducting material, the tissue equivalent gas mixture must have the desirable properties of a counting gas etc.

In this section the tissue equivalence of tissue equivalent media at low photon energies is investigated. Once again using the photon cross section programme of section 8.1 the photoelectric mass absorption coefficients for the commonly used A-150 tissue equivalent plastic and

Rossi-Failla tissue equivalent gas were calculated as well as for ICRU tissue equivalent muscle. The results are given for all three tissue equivalents [28] in table 14 where they can be compared to the photoelectric cross section data for the cell nucleus from table 12.

The greatest differences both between the various tissue equivalent materials themselves and between the tissue equivalents and cell nucleus data occurs at photon energies below 1 keV, reflecting the variation in the relative weights of carbon, nitrogen and oxygen in the material constitutions, (A-150 tissue equivalent plastic is carbon based, Rossi-Failla gas has about equal amounts of carbon and oxygen whereas ICRU muscle equivalent and the cell nucleus have oxygen as the predominent constitu nt). Above 1 keV the differences in the photoelectric cross section are in general between 10% - 100% higher for the cell nucleus than for A-150 plastic or Rossi-Failla gas. For the ICRU muscle equivalent however an excellent agreement is obtained with the cell nucleus data over the entire photon energy range. Figure 32 demonstrates this in a plot of the ratio of the photoelectric mass absorption coefficients for the cell nucleus to ICRU muscle equivalent as a function of energy. Once again the cell nucleus data is with the exception of the photon energy range between the carbon and oxygen K edges, greater than for the ICRU muscle equivalent with deviations of up to about 16% at 100 keV.

These results show that in the photon energy range below 100 keV tissue equivalent materials may not be accurate in simulating cell nuclei, the most sensitive target areas in tissue. The accuracy of simulation of a cell nucleus or for that matter real tissue is sensitively dependent on the precise atomic constituents of the medium. Exact simulation is only then achieved when the relative weights of all atomic constituents agree between simulant and what is to be simulated.

[28] The relative weights of the atomic components of several of the most commonly used tissue equivalent materials are in the ICRU Report on Microdosimetry 1983.

Figure 32
Ratio of the photoelectric mass absorption coefficients, cell nucleus/ICRU tissue equivalent, as a function of the incident photon energy.

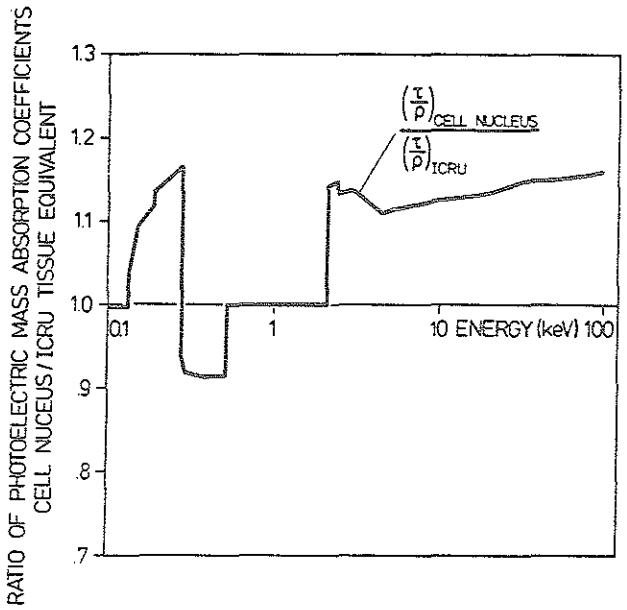

Table 14

Photoelectric absorption coefficients for A-150 tissue equivalent plastic, Rossi-Failla tissue equivalent gas and the ICRU tissue equivalent muscle as a function of photon energy.

	τ/ρ (cm^2/g)			τ/ρ / τ/ρ
Energy(keV)	A-150 plastic	Rossi-Failla gas	ICRU-muscle equivalent	cell nucleus / ICRU equiv.
.100	3.001E 4	4.039E 4	5.191E 4	1.00
.122	1.912E 4	2.572E 4	3.318E 4	1.00
.123	1.877E 4	2.525E 4	3.258E 4	1.00
.131	1.628E 4	2.189E 4	2.828E 4	1.00
.133	1.573E 4	2.116E 4	2.743E 4	1.04
.150	1.199E 4	1.611E 4	2.103E 4	1.09
.185	7.487E 3	1.003E 4	1.357E 4	1.12
.188	7.221E 3	9.674E 3	1.310E 4	1.12
.190	7.052E 3	9.446E 3	1.281E 4	1.13
.283	2.874E 3	3.672E 3	5.009E 3	1.17
.285	3.827E 4	2.443E 4	1.056E 4	.94
.300	3.409E 4	2.173E 4	9.544E 3	.92
.401	1.914E 4	1.182E 4	5.024E 3	.91
.402	1.998E 4	1.272E 4	5.984E 3	.91
.531	9.866E 3	6.245E 3	2.980E 3	.91
.533	1.079E 4	1.393E 4	1.681E 4	1.00
.623	7.229E 3	9.502E 3	1.159E 4	1.00
.625	7.182E 3	9.443E 3	1.152E 4	1.00
.700	5.578E 3	7.168E 3	8.813E 3	1.00
.892	3.011E 3	3.965E 3	4.957E 3	1.00
.894	2.993E 3	3.943E 3	4.931E 3	1.00
1.070	1.966E 3	2.635E 3	3.329E 3	1.00
1.073	1.950E 3	2.613E 3	3.308E 3	1.00
1.500	7.167E 2	9.792E 2	1.260E 3	1.00
2.000	3.040E 2	4.217E 2	5.501E 2	1.00
2.145	2.459E 2	3.436E 2	4.497E 2	1.00
2.147	2.452E 2	3.427E 2	4.536E 2	1.14
2.470	1.613E 2	2.274E 2	3.030E 2	1.15
2.475	1.603E 2	2.261E 2	3.123E 2	1.13
3.000	9.020E 1	1.288E 2	1.796E 2	1.14
4.556	3.944E 1	3.795E 1	5.589E 1	1.11
4.558	3.938E 1	3.790E 1	5.582E 1	1.11
4.850	3.276E 1	3.160E 1	4.669E 1	1.11
4.853	3.270E 1	3.154E 1	4.661E 1	1.11
5.187	2.676E 1	2.548E 1	3.763E 1	1.11
5.189	2.673E 1	2.545E 1	3.758E 1	1.11
7.000	1.092E 1	1.004E 1	1.484E 1	1.12
10.000	3.671E 0	3.263E 0	4.932E 0	1.13
15.000	1.061E 0	9.059E-1	1.395E 0	1.13
20.000	4.395E-1	3.643E-1	5.664E-1	1.13
33.160	9.144E-2	6.953E-2	1.098E-1	1.15
33.180	9.127E-2	6.940E-2	1.096E-1	1.15
50.000	2.486E-2	1.824E-2	2.917E-2	1.15
70.000	8.542E-3	6.030E-3	9.747E-3	1.15
100.000	2.758E-3	1.869E-3	3.047E-3	1.16

9 Simulation of photoelectric interactions in phosphorus using Monte-Carlo methods

9.1 The photoelectric effect in phosphorus

This section is concerned with the microdosimetry of low energy photon interactions in phosphorus when irradiated with monochromatic photons just above and below the K edge. Photons of energy below 5 keV interact with phosphorus almost totally by the photoelectric effect and then predominantly with the innermost shell for which the photon energy $h\nu$ exceeds the orbital binding energy E_B. Such an interaction produces a photoelectron of energy T as given by equation 22 (Part II section 7.1) and leaves an excitation energy on the atom equal to the binding energy of the atomic vacancy. This energy is usually rapidly lost by a cascade process of inner shell atomic transitions of predominantly non-radiative nature in a manner analogous to that following electron capture or internal conversion as already discussed in Part I of this thesis. Such cascade processes can be simulated using a Monte-Carlo approach in order to obtain information on the statistical distribution of the electron emission spectra from which an estimate of the local energy deposition in volumes around the photoelectric interaction sites can be made.

9.2 Method

An inner shell electron vacancy which is produced by the photoelectric effect gives rise to a chain of events which are independent as to the nature by which the initial inner shell vacancy was produced. For this reason much of the Monte-Carlo computer code already developed to simulate radionuclide decay by electron capture or internal conversion could be directly employed for the purposes of calculations proposed here. That what is different is the simulation of the photoelectric interaction itself. Since a photoelectric interaction can in principle take place in any shell for which $h\nu > E_B$, the first step in the Monte-

Carlo simulation process is to choose a shell for interaction where the sub-shell interaction probabilities are correspondingly weighted according to their respective cross sections (see section 9.3.1). The sub-shell containing the induced vacancy is recorded and the energy of the photoelectron calculated from equation 22 (Part II, section 7.1). The programme then addresses the set of transition probabilities to the shell with the vacancy, selects a transition with the random number generator, records the new vacancy/vacancies and so on until all vacancies have reached the outer M shells.

The problem of neutralizing the charge build-up on the phosphorus atom during the vacancy cascade is treated with in the same way as described for vacancy cascades induced by radionuclide decay (Part I , section 4.2.1). Figure 33 depicts a typical vacancy cascade resulting from a photoelectric interaction in the K shell of a bound phosphorus atom, in a condensed medium, with the possibility of autoionization [29] i.e. an electron which falls from the conduction band of the medium to fill a vacancy in one of the phosphorus levels leads to the release of a further electron. In these calculations the free electrons in the conduction band were attributed with an energy of zero electron volts as a first approximation.

The computer code has been used to generate emission spectra (electron and photon) for 10,000 simulated photoelectric interactions at five incident photon energies : 4.55 keV (titanium K_α), 2.145 keV (just above the phosphorus K edge), 2.128 keV (just below the phosphorus K edge), 1.5 keV (aluminium K_α) and 278 eV (carbon K_α). The electron spectra for each photon energy were stored on magnetic tape and used for energy deposition calculations in spheres of variable diameter containing a homogeneous distribution of phosphorus atoms.

[29] The term autoionization generally refers to electrons which when falling from a superexcited state are able to set free a bound electron (see T.A.Carlson, Photoelectron and Auger Spectroscopy Plenum Press, New York, pg 4, 1975).

Figure 33
Electron cascade process induced by a photoelectric interaction in the K shell of phosphorus.

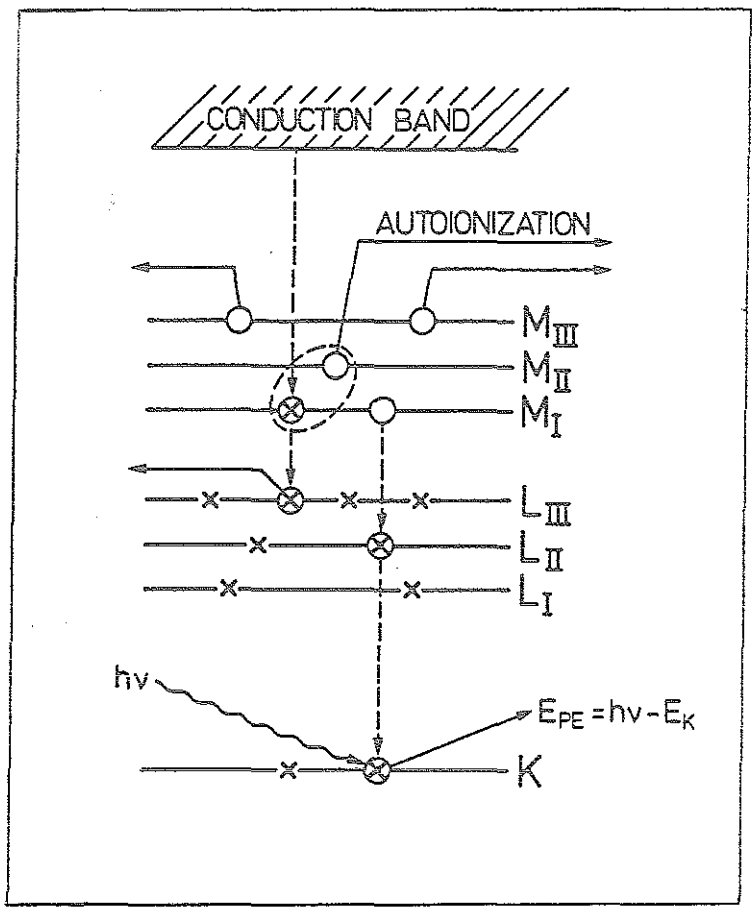

9.3 Input data for phosphorus calculations

The programme simulating photoelectric interactions in phosphorus requires three sets of input data.

1. The initial inner shell vacancy distribution
2. The electron transition probabilities
3. The electron and photon energies

9.3.1 The initial inner shell vacancy distribution

The distribution of initial inner shell vacancies in a phosphorus atom produced by photoelectric interactions after irradiation with monochromatic X-rays is directly proportional to the sub-shell photoelectric cross sections at the incident photon energy. In dividing the individual sub-shell photoelectric cross sections at a photon energy $h\nu$ by the total atomic photoelectric cross section one obtains the relative sub-shell interaction probabilities at that photon energy. In table 15 are given the relative sub-shell interaction probabilities used for the phosphorus calculations in this work derived from the photoelectric sub-shell cross section data of Scofield, 1973, for photon energies above 1 keV and from Band et al, 1979, for energies below 1 keV.

Table 15
Relative sub-shell photoelectric interaction probabilities at photon energies : 4.55 keV, 2.145 keV, 2.128 keV, 1.5 keV and 278 eV

Energy (keV)	Sub-shell						
	K	L_1	L_2	L_3	M_1	M_2	M_3
4.55	0.913	0.056	0.007	0.013	0.006	0.002	0.004
2.145	0.900	0.055	0.013	0.026	0.005	0.000	0.001
2.128	-	0.547	0.132	0.257	0.052	0.004	0.008
1.5	-	0.470	0.159	0.312	0.044	0.005	0.010
0.278	-	0.143	0.267	0.531	0.018	0.013	0.028

At photon energies above the K edge of phosphorus over 90% of the photoelectric interactions occur in the phosphorus K shell. Once slightly below the phosphorus K edge (2.128 keV) photoelectric interactions in the K shell are no longer permissible and interactions occur predominantly in the L shell. Since the L shell consists of three sub-shells the initial vacancies are in general distributed among all three. At the photon energy 2.128 keV the largest number of photon interactions take place in the L_1 shell. With decreasing photon energies i.e. 1.5 keV and 278 eV, the probability of a photoelectric interactions in L_1 is reduced complimented by a corresponding increase in the interaction probability in L_2 and L_3. This change in the relative probability for interaction in the various L sub-shells shows an influence on the electron emission spectra (see section 9.4.1).

9.3.2 The electron transition probabilities

Inner shell electron transitions in elements of low atomic number such as phosphorus are predominantly non-radiative Auger and Coster-Kronig transitions. In this work the non-radiative transition data were taken from Mc Guire (for transitions to the K shell Mc Guire, private communication, and to the L shells Mc Guire, 1972).

The probability of radiative transitions is given by the fluorescence yield ω which for the phosphorus K shell is 0.06, Krause 1979, and for the higher shells negligible i.e. a photoelectric interaction in the phosphorus L shell produces only an electron spectrum. The K shell radiative transition probabilities were taken from Salem et al 1974. In accordance with the fluorescence yield of the K shell ($\omega_K = 0.06$) all radiative transitions to the K shell are normalized to 0.06 and non-radiative transitions to 0.94. The L shell transition probabilities are divided into those to L_1, L_2 and L_3. Since $\omega_L \simeq 0$ each set of sub-shell non-radiative transition probabilities is normalized to one. A list of the normalized radiative and non-radiative transitions to the K and L shells used in the work are given in

table 6a, appendix 6.

The phosphorus atom also has electrons in the M shell : two in M_1, one in M_2 and a further two in M_3. The possibility of super Coster-Kronig transitions in the M shell were however not considered in these calculations, principally because no data was found available in the literature for these transmitions in phosphorus. However the lack of such data implies that their probability is small [30]. Also the energy differences involved are of the of the order of only a few electron volts, therefore the error introduced by their neglect is likely to be quite small.

9.3.3 Electron and photon energies

The energies of the electrons and photons resulting from inner shell transitions used in these calculations are given in column 5 of table 6a, appendix 6. The photon energies were taken from Storm and Israel 1970, Auger and Coster-Kronig electron energies calculated using equation 12, the so called modified Z+1 approximation (Part I, section 3.2.3), and the photoelectron energies calculated within the programme (depends on the photon energy) with equation 22 (Part II, section 7.1).

9.4 Results

9.4.1 Electron number distributions and their dependence on chemical phase and photon energy

A single photoelectric interaction by a photon of energy above the K edge of an isolated phosphorus atom can lead to the emission of between one and five electrons. Therefore in simulating 10,000 photoelectric interactions in phosphorus one obtains a distribution of the electron

[30] Most vacancy cascades in phosphorus have the M shell highly depleted since on average about four electrons per K shell vacancy are emitted (see section 9.4).

emission number, the shape of which depends on the incident photon energy. Also the chemical phase can influence the shape of the distribution. In figure 34 the electron number distributions are shown for calculations of phosphorus irradiated just above the K edge i.e. with 2.145 keV X-rays, as an isolated atom and in a condensed medium. The influence of possible neutralization of charge build-up on an element of low atomic number such as phosphorus is small when compared to the similar study made for iodine (Part I section 4.2.2). The higher electron number end of the distribution becomes marginally increased as well as the average electron number per interaction as a result of the additional autoionization electrons released.

The effect of the incident photon energy on the electron number distribution is shown in figure 35. At photon energies above the phosphorus K edge, where more than 90% of the initial vacancies are produced in the K shell, the change in the electron number distribution is small. However at photon energies below the edge the spread of the distribution is reduced to between one and three electrons and the shape of the distribution becomes more sensitive to photon energy due to a shifting in the sub-shell photoelectric interaction probabilities. The mean number of electrons emitted per photoelectric interaction $\bar{n}$ together with further data e.g. the average electron energy per interaction $\bar{E}$, are given in table 16 for the different incident photon energies.

Table 16

Average electron number $\bar{n}$, electron energy $\bar{E}$, photon energy $\bar{P}$ and potential energy $\overline{IP}$ following photoelectric interactions in phosphorus at different incident photon energies $h\nu$

$h\nu$ (keV)	Condensed phase $\bar{n}$	$\bar{n}$	Isolated atom $\bar{E}$	$\bar{P}$	$\overline{IP}$
4.55	4.03	3.98	4.335	0.101	0.114
2.145	3.99	3.94	1.934	0.100	0.111
2.128	2.47	2.47	2.084	-	0.044
1.5	2.40	2.40	1.458	-	0.042
0.278	2.08	2.07	0.245	-	0.033

Figure 34
Electron number distribution for 4.55 keV photons incident on phosphorus as an isolated atom and in the condensed phase.

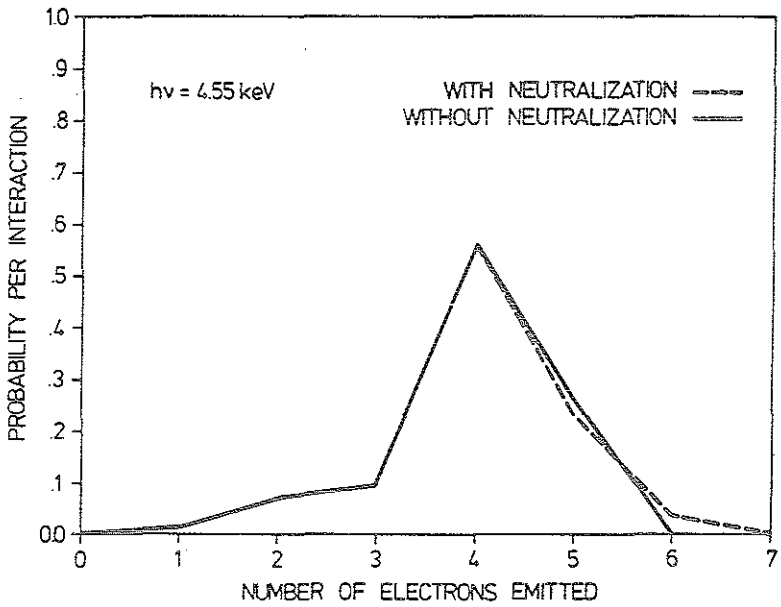

Figure 35
Electron number distribution for photoelectric interactions in phosphorus, (condensed phase) showing the effect of incident photon energy.

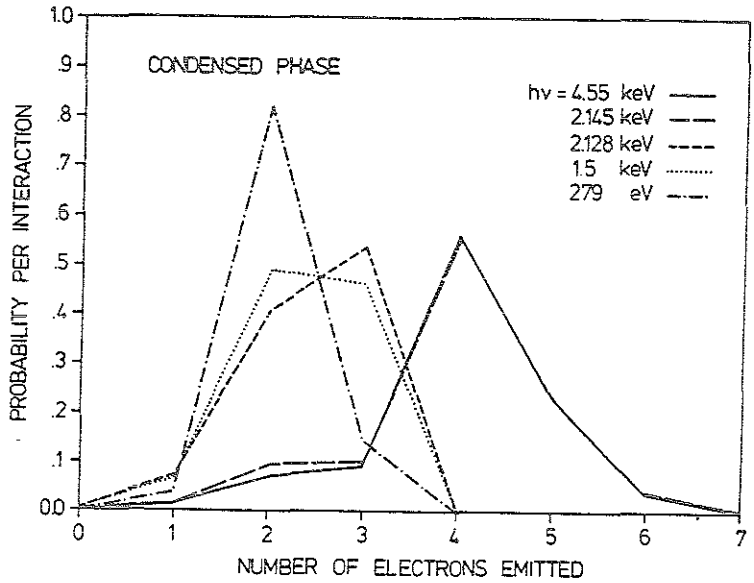

9.4.2 Energy balance and particle fractions

For a photoelectric interaction in an isolated phosphorus atom the energy of all particles released from the phosphorus plus that remaining on the phosphorus atom must be equal to the incident photon energy $h\nu$, from the principle of conservation of energy. Thus the energy balance equation for a photoelectric interaction can be written.

$$h\nu = \sum_{i=1,m} E_i + \sum_{j=1,n} P_j + I_m \qquad (33)$$

where $\sum_{i=1,m} E_i$ is the sum of the energies of m emitted electrons including the photoelectron,

$\sum_{j=1,n} P_j$ is the sum of the energies of n emitted photons,

and I_m is the total potential energy for an atom with charge +m equal to the sum of the first m ionization potentials [31].

The incident photon energy is converted to electron, photon and potential energy of the phosphorus atom. The relative fraction of energy converted to each is shown graphically in figure 36 for selected photon energies between 278 eV and 4.55 keV, together with the variation in the average number of electrons emitted (insert).

At photon energies below the phosphorus K edge the total energy fraction is composed of two components, the largest fraction is due to the incident photon energy being converted to electron energy (0.8 - 1.0) and a smaller quantity remaining as potential energy on the phosphorus atom (0.0 - 0.2). At the phosphorus edge there is a slight drop in the electron energy fraction. This is due firstly to the appearance of a fluorescence component (6% of the transitions to an initial vacancy in the K shell are radiative) and secondly from the possibility of a larger

[31] The ionization potential data from Handbook of Physics and Chemistry R.C.Weast Ed. 1980-81 were used.

Figure 104
Energy fractions and average electron emission number, (insert) for photoelectric interactions on phosphorus at different incident photon energies in the range 279 eV - 4.55 keV.
Isolated atom - - - -
Condensed phase ————

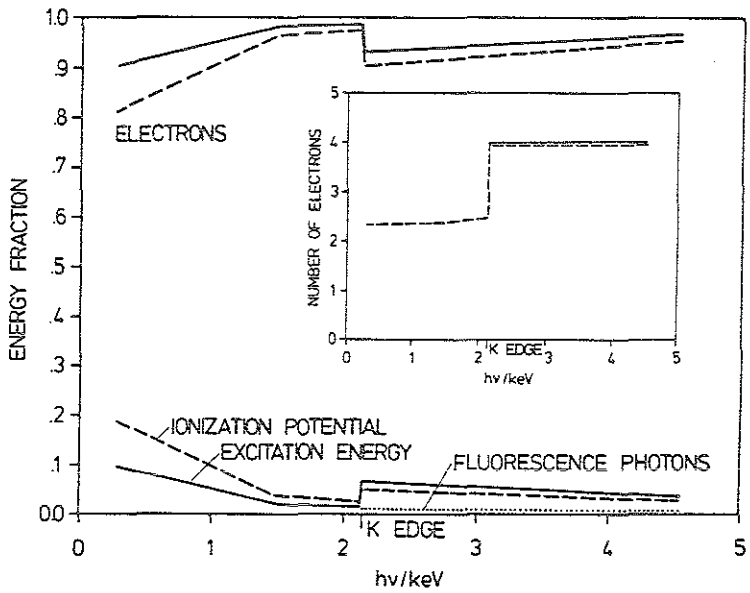

number of Auger electrons being emitted (see insert figure 36) which increases the average charge on the phosphorus atom and hence the atomic potential energy. With increasing photon energies above the K absorption edge the electron energy fraction increases asymptotically to one, as the photoelectron takes a continually higher fraction of the incident photon energy.

Figure 36 also shows the relative energy fractions for phosphorus when in the condensed phase. In this case the potential energy on the phosphorus atom will attract electrons from neighbouring atoms eventually resulting in the neutralization of the phosphorus. Therefore the potential energy becomes converted partly to further electron energy by autoionization and the rest to various collective sources of excitation energy e.g. phonons, plasmons etc. dissipated in the medium.

9.4.3 Emission spectra

From 10,000 individual electron energy spectra at each photon energy an average electron energy spectrum could be formed. Figures 37 and 38 show two examples for the photon energies : 4.55 keV above the K edge, and 1.5 keV below the K edge, of phosphorus. Such spectra are not necessarily typical for the electron emission from a single interaction, which can have a large statistical variation, but do give the probability per interaction with which an electron with a particular energy is emitted from a large number of interactions.

The different components of the emission spectra are distinguishable for a low Z element such as phosphorus, therefore the individual groups of spectral lines in the diagrams have been labelled. For the irradiation with 4.55 keV photons the addition of the phosphorus K fluorescence photon lines makes the emission spectrum complete.

Figure 37
Average individual electron energy spectrum produced by 4.55 keV X-rays incident on phosphorus.

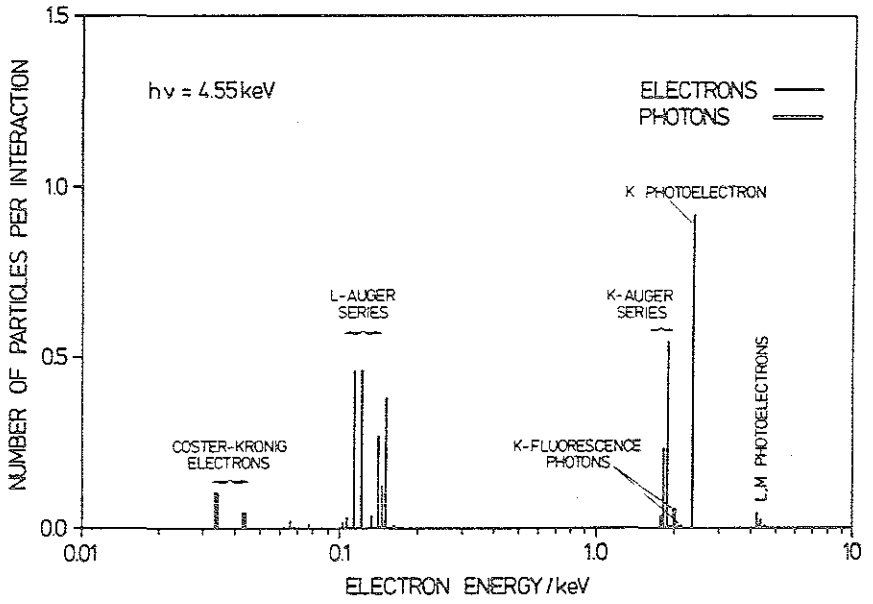

Figure 38
Average individual electron energy spectrum produced by 1.5 keV X-rays incident on phosphorus.

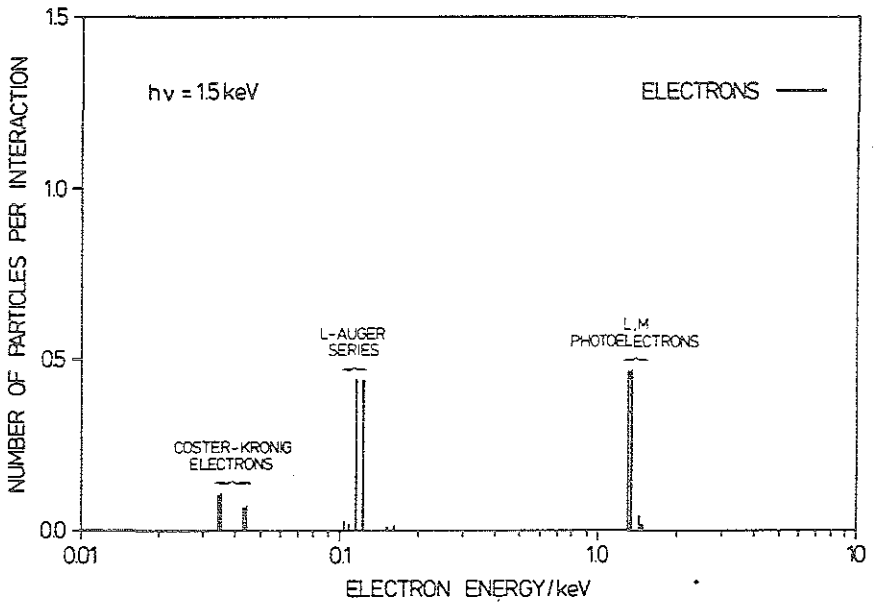

9.4.4 Energy deposition as a function of incident photon energy

The energy of a photon which interacts by the photoelectric effect in an atom such as phosphorus becomes mainly converted to a series of low energy short range electrons. This makes the site of a photoelectric interaction, one around which a high concentration of energy deposition can occur.

For a homogenous distribution of phosphorus atoms in a spherical volume V the energy deposition in V was calculated per interaction at different incident photon energies [32]. Using the point kernel data of M.J.Berger and the individual electron spectra data for 10,000 simulated photoelectric interactions per photon energy the average energy deposition $\bar{E}$ per interaction could be calculated as a function of the volume diameter d, (the method of the calculation follows in an analogous way as for incorporated radionuclides, see Part I, section 6). Further the assumption has been made that the potential energy, from the charge build-up on the phosphorus, is locally deposited and that the energy emitted in form of photons is carried far from the interaction site making no contribution to the local energy deposition. The values obtained for $\bar{\epsilon}_F$ from these calculations are presented in table 17 and figure 39 for photon energies from 278 eV - 4.55 keV in site diameters from 1 nm - 10 µm.

At site diameters greater than about 5 µm the mean energy deposition approaches that of the incident photon energy [33] i.e. almost all the available electron energy becomes absorbed within the diameter of a cell nucleus. Decreasing the site size reduces the mean energy deposition as more and more electron energy escapes outside the

[32] A homogenous distribution of phosphorus might be a good approximation due to the superwinding of the DNA in the cell nucleus, although the localization of the DNA is different at different times in the cell cycle.

[33] For photons of energy above the K edge of phosphorus about 100 eV is lost on average by fluorescence photons per interaction.

sensitive volume. For very small site diameters (< 10 nm) the mean energy deposition per interaction for electron cascades induced by photons above the phosphorus K edge is about twice that for photons below the edge. There are three reasons :

1. KLL transitions from 89% of the transitions to a K shell vacancy. This results in the further development of two vacancy cascades starting from the L shell instead of only a single one following a direct photoelectric interaction in L.
2. The energy imparted at the interaction site is larger the greater the number of electrons released because of higher build-up of charge on the phosphorus atom.
3. The additional K-Auger electron deposits a small fraction of its energy even at such small site sizes.

Table 17

Mean energy deposition $\bar{\epsilon}_F$ around photoelectric interactions in phosphorus as a function of photon energy and site diameter

	Mean energy deposition $\bar{\epsilon}_F$(keV)				
d(/um)	hν (keV) 0.278	1.5	2.128	2.145	4.55
0.0010	0.045	0.052	0.054	0.131	0.129
0.0018	0.056	0.062	0.064	0.146	0.143
0.0032	0.078	0.080	0.082	0.174	0.171
0.0056	0.123	0.111	0.112	0.220	0.222
0.0100	0.180	0.151	0.150	0.272	0.282
0.0178	0.222	0.195	0.189	0.320	0.344
0.0316	0.249	0.255	0.237	0.373	0.425
0.0562	0.265	0.377	0.318	0.458	0.564
0.1000	0.273	0.637	0.497	0.645	0.858
0.1778	0.278	0.965	0.887	1.025	1.510
0.3162	0.278	1.192	1.361	1.421	2.415
0.5623	0.278	1.331	1.686	1.683	3.178
1.000	0.278	1.410	1.884	1.840	3.705
1.778	0.278	1.453	1.994	1.927	4.024
3.162	0.278	1.479	2.059	1.976	4.207
5.623	0.278	1.493	2.094	2.005	4.311
10.000	0.278	1.500	2.113	2.021	4.368

This higher energy deposition in volume diameters less than 10 nm for photons of energies above the phosphorus K edge can be of importance when considering DNA bound phosphorus. If a certain initial energy within a particular sensitive volume, (say 100 eV in a volume of 2 nm diameter) is necessary to produce a significant biological effect then photon interactions with the K shell of phosphorus might, on account of their high local energy deposition, give rise to an enhancement in the DNA damage. However a complete study of the energy deposition in the DNA resulting from photon interactions in the cell nucleus necessitates consideration of the energy imparted in the DNA both due to photon interactions in elements other than phosphorus in the DNA as well as energy being deposited from interactions in the non-DNA parts of the cell nucleus. This problem has been treated by Booz, Humm et al 1983.

Figure 39
Mean energy deposition $\bar{\epsilon}_F$ for photoelectric interactions in phosphorus produced by photons of energies from 279 eV - 4.55 keV as a function of the sensitive site diameter.

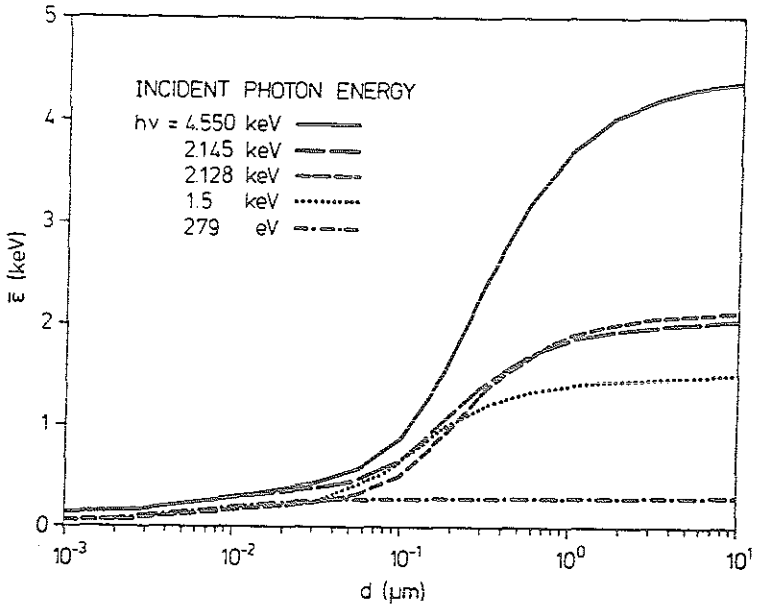

10 Photoelectric interactions in argon

10.1 Argon as a simulant of phosphorus for microdosimetric spectra measurements

A further aim of this thesis was to compliment the theoretical study of energy deposition from photoelectric interactions in phosphorus of the previous section with an experimental investigation of the K edge effect with respect to energy deposition. A well established experimental technique for the measurement of energy deposition in simulated volumes of down to 1 µm diameter was developed by H.H.Rossi (see Rossi 1968). Conventionally this technique employs a tissue equivalent proportional counter with a tissue equivalent gas as a counting gas and measures the number of ion pairs produced in the gas (counting volume) as a function of gas pressure (simulated diameter). For a microdosimetric study of the K edge effect a gas of phosphorus would be preferred in accordance with the relevance of phosphorus in radiation biology. However the few available gaseous compounds of phosphorus such as phosphine PH_3, phosphorus trichloride PCl_3 and phosphorus pentachloride PCl_5 are firstly unsuitable as counting gases and secondly are all highly toxic and corrosive. Therefore for these investigations argon gas was used which not only possesses the appropriate physical properties and is agreeable to work with but also can act as a good simulant for phosphorus.

From a Monte-Carlo simulation of photoelectric interactions in argon, using the computer code as for phosphorus, (section 9) with input data for argon, the agreement in the electron number distribution for phosphorus and argon could be tested. The result has been plotted in figure 40 showing an excellant agreement concerning both the distribution shape and range. The closeness in the two distributions is accredited to the similar size of the two atoms. Also the electron energy spectra are similar because of the comparable shell binding energies, (the K edge of argon is at 3.2 keV, for phosphorus 2.145 keV). Similarity

Figure 40

Electron number distributions for phosphorus and argon irradiated with monochromatic photons of energies just above their respective K absorption edges.

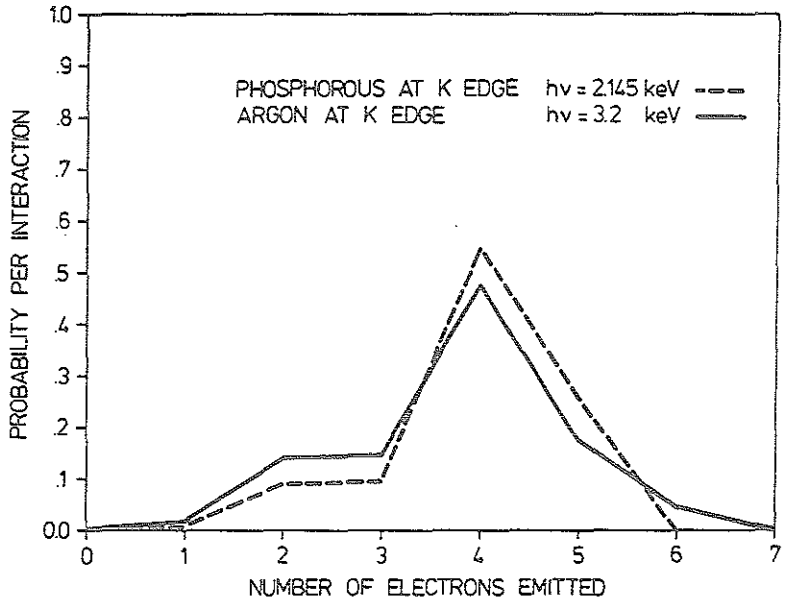

in electron number, electron energies and also in the photon spectra justifies that argon can be used as a good model substance for phosphorus.

The choice of argon as a counting gas for microdosimetric measurements has led to the performing of calculations simulating photoelectric interactions in argon at photon energies corresponding to those applied in the experimental part of this thesis. Electron spectra were generated and then used for energy deposition calculations. The results of those calculations are now briefly discussed before going on to the experimental studies.

10.2 Results of Monte-Carlo simulated photoelectric interactions in argon

10,000 photoelectric interactions were simulated in argon using the technique as described for phosphorus (section 9) for the following five monochromatic photon energies : 4.55 keV (Titanium K_α), 4.09 keV (Scandium K_α), 3.34 keV (Potassium K_α), 2.63 keV (Chlorine K_α) and 2.28 keV (Sulphur K_α). The results obtained for the average electron emission number and the average electron, photon and potential energies are given in table 18 for different photon energies. From individual electron spectra at each of the above five photon energies the mean energy deposition $\bar{\epsilon}_F$ in a spherical volume V, variable diameter, per photon interaction could be calculated for a homogeneous distribution of argon atoms in V. The results of these calculations are given in table 19. They show comparable tendencies to the results for phosphorus both with regard to the difference in energy deposition at photon energies above and below the K edges and also to the general magnitude of energy deposition at corresponding incident photon energies.

Table 18

Average electron number $\bar{n}$, electron energy $\bar{E}$, photon energy $\bar{P}$ and potential energy $\overline{IP}$ of argon irradiated with photons of different energies

$h\nu$ (keV)	$\bar{n}$	$\bar{E}$	$\bar{P}$	$\overline{IP}$
4.55	3.80	4.113	0.305	0.132
4.09	3.79	3.654	0.305	0.131
3.34	3.78	2.908	0.302	0.130
2.63	2.33	2.573	-	0.057
2.28	2.32	2.224	-	0.056

Table 19

Mean energy deposition $\bar{\epsilon}_F$ around sites of interaction with argon atoms for different photon energies at varying site diameter

d(/um)	$h\nu$ (keV)	2.28	2.63	3.34	4.09	4.55
0.0010		0.064	0.065	0.143	0.143	0.144
0.0018		0.071	0.072	0.153	0.153	0.154
0.0032		0.085	0.086	0.173	0.173	0.173
0.0056		0.109	0.111	0.219	0.209	0.209
0.0100		0.156	0.156	0.309	0.283	0.282
0.018		0.232	0.231	0.439	0.414	0.409
0.032		0.317	0.313	0.557	0.575	0.553
0.056		0.420	0.406	0.656	0.798	0.738
0.100		0.603	0.554	0.771	1.089	1.057
0.178		0.984	0.887	0.976	1.418	1.532
0.316		1.466	1.445	1.308	1.926	2.156
0.562		1.805	1.929	2.002	2.585	2.888
1.000		2.010	2.230	2.430	3.078	3.441
1.778		2.126	2.404	2.693	3.382	3.786
3.162		2.193	2.503	2.843	3.557	3.985
5.623		2.231	2.558	2.928	3.656	4.098
10.000		2.251	2.589	2.976	3.711	4.161

10.3 Comparison of the calculated electron emission number distribution with experimental results from Carlson and Krause

Experimental data on the number of electrons emitted following vacancy cascades whether induced by nuclear decay or photoelectric interaction is scarce. Some experimental results are however available on the relative ion abundances following photoelectric induced vacancy cascades in argon gas. Carlson and Krause , 1965, performed these

measurements using a magnetic spectrometer and gave distributions [34] for photon irradiations both above and below the K edge of argon. This gave a special opportunity to test the calculational methods applied in this thesis since the case of argon gas firstly involves no complications due to charge neutralization and secondly the argon atom is small; therefore, the number of inner shell transitions is limited, which presents a fundamental test as to the accuracy of both the calculational method and the basic assumptions of the computer code.

Figure 41 shows the electron number (charge) distribution as measured by Carlson and Krause for X-rays from a titanium target on argon compared with the distribution obtained from Monte-Carlo calculations simulating photoelectric interactions in argon with 4.55 keV (Ti - K_{α}) photons. Figure 42 shows the comparison of the electron number distributions for argon irradiated with X-ray energies below the argon K edge; the experimental results of Carlson and Krause using the X-rays produced by 3 keV electrons on an aluminium target against calculations simulating photoelectric interactions with 2.63 keV (Cl - K_{α}) monochromatic photons.

The agreement with experiment is good in both cases at the low electron number end and at the peak of the distributions. At upper end of the distribution the frequency for the emission of higher electron numbers is greater for the experimental distribution which also extends to higher electron emission numbers than for the calculated distribution. For example from the experimental electron emission number distribution a charge of up to +8 has been measured on the argon atoms when irradiated with titanium X-rays. Computer simulated photoelectric interactions in argon at this energy however permit up to a maximum of only 6 electrons per photon interaction. Also with photon energies below the K edge of argon the experimental maximum electron

[34] The charge on a gas molecule is equal to the number of electrons emitted assuming no charge is neutralizied.

Figure 41
Comparison of the electron number distribution, (charge distribution) from Monte-Carlo calculations with the experimental data of Carlson and Krause, produced by X-rays of energies above the K-edge of argon.

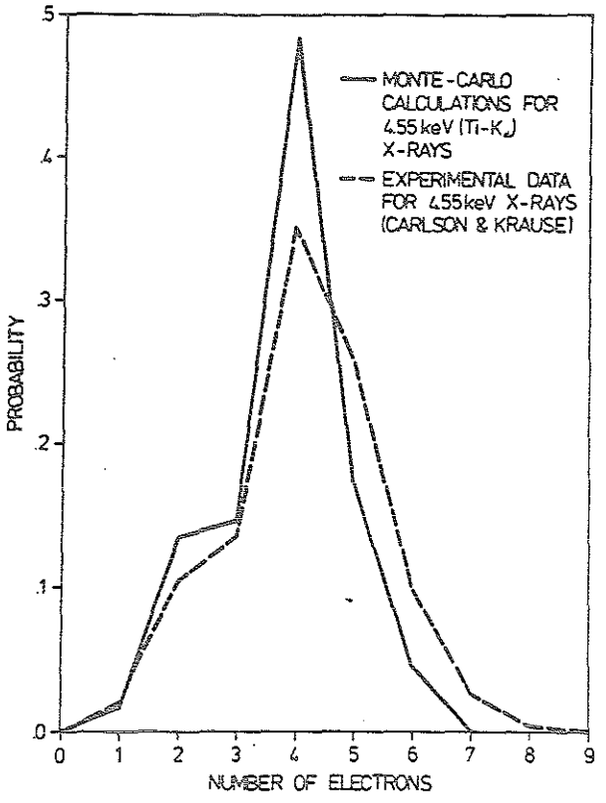

Figure 42
Comparison of the electron number distribution, (charge distribution) from Monte-Carlo calculations with the experimental data of Carlson and Krause, produced by photons of energy below the K-edge of argon.

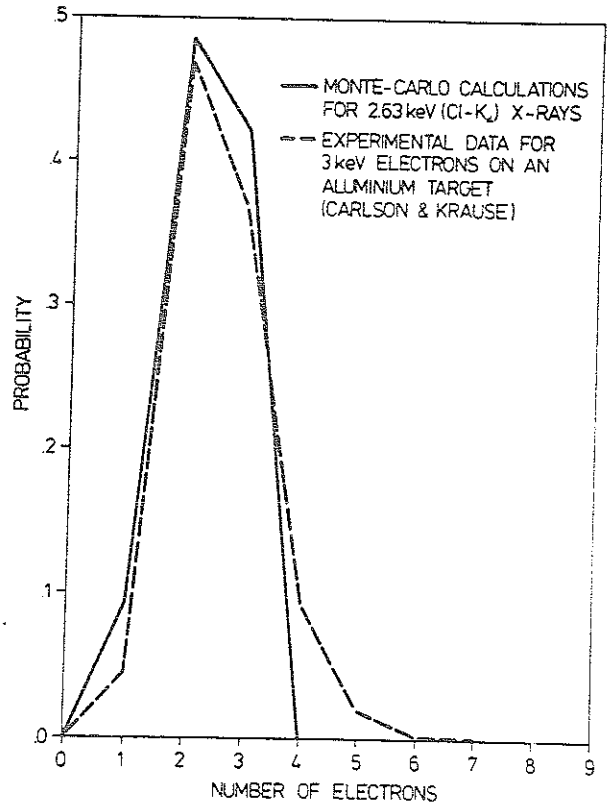

number is 6, (although the probability of 6 electrons being emitted is very small 0.004 i.e. 0.4%), compared to 3 electrons obtained from calculations.

Carlson and Krause accredit this discrepency with the theoretically expected maxima to the process of electron shake-off, i.e. the emission of an orbital electron caused by a sudden change in effective charge of the atom, after either the photoelectric effect or an Auger transition, which is not accounted for in the computer code. This electron shake-off would certainly shift the electron number distribution to higher electron numbers and could even produce an argon molecule irradiated with X-rays of energy below the K edge with a charge of +6 if both the photoelectric interaction and the two ensuing Auger transitions produced electron shake-off

PART III

ENERGY DEPOSITION MEASUREMENTS FOR PHOTOELECTRIC INDUCED VACANCY CASCADES IN ARGON

11 Techniques of experimental microdosimetry

11. Microdosimetry with Rossi counters

Experimental microdosimetry began with Rossi and Rosenzweig 1955 who developed a technique for measuring spectra of energy deposition $f(\epsilon)$ in small simulated tissue volumes of the order of a few micrometers (cellular and sub-cellular dimensions) when irradiated with ionizing radiation. Their technique involved the construction of a special spherical proportional counter (the so called Rossi couter) made with walls of tissue equivalent plastic filled with a tissue equivalent gas acting as both the sensitive volume as well as a counting gas. A counter with matching walls and counting gas represents, when placed in a radiation field, an instrument with a homogeneous response; the Fano principle states that, " in a medium of constant atomic composition, the fluence of secondary particles [35] is constant if the fluence of primary particles is constant and that under this condition the fluence is independent of the density variations provided the interaction cross sections and stopping powers of the particles are independent of density " Fano 1954, ICRU 1983.

Since the physical dimensions of the chamber are fixed, the sensitive counting volume is regulated by changing the gas pressure. The pressure p in pascal required to simulate a unit density tissue diameter d_s is given by equation 34 (Hogeweg 1978)

$$d_s = \frac{p}{p_n} \cdot \rho^{d} \qquad (34)$$

where ρ is the density of the gas at NTP,

d is the diameter of the gas volume in the counter and p_n the normal pressure in pascal at which the density is defined

However this technique to simulate small tissue

[35] Secondary particles are particles to which energy has been transferred from the primary beam.

equivalent volumes has an inherent limitation. At a certain gas pressure, which depends on the counting gas but is usually about 500 Pa, the multiplication region of the proportional counter becomes so large that the signal measured in the counter is no longer a function of the number of initial ion pairs alone but also depends on their location of origin within the counter.

For gas pressures above 500 Pa (corresponding to a simulated tissue diameter of 0.3 μm in a 2 inch i.e. 5.08 cm Rossi counter), and with ideally tissue-equivalent materials, the number of ion pairs produced by particles traversing the simulated volume should be equivalent to the number of ion pairs that would be produced in a tissue medium of the same dimension. Further, in measuring the number of ion pairs created in the sensitive volume of the counter, one has a direct relation to energy deposition through the W-value giving the average energy expended by the incident particle per ion pair formed. The W-value depends on the type of counting gas, the radiation and its energy, and is typically 30 eV/ion pair.

Each particle traversing the sensitive volume of a Rossi counter produces a certain number of initial ion pairs which after gas multiplication produces a signal on the central wire proportional to the energy deposited by that particle. By electronic processing and storage of each individual event of charge collection on the central wire a spectrum of these events is obtained which represents the spectrum of energy deposition in the sensitive volume and is a characteristic of the type of radiation. Another important factor determining the shape of an energy deposition spectrum is the path-length distribution of the secondary particles in the sensitive volume (or chord length distribution if all secondaries have a range sufficiently greater than the diameter of the sensitive volume) and this will depend on the counter geometry. More about this subject will be said in section 16.

From an energy-deposition spectrum, $f(\epsilon)$, the conversion to a lineal-energy distribution, $f(y)$, results from dividing each individual component of ϵ by the mean

chord length of the sensitive measuring volume, $\bar{l}$, (see Part I, section 6.1) This distribution f(y) plotted against y and the alternative representation, d(y) (the so-called dose distribution of y) are of particular importance in microdosimetry. These mean values $\bar{y}_F$ and $\bar{y}_D$, defined by equations 35 and 36, are measures of the quality of the radiation and are reputed to be linked to the biological effectiveness of the radiation field e.g., by the dual radiation action hypothesis of Kellerer and Rossi, 1972.

$$\bar{y}_F = \frac{\int_o^\infty yf(y)dy}{\int_o^\infty f(y)dy} \qquad (35)$$

$$\bar{y}_D = \frac{\int_o^\infty y^2 f(y)dy}{\int_o^\infty yf(y)dy} = \frac{1}{\bar{y}_F}\int_o^\infty y^2 f(y)dy \qquad (36)$$

More detailed accounts of the experimental techniques in microdosimetry are to be found by Rossi 1968, Srdoc 1970, Booz 1976 and Hogeweg 1978.

11.2 A microdosimetric method for low-energy photons

In order to apply microdosimetric techniques for energy deposition measurements at low photon energies, which is the aim of this work, considerable modifications to the traditional methods are required. In this section a very brief introductory outline of the general approach employed in these investigations is given, as well as mentioning some of the problems. A more detailed treatment is to be found in the remaining sections of the thesis.

The system used for the measurements consisted of an X-ray generator used in a configuration with secondary targets of highly pure materials to act as a variable energy source and two microdosimetric chambers : a spherical Rossi counter and self-built cylindrical one. Since the photons employed in this work are of extremely low energy, from 2.3 keV - 5.4 keV, too low to be able to penetrate the walls of either counters, an isotropic irradiation of

the counter proved impossible and it was therefore necessary to design small entrance windows (of 20 /um thick mylar with a 1 mm diameter opening) for both counters. All measurements were performed under this narrow beam geometry, the X-ray beam orientated perpendicular and traversing a diameter of the counters. Such an irradiation produces a line of photoelectric interactions along the diameter of the chamber with the emission of a photoelectron preferentially at 90° to the incident beam and with an isotropic emission of Auger electrons. This approximate line source of secondary electrons in the counter volume gives neither a /u-random path-length distribution nor one of i-randomness (for a definition of /u and i-randomness see section 16). Since the path-length distribution is such an important factor in determining the shape of energy deposition spectra this problem required detailed study (section 16) for the special geometrical situation dictated by the experimental conditions.

A further consideration concerning the path-length distribution from low energy X-ray measurements is that all of the secondary electrons produced are of very short range [36], many with ranges far shorter than that of realizable sensitive volume diameters. However this has a certain advantage in that at relatively small simulated diameters (> 8 /um) i.e. gas pressures > 1 x 10^4 pascal, one has complete secondary electron absorption within the chamber and obtains a full energy peak corresponding to the incident photon energy. Such an energy spectrum can be useful for calibration purposes and for measuring the resolution and quality of the counter.

Two last problems to be mentioned concern boundary effects between the solid counter and the gaseous sensitive volume. The first relates to the loss of charge-particle equilibrium at the window interfaces where the X-ray beam enters and leaves the sensitive volume. This problem is

[36] An electron of 4 keV energy corresponding to a photoelectron from the M shell of argon irradiated with scandium K_α X-rays has a range of only 0.6 um in unit density tissue.

avoided in traditional microdosimetry by using materials of similar constitution as both counter wall and gas so that the Fano principle applies. In these investigations where irradiating through the counter wall is not possible due to the low photon energy and where argon is required as a counting gas a certain material mismatch seemed inevitable.

Secondly, and perhaps more seriously, low-energy electrons, in traversing the gas-wall interface i.e. in escaping the measuring volume, may undergo a process of discontinuous energy loss at the boundary layer. Electrons which strike the counter walls can give rise to secondary electron emission leading to an overestimation of the local energy deposition. As part of these investigations it was therefore also necessary to examine this wall effect.

Following this general introduction to the methods and problems of low-energy photon microdosimetry the next three sections discuss the experimental system and execution of the measurement in more detail.

12 Experimental system components

This section concentrates on the individual components of the experimental microdosimetric system : the X-ray source, detectors, vacuum system and the signal processing electronics.

12.1 The X-ray source

As a primary source of X-rays a Siemens X-ray generator, trade name Kristalloflex 4, was used. This generator comprises of two parts : the power supply and the X-ray tube which is interchangeable. Siemens manufacture X-ray tubes with anticathodes from chromium (Z=24) for low-energy X-ray work to tungsten (Z=74) for the higher energy X-rays. In this thesis measurements were performed with both a chromium and molybdenum X-ray tube (figure 43), which deliver the strong characteristic X-rays of the anticathode material on a continuous bremsstrahlung background spectrum between 0 keV and the operating tube voltage.

To obtain monochromatic X-rays of different energies the fluorescence photons of secondary target materials of high purity (> 99.7%) were used being placed in a special target holder attached to the X-ray tube window. Secondary target materials were chosen so as to give X-ray energies as near to the argon K-edge (3.2 keV) as possible, e.g. vanadium 5.0 keV, titanium 4.55 keV, scandium 4.13 keV and sulphur 2.31 keV. The optimum fluorescent photon energies for a study of the argon K-edge would be from targets consisting of the elements on either side of argon in the periodic table i.e. potassium and chlorine with photon energies 3.34 keV and 2.63 keV respectively. Potassium targets were made by pressing powdered potassium carbonate into tablet form with a hydraulic press; chlorine targets were made in the same way using the compound lithium chloride. The extremely low energy of carbon, oxygen and lithium X-rays were found not to disturb the desired X-ray line being totally absorbed before reaching the detector. One final lithium bromide target of 99.7% purity was used

Figure 43
The Siemens X-ray generator.

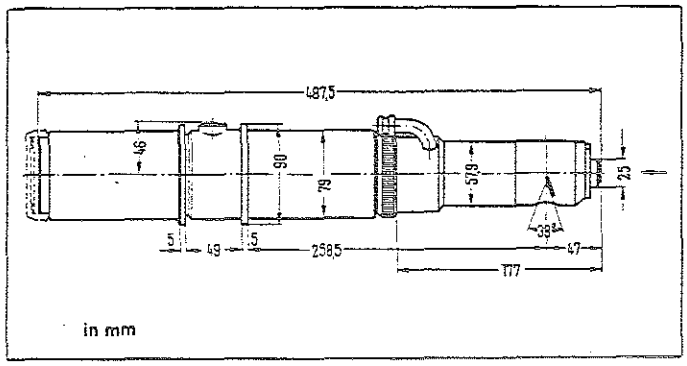

Figure 44
Irradiation geometry.

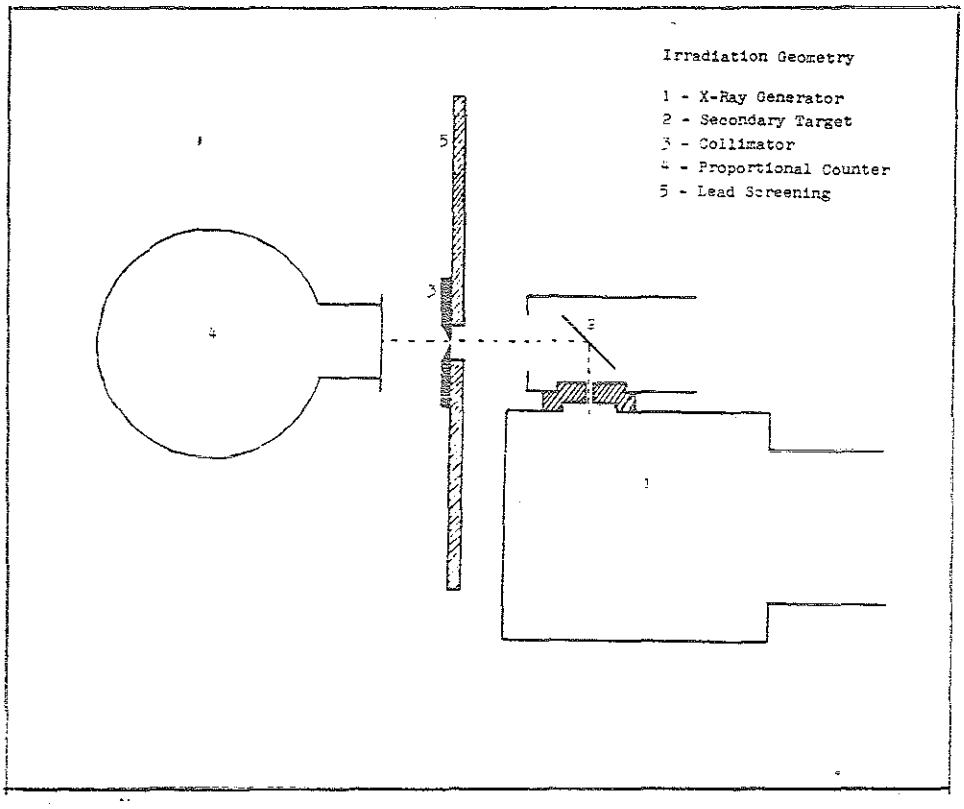

giving bromine X-rays at 12.087 keV.

These targets were slotted into a target holder which was so constructed that the primary beam interacted only with the target and not with any part of its holder which could give additional unwanted X-ray lines. With a target orientation of 45° to the primary beam a maximum yield of secondary fluorescence photons (emitted preferentially at 90° to the primary beam direction) could be extracted from the main beam with minimum interference from the primary X-rays (figure 44). 2 mm of lead shielded the detector from the primary beam, the secondary beam reaching the detector through a small collimator centrally aligned between the secondary target and the counter window.

12.2 The detectors

12.2.1 Basic principles of a proportional counter

For the purpose of microdosimetry the proportional counter has proved to be the most adaptable and appropriate radiation detector. It has a relatively high resolution, is simple and is a most suitable detector for simulating tissue media. The basic construction of a proportional counter is the same as for an ionization chamber or Geiger-Muller tube, i.e. a vacuum-tight chamber filled with an appropriate gas and an ultra-thin central wire electrically isolated from the counter walls. By applying a high potential between the central wire and the walls, electrons produced by ionizing radiation traversing the chamber are attracted to the central wire. When they arrive at the so-called multiplication region, usually a short distance from the central wire, the electric field becomes so strong that they gain sufficient kinetic energy to create further ion pairs. In this way a cascade process, so-called Townsend avalanche, may develop whereby each created free electron has the potential of producing more free electrons by the same process.

In the so-called proportional region, the number of

electrons collected on the central wire following a Townsend avalanche is proportional to the initial number of ion pairs produced in the chamber. The degree of charge multiplication achieved by such a cascade process, often referred to as the gas gain, can be anything between one and several thousand. The great advantage of the proportional counter is that a high amplification can be achieved within the detector itself leading to an improved signal to noise ratio.

In this work measurements have been performed with two counters : a commercial spherical Rossi counter and a self-constructed cylindrical counter.

12.2.2 The Rossi counter

The first experimental microdosimetric investigations were performed using the spherical Rossi counter shown in figure 45. This counter has an inside diameter of 5.08 cm (2 inch) and tissue equivalent wall (A-150 plastic) of 6 mm thickness. As a central wire electrode a 0.12 mm steel wire suspended across a diameter of the chamber is held taught with a spring. The chamber also contains a helix electrode (diameter 0.127 mm, 3 mm pitch, at a distance of 1.6 mm from the central wire) to provide a cylindrical electric field around the central wire. Inside the chamber wall there is a small opening into which a specially designed vacuum tight plug can be fitted. This plug contains a thin 20 µm thick mylar window and a 1 mm collimator allowing a narrow beam of X-rays to traverse the diameter of the chamber.

Lastly the counter contains two vacuum connections : the first one used for evacuating the chamber and the second for filling it to the desired pressure with the counting gas.

12.2.3 Cylindrical counter

Due to unexpected difficulties, (see section 15), encountered in performing low-energy photon microdosimetry

Figure 45
The Rossi counter with low energy X-ray window.

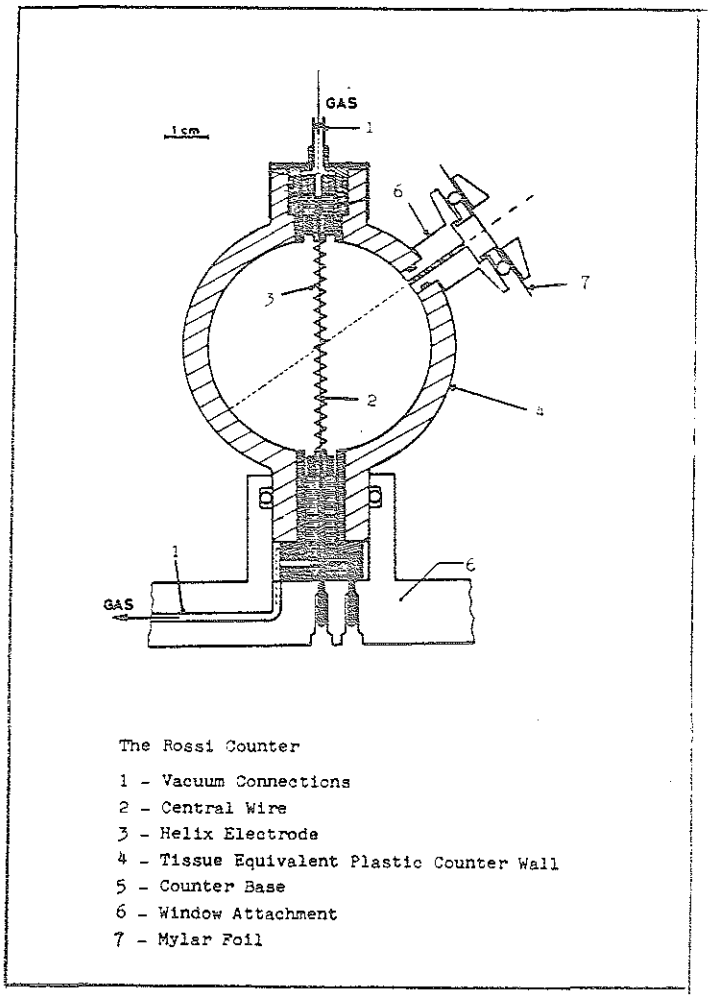

The Rossi Counter

1 - Vacuum Connections
2 - Central Wire
3 - Helix Electrode
4 - Tissue Equivalent Plastic Counter Wall
5 - Counter Base
6 - Window Attachment
7 - Mylar Foil

Figure 46
The cylindrical counter.

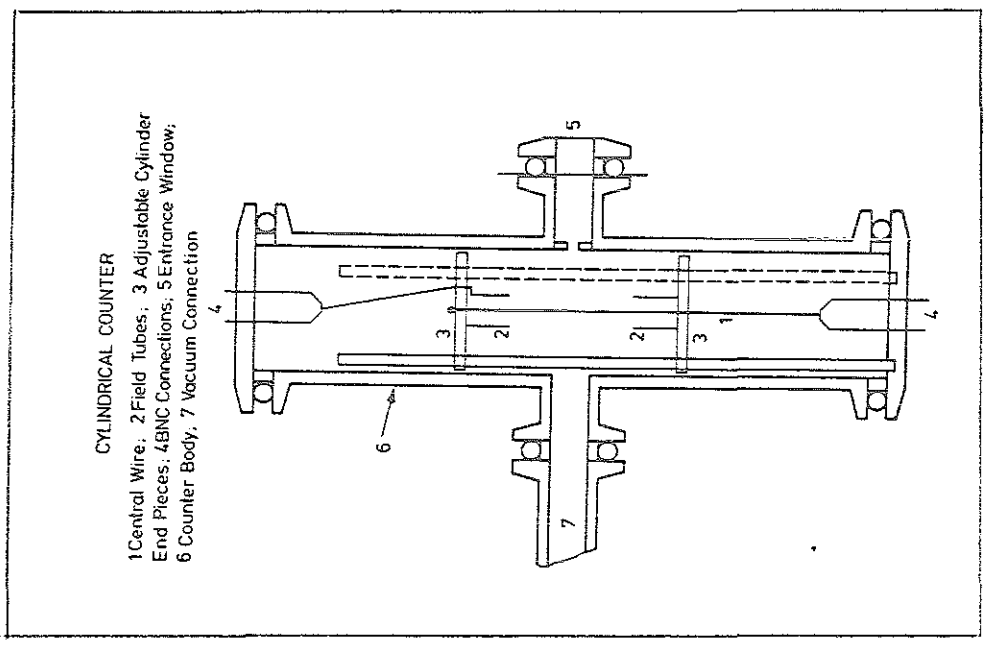

with the Rossi counter described above, it was necessary to repeat the planned measurements with a self-constructed cylindrical counter. The basis of this counter (figure 46) is a standard aluminium Leybold vacuum cross piece (33.5 mm inside diameter). The electrodes, comprising of a central wire (1 mm diameter steel) and two field tubes (6 mm inside diameter, 0.2 mm thick), were mounted on a specially designed frame which could be assembled as a single unit outside of the chamber and then simply slid into place in the counter body. The frame supporting the electrodes consists of a standard vacuum blind flange into which three thin aluminium rods (2 mm diameter, 60° apart) are screwed. These rods [37] support two 32 mm diameter teflon discs onto which the field tubes are mounted. The construction has been made in such a way that the height of the cylindrical counting volume (determined by the space between the ends of the field tubes) can be adjusted as desired [38]. The central wire passes centrally through both discs and is connected to the outside of the chamber via a vacuum tight BNC plug soldered into the blind flange at one end and held taught by a small ball bearing at the other. Electrical connection to the field tubes results through a second BNC plug at the other end of the counter whereby the contact to the field tube at the far end is made via a screened cable.

Irradiation is performed through the chamber cross piece. One arm serves as an entrance for the X-ray beam and contains a 20 µm mylar window pressed between two flanges. The other serves both as an exit window for the incoming X-ray beam and as a vacuum connection for evacuating and filling the chamber with argon gas. In order not to

[37] The rods were specially made to pass as near to the counter walls as possible, where the electric field gradient is small, so as to minimize the field distortion in the measuring volume

[38] An adjustment of the cylinder height is a quick operation requiring only a replacement of the central wire.

distort the cylindrical electric field at the chamber intersection (which could severely reduce the counter resolution) a 2 mm aluminium collimator and a conducting 20 /um thick mylar foil (aquadag coated) were fitted flush with the inner cylindrical measuring volume wall in the X-ray inlet arm and in the output arm respectively.

12.3 Vacuum system

The vacuum equipment (figure 47) consists of a rotary pump with which to evacuate the measuring chamber attached to one outlet of the Rossi counter and a supply of argon gas to fill the chamber at a second outlet, (for the cylindrical counter both resulted through a single connection). By opening valve V_1 the system can be evacuated and the pressure in the chamber checked at two aneroid manometers M_1 (10^2 - 10^5 Pa) and M_2 (10^1 - 10^4 Pa) and a thermatron pressure guage M_3 (10^{-1} - 10^2 Pa). In closing valve V_1 and opening V_2, gas can slowly be let into the chamber using the fine needle value V_3 and the reading on the aneroid manometer for an accurate setting of the chamber gas pressure.

12.4 Electronic signal processing

A 3 keV photon which deposits its total energy in the chamber will produce on average about 100 ion pairs if the W-value is 30 eV. Assuming a gas gain of 10^3 then about 10^5 electrons will be collected on the counter central electrode representing a charge of $10^5 \times 1.6 \times 10^{-19}$ C. This small charge pulse is collected at the input stage of a specially developed charge-sensitive preamplifier [39]. The preamplifier integrates the charge pulse on a 0.5 pF capacitor to produce a voltage pulse of $1.6 \times 10^{-14} / 0.5 \times 10^{-12} = 32$ mV whereby it is critical that the input capacitance is kept as small as possible in order to minimize the

[39] A development of the electronic division of the CRR-Ispra.

Figure 47

Schematic diagram of the measurement system

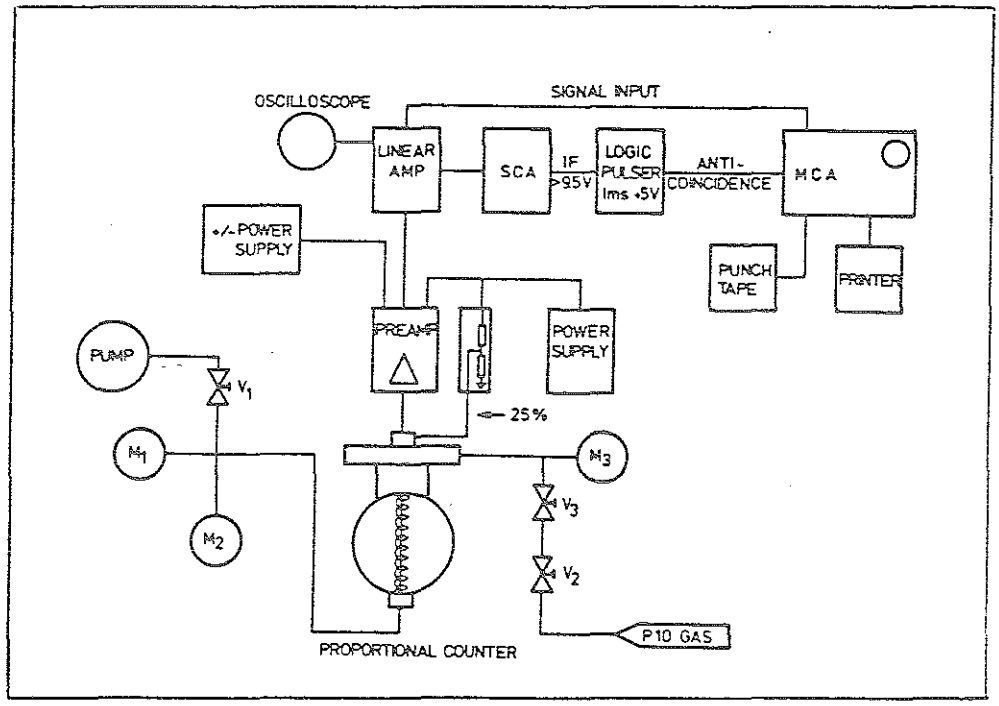

noise level. The principle function of the preamplifier is to optimize the signal to noise ratio at as an early stage as possible in the signal processing and to clip the charge on the preamplifier input with a time constant of 40 μs to avoid charge saturation. In addition, the preamplifier matches the high impedance of the detector to the low input impedance of successive amplifying stages.

Two main amplifiers were used in this work : a Tennelec 205A Oak Ridge linear amplifier and a Canberra model 2021 spectroscopy amplifier. Both exhibited a broad range of linear amplification from 1 - 3000, where equipped with Gaussian pulse shaping and a base line restorer. The amplified and shaped pulses were collected and stored on a 4K Canberra Series 80 multi-channel analyser, 1K of storage i.e. 1024 channels, being reserved for each individual spectrum.

The quality of the pulses could be observed on a Tektronix oscilloscope. One disturbance which needed elimination was occasional pulse overshoots leading to a saturation of the main amplifier for a period of up to 100 μs. Such saturation pulses destabilize the amplifier baseline and are therefore a potential source of spectrum distortion. In order to avoid the measurement of pulses arriving at the ADC when the amplifier has only partly recovered from saturation, a single channel analyser was used to discriminate pulse heights greater than 9.8 V and trigger a 1 ms 5 V logic pulse which was fed to the multichannel analyser as a coincidence signal with the signal input. By operating the ADC in anticoincidence it was possible to close the gate for periods long enough (1 ms) to assure a fully restabilized amplifier baseline. The corresponding live time correction was performed automatically by the analyser.

A block diagram of the various signal processing stages is featured in figure 47. Normally the quality of any such functioning system is limited by the performance of the weakest component in the chain. In nuclear instrumentation it is usually the preamplifier, directly between the detector and the first amplification stage, that is

the deciding factor for the overall signal to noise ratio. To measure the preamplifier noise level requires disconnecting the detector and applying a test pulse from a high precision pulser to the input with a 50 μs time constant in order to simulate the detector output. The extent of the peak broadening, usually measured as the full width at half maximum (FWHM) of the applied test pulse, expressed in charge or energy units, is then a specification of the noise figure. Another is the number of electrons (RMS) obtained by dividing the FWHM in charge units by 2.35 times the electron charge 1.6×10^{-19} C. All preamplifiers employed in this work were tested in this way and showed noise figures of between 120 - 240 electrons RMS. With the counter attached the noise level rose to between 320 - 440 electrons RMS.

13 Theoretical expectation of the system

It is always extremely valuable to make an estimation of the size of the signal which one would expect to measure at the counter under precisely the experimental conditions employed in the measurement. This helps in clarifying the extent to which the various experimental parameters determine the signal magnitude and therefore assists the optimization of the measurement configuration.

The number of photon interactions in the measuring chamber depends principally on five factors :

1. initial intensity of the primary X-ray beam,
2. geometric attenuation (the solid angle between the X-ray tube and secondary target, and secondary target and counter window,
3. absorption of photons in their passage between the source and detector,
4. transfer function of the secondary target foil i.e. the number of primary photon converted to secondary photons of the desired monochromatic energy,
5. the number of photon interactions in the sensitive counter volume.

1) The intensity I_p of the primary chromium X-ray beam was determined using the Beatty formula (Bertin, 1978)

$$I_p = k\ i\ Z\ V^2 \qquad (37)$$

where i is the beam current,
V the tube voltage
Z the atomic number of the tube target element
and k a dimensionless constant 1.5×10^{-9}

Operating the tube (chromium target Z = 24) at 10 kV with a 6 mA beam current one obtains a primary beam intensity I_p of 2.16×10^{-2} J/s i.e. 1.35×10^{14} keV/s. Taking the average X-ray energy to be 5.47 (the mean K_α, characteristic X-ray energy) this beam intensity corres-

ponds to 2.47×10^{13} photons per second.[40]

2) The geometric attenuation factor of the beam, G, depends on the product of the solid angle, $\Omega_1/4\pi$, between the tube window and secondary target foil and, $\Omega_2/4\pi$, between the target and detector entrance-window (figure 48). In this work a reduction by a factor of 0.56×10^{-18} in the beam intensity is to be expected assuming the beam to be isotropic. However this is a gross underestimation since the emission beam from both the X-ray tube and secondary target is preferentially at 90° to the incident electron/photon beam at such low energies.

3) The loss in the beam intensity due to photon absorption, A, results from two components : absorption of the primary beam in the X-ray tube window (0.5 mm beryllium) and the air layer between tube and target, as well as absorption of the secondary beam in the air between the target and detector window and the mylar window of the counter. The reduction in the photon beam intensity A, due to absorption is given by the expression,

$$A = \exp\left[-\left(\frac{\mu}{\rho}\right)_{Be,\lambda_p} \rho_{Be}\, x_1 - \left(\frac{\mu}{\rho}\right)_{air,\lambda_p} \rho_{air}\, x_2 - \right.$$
$$\left. - \left(\frac{\mu}{\rho}\right)_{air,\lambda_p} \rho_{air}\, x_3 - \left(\frac{\mu}{\rho}\right)_{my,\lambda_s} \rho_{my}\, x_4 \right] \qquad (38)$$

where $\left(\frac{\mu}{\rho}\right)_{Be,\lambda_p}$ and $\left(\frac{\mu}{\rho}\right)_{air,\lambda_p}$ are the absorption cross-section for beryllium and air at the primary beam wavelength λ_p and $\left(\frac{\mu}{\rho}\right)_{air,\lambda_s}$ and $\left(\frac{\mu}{\rho}\right)_{my,\lambda_s}$ the absorption cross-sections for air and mylar at the secondary beam wavelength λ_s,
x_1, x_2, x_3 and x_4 are the corresponding thicknesses of the respective absorption layers.

[40] The correct average energy of on X-ray beam is the weighted sum of the average characteristic line spectrum and the bremsstrahlung ($\simeq 2/3\ E_{max}$, where E_{max} is the maximum photon energy). In this case the average characteristic line energy is a good approximation.

A prior knowledge of the dimensions of the experiment would give a value of 0.27 for A.

4) The transfer function T for the secondary target is the ratio of the primary beam intensity I_1 incident on the target foil at an angle $\emptyset$ to the intensity I_2 of the secondary fluorescent photon beam I_2 in the direction ψ. Considering an interaction in the target foil at a depth t then the total fluorescence photon intensity I_2 is the sum produced by interactions at each consecutive layer of thickness t from t = 0 to t = t_o (figure 48, see E.P.Bertin, 1978).

Figure 48
Irradiation geometry of primary beam on the secondary fluorescence targets.

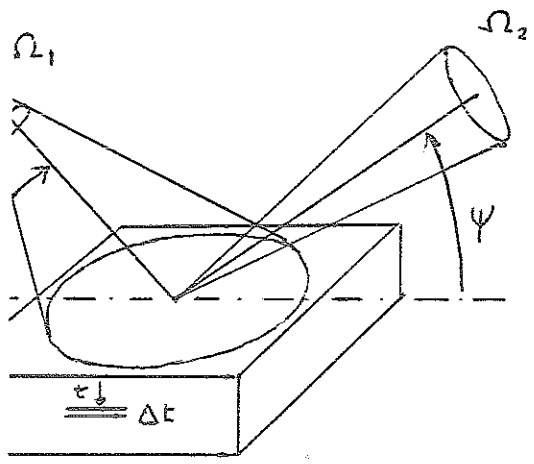

Expressing this mathematically the fraction of incident photons penetrating to a depth t is

$$\exp\left[-\left(\frac{\mu}{\rho}\right)_{\lambda_p}\rho t \operatorname{cosec}\emptyset\right]$$

where $\left(\frac{\mu}{\rho}\right)_{\lambda_p}$ is the absorption cross section of the target material, density ρ for the primary beam energy.

The fraction of photons absorbed in a layer of thickness Δt at this depth t is

$$\left(\frac{\mu}{\rho}\right)_{\lambda_p} \rho \, \Delta t \, \operatorname{cosec} \phi$$

The fraction of interactions giving rise to a K shell fluorescent photon is determined firstly by the proportion of interactions in the K shell of the target material $(r_K - 1) / r_K$ where r_K is the jump ratio of the target atom and secondly by the fluorescence yield for the K shell ω_K.

The fraction of these secondary fluorescent photons emitted in a direction ψ escaping reabsorption is

$$\exp \left[- \left(\frac{\mu}{\rho}\right)_{\lambda_s} \rho t \operatorname{cosec} \psi \right]$$

where $\left(\frac{\mu}{\rho}\right)_{\lambda_s}$ is the absorption cross section of the target for the secondary beam.

Writing the whole expression for the transfer function T

$$T = \frac{I_2}{I_1} = \left(\frac{\mu}{\rho}\right)_{\lambda_p} \operatorname{cosec} \phi \cdot \omega_K \cdot \frac{(r_K - 1)}{r_K} \cdot \int_0^{t_o} \exp \left[- \left(\frac{\mu}{\rho}\right)_{\lambda_p} \rho \operatorname{cosec} \phi - \left(\frac{\mu}{\rho}\right)_{\lambda_s} \rho \operatorname{cosec} \psi \right] t \, dt \qquad (39)$$

and integrating equation (41) over the target thickness one obtains

$$T = \frac{\left(\frac{\mu}{\rho}\right)_{\lambda_p} \operatorname{cosec} \phi \cdot \omega_K \cdot (r_K - 1)}{\left[\left(\frac{\mu}{\rho}\right)_{\lambda_p} \operatorname{cosec} \psi + \left(\frac{\mu}{\rho}\right)_{\lambda_s} \operatorname{cosec} \psi \right] r_K} \cdot \left(1 - \exp \left[- \left(\frac{\mu}{\rho}\right)_{\lambda_p} \rho \operatorname{cosec} \phi - \left(\frac{\mu}{\rho}\right)_{\lambda_s} \rho \operatorname{cosec} \psi \right] t_o \right) \qquad (40)$$

For a scandium target where $\phi = \psi = 45^\circ$, T = 0.025 i.e. 2.5% of the incident photons are reemitted as fluorescent scandium $K_{\alpha,\beta}$ photons.

5) Following the attenuation due to the factors 2) to 4) the photon intensity arriving at the chamber is I_{ch}; a fraction ΔI_{ch} is absorbed in the sensitive volume given by

$$I_{ch} = \exp \left[- \left(\frac{\mu}{\rho}\right)_{\lambda_s} \rho \, d \right] \qquad (41)$$

where d is the simulated tissue-equivalent diameter. For a simulation of 1 µm tissue ΔI_{ch} is 3.8×10^{-3}

The expected number of photoelectric interactions induced in the counter sensitive volume by scandium K X-rays per second, N_{ch}, is given by the initial primary beam intensity in number of photons per second, N_p, multiplied by each of the reduction factors 2) - 5).

$$N_{ch} = N_p \; G \; A \; T \; \Delta I_{ch} \qquad (42)$$

Putting in the various values for the experimental configuration here one obtains for N_{ch}

$$N_{ch} = 2.47 \times 10^{13} \times 0.56 \times 10^{-8} \times 0.27 \times 0.025 \times 3.8 \times 10^{-3}$$
$$= 3.6 \text{ photoelectric interactions/second}$$

The actual number of photon interactions experimentally measured under these conditions was about 50 per second for the scandium foil, higher than the number estimated because of the pessimistically choosen geometric reduction factor. For the chlorine X-rays (a photon energy below the argon K-edge) the intensity was about 20 times smaller. Therefore great care had to be taken in the experimental layout in order that the desired monochromatic X-ray intensity is maximal without contamination from the primary beam.

14 Experimental parameters and execution of the measurement

14.1 Measurement of the X-ray beam with a solid state detector system

A high resolution lithium-drifted silicon detector from Canberra, Series 7300, was used to test the intensity and monochromaticity of the fluorescent X-ray beams from the secondary targets. Care was taken that the measurements were performed under the same beam geometry as those with the Rossi and cylindrical proportional counter so that the measured spectra differ singly with respect to the detector response. Figures 49 - 51 show spectra measured for the principal secondary fluorescence targets empoloyed : scandium, potassium carbonate and lithium chloride. Sharp peaks are visible at the corresponding $K_{\alpha,\beta}$ line of the target material and for the scandium target the detector can even clearly distinguish between the K_{α} line at 4.09 keV and the K_{β} at 4.66 keV, the detector having a resolution of about 200 eV at this energy. However, for the potassium target (figure 50), chromium K_{α} , K_{β} , characteristic photons elastically scattered off the secondary target become noticeable. This both undesirable and unadvoidable source of X-ray background is of nearly constant intensity irrespective of the secondary target material, whereas the intensity of the fluorescent photons arriving at the detector rapidly decreases with decreasing target atomic number. This is due to the increase in absorption between target and detector of the lower fluorescent photon energies. Therefore, the ratio fluorescent photons to Rayleigh scattered photons, decreases in the measured intensities, the lower the atomic number of the target. For the range of energies of interest in this work, with the scandium target the Rayleigh scattered contribution is insignificant, for the chloride target scattering contributes about 50% to the overall measured intensity [41].

Finally, in order to examine whether the collimator-window attachment results in a degradation of the secondary

Figure 49
X-ray beam from the scandium target measured with a Si-Li detector.

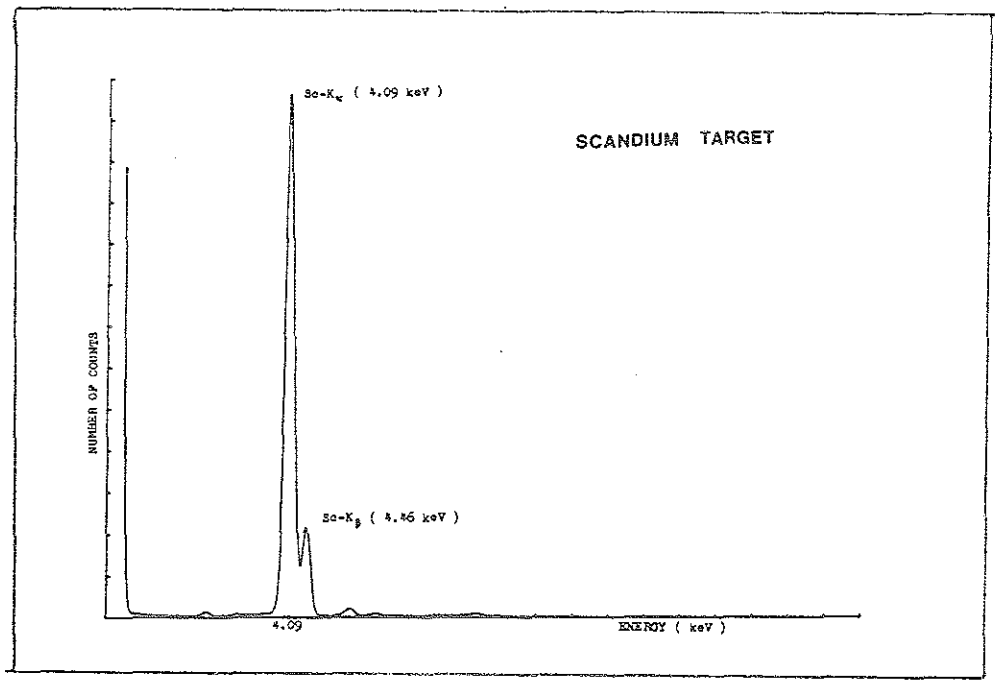

Figure 50
X-ray beam from the potassium carbonate target measured with a Si-Li detector.

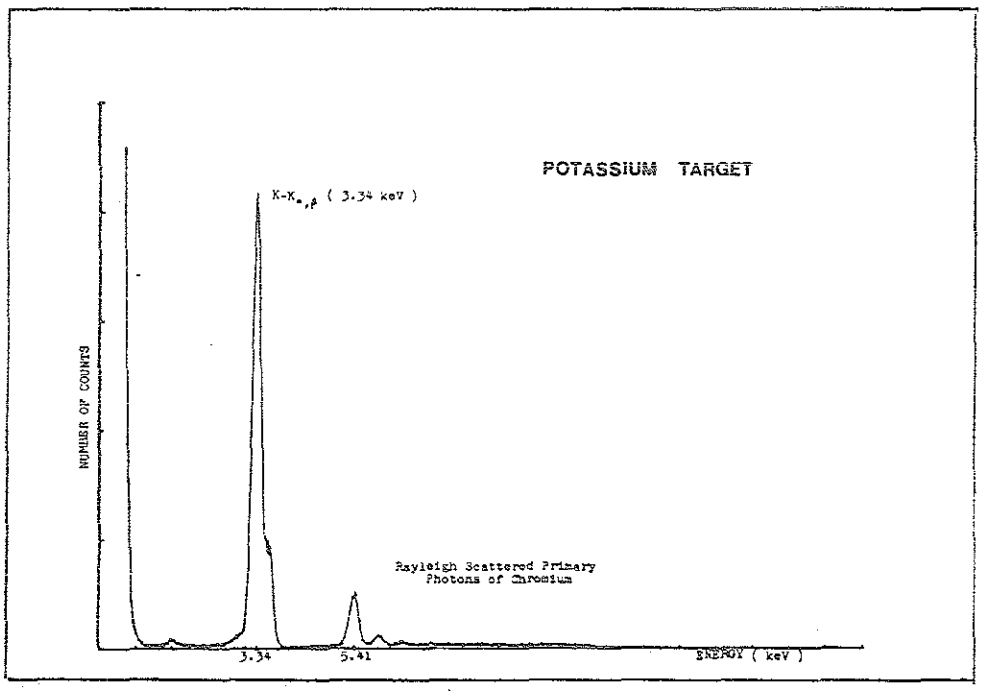

Figure 51
X-ray beam from the lithium chloride target measured with a Si-Li detector.

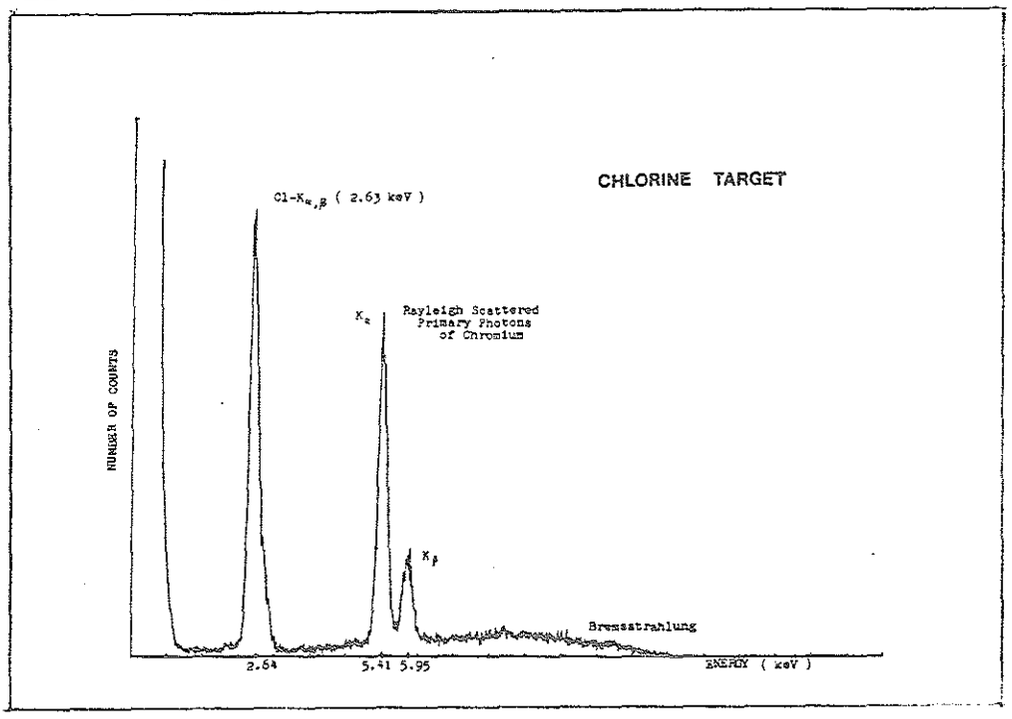

Figure 52
X-ray beam from the scandium target measured behind the Rossi-counter window attachment with a Si-Li detector.

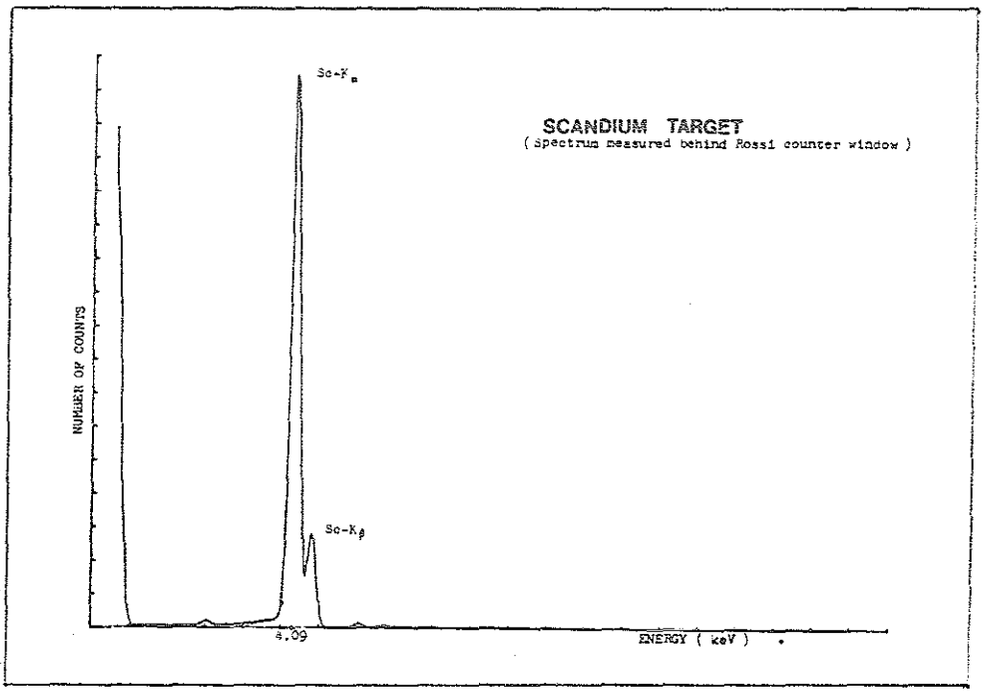

beam spectra, further measurements were undertaken with the Si(Li) detector behind this collimator-window piece, i.e. the Rossi counter collimator-window was suspended 1 mm above the Si(Li) detector which was sufficently screened so that only photons traversing the window could actually be detected. Figure 52 demonstrates that the monochromaticity of the scandium fluorescence beam is maintained. Only the intensity of the detected signal is correspondingly reduced due to the higher beam collimation.

14.2 Simulation of small tissue-equivalent volumes using argon counting gas

For the purpose of these investigations argon was used as a counting gas but not in a pure form. Preliminary investigations performed with pure argon incurred difficulties due to the unstable operation of the counter. This problem arises when using monatomic counting gases which during the gas multiplication can lead to certain excitation states which fall to the ground with the emission of ultra-violet light. These UV photons are absorbed in the counter walls, releasing lightly bound electrons from its surface which subsequently create further ion pairs and thus lead to counting instabilities. For this reason all measurements reported in this thesis employed the commercially available counting gas P10 (90% argon, 10% methane). Methane absorbs the UV photons without electron emission and thus leads to a stable operation of the proportional counter.

The effect of the 10% methane on the low-energy photoelectric cross section is shown in figure 53 for photon energies from 0.1 keV - 10 keV [42]. The difference from

[41] Measurements performed with the proportional counters show a smaller scattering contribution (see chapter 15 and 17) which might be due to lower absorption in the mylar counter window (the Si(Li) detector has a 22.5 µm beryllium cryostat window 3 mm behind which the actual detector is seated).

[42] These calculations were performed using the photon cross section programme described in Part II, section 7.1.

Figure 53
Comparison of the photoelectric mass absorption cross section for pure argon with P10 gas,(90% argon - 10% methane).

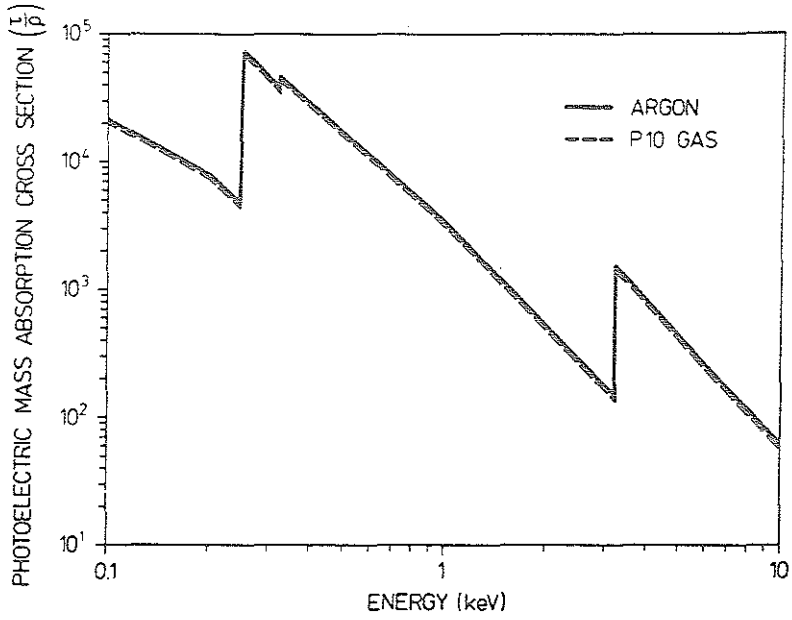

pure argon is very small ensuring that only a small percentage (< 1%) of the primary photon interactions occur in the methane.

The counter is filled with P10 counting gas (density = 1.566×10^{-3} kg/m^3) and regulated to a pressure depending on the tissue equivalent diameter to be simulated as given by equation 34 (see section 11.1)

$$d_s = \frac{p}{p_n} \cdot \rho d \qquad (34)$$

For a spherical Rossi counter of diameter 5.08 cm the pressure p necessary to simulate a unit density tissue volume of 1/um diameter is

$$p = \frac{1 \times 10^{-6} \times 0.981 \times 10^5}{1.566 \times 10^{-3} \times 5.08 \times 10^{-2}} = 1.233 \times 10^3 \text{ Pa}$$

For the cylindrical counter one could relate the simulated tissue diameter to the mean chord length, $\bar{l}$, of the measuring volume where for a cylinder of radius r, height h, $\bar{l} = 2rh/r+h$, (Bevan 1966). However, the mean chord length is then a useful concept when considering an isotropic external irradiation in which the energy depositing charged particles fully traverse the sensitive volume. Under these conditions the mean chord length acquires a definite physical significance, namely it is directly related to the mean path-length of the particles traversing the sensitive volume [43]. For the low-energy photon microdosimetric investigations of this thesis where the irradiation is anisotropic, the source of charged particles created within the sensitive volume and most of the created electrons have ranges shorter than the simulated volume diameter, so that the mean chord length becomes an unsuitable concept (see section 16).

Therefore the simulated volume diameter was related to the real diameter of the cylindrical counter used for the

[43] In this context it is used in the definition of the lineal energy y.

measurements. Given the counter inside diameter of 33 mm, the P10 gas pressure required to simulate a tissue diameter of 1 µm is, from equation (34), 1.9×10^3 Pa.

14.3 The counter operating potential

The usual operating potential of a proportional counter is in a voltage range known as the proportionality region, where the charge collected on the central wire is greater but still proportional to the initial number of ion pairs produced in the measuring volume. The proportionality region lies between two threshold potentials : a lower one, below which there is no gas multiplication i.e. where the collected charge signal is either equal or lower than the initial number of ion pairs formed [44], and an upper threshold where the measured signal is no longer proportional to the initial number of ion pairs due to the too great extension of the multiplication region around the central wire into the counting volume, i.e. there the magnitude of the gas multiplication might depend on the position where the initial ion pairs are created within the chamber. For a good linear multiplication it is necessary that the high electric field region, in which charge multiplication occurs, is limited to a region as close to the central wire as possible and that this field is precisely cylindrical.

The cylindrical counter in this work (figure 46) had a thin (0.05 mm radius) smooth and regular steel wire. Since the counter is cylindrical and the counter body well earthed, the field within the chamber is cylindrical around the central wire except at the counter ends. To avoid distortion of the electric field and hence a different gas multiplication at the ends of the counter, special field tubes have been employed. They provide both a well defined counting volume and no discontinuity in the electric field between the counting volume and the " dead " region, when applying an intermediate potential to the field tubes between that of the central wire and

[44] This is the region of operation of an ionization chamber

counter walls. The optimum setting of the potential on the field tubes is that potential which would exist at the position they occupy in an infinitely long cylinder, in their absence. The field tube voltage V_F can be calculated using equation (43) (Eickel and Booz 1977)

$$V_F = \frac{V_a \cdot \ln (r_F/b)}{\ln (a/b)} \qquad (43)$$

where V_a = the tension on the central wire,
r_F = the field tube radius,
a = the radius of the central wire,
and b = the radius of the counter.

For the fixed counter geometry the ratio V_F / V_a is a constant, (for the counter shown in figure (46) $V_F / V_a = 0.295$ i.e. the field tube voltage must be maintained at about 30% of the central wire voltage).

With the spherical Rossi counter (figure 45) a special helix electrode is employed to obtain a cylindrically uniform electric field around the central counting wire. Once again using equation (45), the percentage of the central wire potential supplied to the helix electrode in order to minimize the field distortion at the edges of the counting volume can be calculated and amounts to 25% for the particular Rossi counter concerned.

The actual potentials applied in the measurements were determined by the magnitude of the desired gas gain which is an extremely sensitive function of the operating potential. For this reason very stable high tension supplies are required if the counter resolution is not to be impaired [45]. All measurements were therefore performed with two stabilized power supplies from Canberra 205A; one for the central wire, the other for the helix electrode.

[45] A small change in the central wire potential can have a large influence on the gas gain and hence on the position of the peak in the measured spectrum.

14.4 Gas gain and counter resolution

A counter which is operated in the region of proportionality produces a signal on the central wire which is proportional to the number of initial ion pairs created in the measuring volume. The ratio of the number of electrons collected on the central wire to the number of initially created ion pairs is a measure of the gas gain. In practice the degree of gas multiplication is not constant for every initial ion pair created but because of the statistical nature of the avalanche process has a certain broadness. Therefore in practice one must refer to the mean gas gain. Although formulae have been developed relating the mean gas gain to the various counter operating parameters : voltage, gas pressure and the counter dimensions, (see Diethorn 1956, for a cylindrical counter and Campion 1971, for a spherical counter) in general their agreement with experiment in counters operated at low pressure is poor (ICRU Microdosimetry 1983, p 71). For this reason the gas gain was always measured under the conditions of counter operation employed.

To measure the gas gain under any particular experimental condition one requires at least one peak in a measured spectrum corresponding to a known energy or energy deposition. For example, the low energy photon sources available in this work provided excellant total energy peaks corresponding to the energy of the incident beam. From the channel address of the energy peak, the multi-channel analyser can be calibrated in terms of energy (keV). By dividing by the W value of the counting gas for the incident photon energy the average initial number of ion pairs n_o produced can be calculated. Thus the analyser can be calibrated in terms of the number of electrons per channel. This calibration is with reference to both a gas and electronic amplification of one. Next by applying a known pulse height from a precision pulser directly at the preamplifier input the analyser can be recalibrated with reference to the charge signal on the

counter output [46] . The ratio of the two calibration factors in terms of elementary charges then gives the magnitude of the gas gain.

The measurement of a monoenergetic X-ray beam gives not a single line spectrum but an almost Gaussian peak shape the broadness of which is determined principally by two factors. Firstly the multiplication statistics generally characterized by a parameter b of the order of about 0.6 (Knoll 1979) and secondly by the Fano factor F, usually between 0.15 - 0.25, (ICRU Report on Microdosimetry 1983) giving a measure of the statistical fluctuation in the number of initial ion pairs n_o formed from a constant energy deposition [47]. The relative variance $(\sigma_Q/Q)^2$ of an energy peak of height Q measured by a proportional counter is written as

$$(\sigma_Q / Q)^2 = \frac{1}{n_o} (F + b) \qquad (44)$$

From equation (44) it follows that the counter resolution decreases with decreasing photon energy and that the larger influence on the peak broadening results from the multiplication statistics. Therefore an increase in the gas gain produces a decrease in counter resolution. For this reason it was necessary to determine the optimum gas gain consistant with a good signal to noise ratio and high counter resolution. Table (20) gives the results of measurements for the counter resolution R, defined as the FWHM of the energy peak divided by the peak position, as a function of gas gain for the cylindrical counter (figure 46) exposed to a scandium X-ray beam of mean energy 4.125 keV.

[46] From the pulse height V the charge input Q, and hence the number of electrons, can be calculated from Q = CV where C is the preamplifier input capacitance.

[47] $\sigma^2_{n_o} = Fn_o$ where σ^2_n is the variance of the number of ion pairs created by equal amounts of energy.

Table 20

Gas gain versus counter resolution

Gas gain	Resolution
1918	22.1%
1505	21.8%
1092	20.2%
540	20.1%
394	19.8%
297	18.5%
196	19.1%
118	20.0%
70	20.5%

The results show the optimum counter resolution is achieved at a gas gain of about 300. A further reduction in the gas gain produces a further decrease in counter resolution due to the increasing influence of noise.

14.5 Counter wall effects

In icrodosimetry under counter wall effects a whole series of problems are understood which are related to different path lengths of electrons in the wall and the gas (Kellerer 1971). In the experiments performed in this thesis the particular problem of secondary electron emission resulting from Auger and photoelectron impingement on the counter wall was investigated. This effect particularly arises for electrons of very low energy (<150 eV) incident on a gas-solid interface and can result in a large fraction of the incident electron energy being re-emitted into the counting volume (Bruining 1954, Dekker 1975). This secondary electron emission can be a source of overestimation of the local energy deposition.

In this work, where electrons reaching the counter walls will be of very low energy, such secondary electron emission phenomena might be a source of spectrum distortion. Fortunately the experimental conditions are beneficial to a minimum secondary electron emission for 3 reasons :

1) The majority of those electrons produced in the counting volume have insufficient energy to reach the counter walls.

2) Due to the field tubes secondary electrons resulting from electron impingement at the counter ends will be predominantly collected on these field tubes and hence not contribute to the measured signal.

3) Metallic materials such as aluminium possess, in general, a relatively low secondary emission yield e.g. the maximum yield δ_m being 1.0 at 300 eV measured in vacuo (Dekker 1975).

To test the influence of the counter walls is not easy, since the difference in secondary emission from conducting materials is very small [48]. However, the secondary emission yield can be greatly enhanced (by a factor of 3) by roughening the counter wall surface. Energy deposition measurements were performed, under the same set of experimental conditions, for a smooth aluminium walled counter and a counter of identical dimensions with (rough) graphite coated walls. Figure 54 compares the spectra obtained for a 2 µm simulated tissue diameter and shows a slight influence of the counter wall. However, such measurements performed with simulated chamber diameters greater than the produced electron ranges and where the limit of the simulatable diameter has almost been reached, can not provide conclusive information on the magnitude of secondary emission effects but only indicate that in the experimental arangement used the effect was small.

[48] Insulating material shows a far larger secondary emission yield (up to 13 secondaries per incident electron for magnesium oxide A.J.Dekker 1975) but are impractical for use as a counter wall which must be at constant earth potential.

Figure 54

The effect of the counter wall. Energy deposition spectra measured with an aluminium walled counter and a counter with a graphite coated wall.

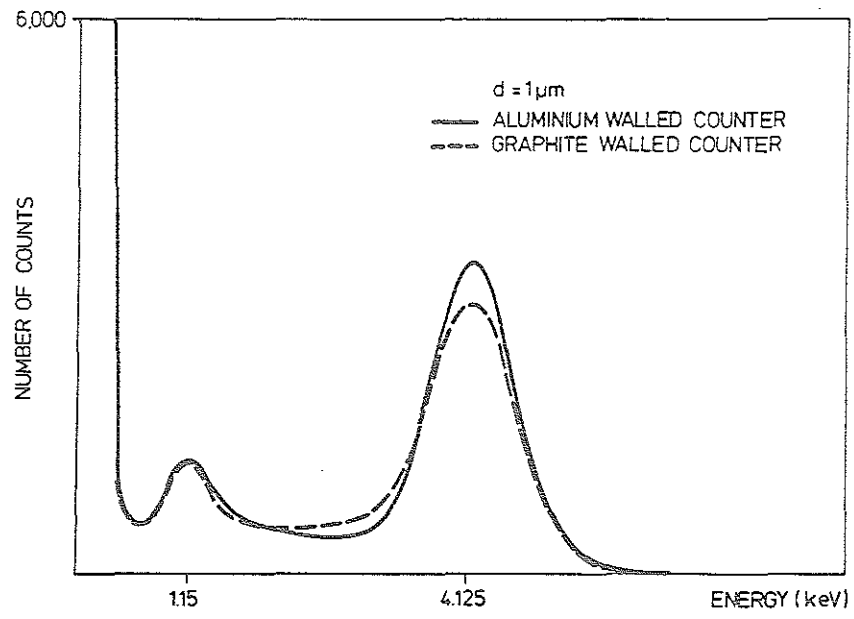

15 An anomalous Rossi counter effect

15.1 The anomalous photon energy response

Before making measurements with sensitive volumes simulating small sites, an initial series of energy spectra measurements were performed with the 2 inch P10 (90% argon - 10% methane) filled Rossi counter at a pressure of 2×10^4 Pa corresponding to a simulated diameter of 16 μm at unit density. When using an incident photon energy exceeding the K shell binding energy of the argon counting gas , a spectrum with two peaks should be measured. A full energy peak corresponding to a total conversion of the incident photon energy into electron kinetic energy, which becomes totally absorbed within the counter, and a second smaller peak, the so-called fluorescence escape peak, corresponding to photoelectric interactions in the K shell of argon followed by a KL or KM photon transition where the photon escapes the measuring volume. The energy of the latter peak is equal to the incident photon energy minus the mean KL, KM photon transition energy for argon. The ratio of the fluorescence-escape peak area to the total energy peak is given by the probability of the production of a K shell vacancy in argon, p_K, at the respective photon energy multiplied by the fluorescence yield, ω_K, for the argon K-shell. For scandium X-rays where $p_K = 0.9$ and $\omega_K = 0.12$ this area ratio should be 0.108.

The spectra as measured with the spherical Rossi counter (figure 45) are shown in figures 55 - 58 for the characteristic X-rays of titanium, scandium, potassium and chlorine respectively. Instead of the expected two peaks, two double peaks were obtained making a total of four. Numbering the peaks from right to left with 1, 2, 3, and 4 (figure 55), either the 1st and 3rd or the 2nd and 4th could energetically correspond to the total energy peak with its respective fluorescence-escape peak. Not only do the energies agree but also the areas under the matching peaks. Assuming peaks 1 and 3 to be the genuine ones (since one can not have an energy deposited greater than

the incident photon energy) then peaks 2 and 4 must be the anomalous peaks [49]. A remarkably unusual property of the peaks 2 and 4 is that they remain in constant ratio to peaks 1 and 3, irrespective of the incident photon energy. This immediately rules out the possibility that they are either foreign lines due to dirty target materials or arise from photoelectric interactions in the helix or central wire since such effect would give rise to peaks of definite energy and therefore at a constant distance from the total energy peak and not a constant ratio or energy fraction. Double peaks of this nature would result from pile-up, except that in these experiments the double peak phenomenon was independent of pulse rate from 1 count/sec to 10,000 counts/sec, thus excluding this possibility.

The spectra in figures 55 - 58 were measured at an average gas gain of approximately 1,000. It was observed that the general shape of these spectra remained unchanged i.e. the peak ratios were constant, at gas gains above 1,000 up to 5,000. However, as the gas gain was reduced, the two peaks gradually moved closer together eventually merging at very low gas gains of below 30. Hence the double peak phenomenon is gas-gain dependent, the spectrum tending to the theoretically expected one in the limit of a gas gain of 1. This is show quantitatively in figure 59 where the peak position difference CA (1) - CA (2) [50] divided by the channel address of peak 1 is plotted as a function of the gas gain. At low gas gains the double peak phenomenon disappears and at high gas gains a nearly constant ratio is reached [51].

[49] Also from the potassium and chloride targets a certain amount of Rayleigh scattered chromium X-rays from the primary beam are visible. If this peak corresponds to the characteristic X-ray energy 5.47 keV of chromium this gives a further indication of the correctness of peaks 1 and 3.

[50] CA (1) is the channel address of peak 1 and CA (2) the channel address of peak 2.

[51] This is further confirmation that the anomalous peaks are not the result of foreign lines either due to photon interactions within or outside of the counter since then the effect would not be gas-gain dependent.

Figure 55
Energy spectrum for titanium X-rays (4.55 keV), measured with a 2 inch spherical Rossi counter showing double peaks.

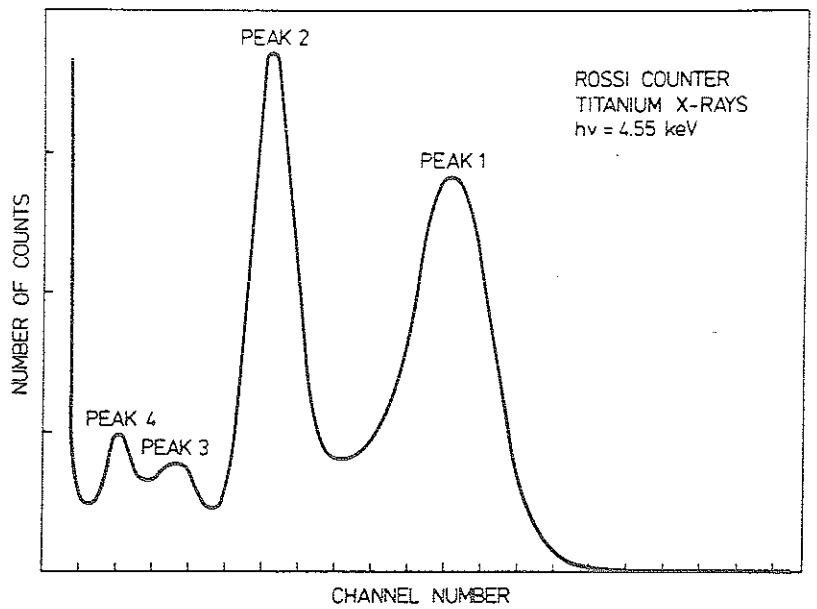

Figure 56
Energy spectrum for scandium X-rays (4.125 keV), measured with a 2 inch spherical Rossi counter showing double peaks.

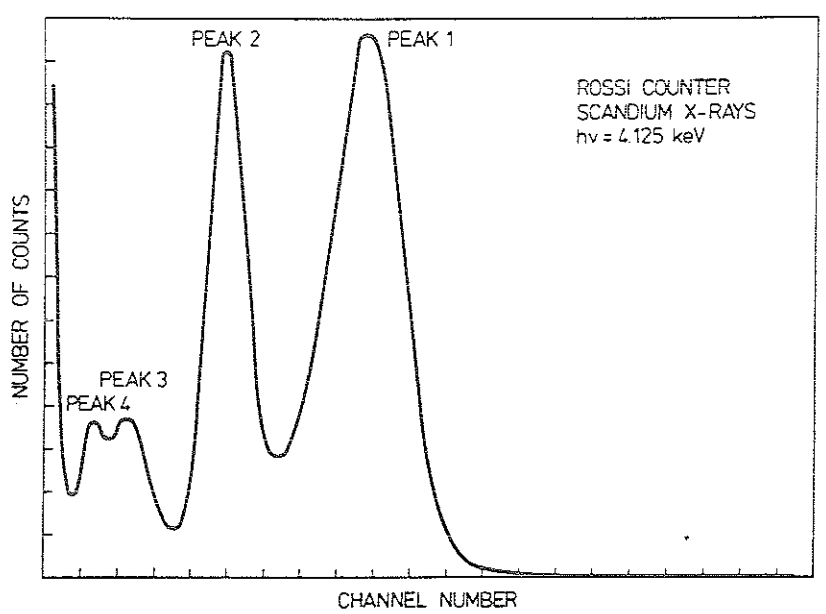

Figure 57
Energy spectrum for potassium X-rays (3.31 keV), measured with a 2 inch spherical Rossi counter showing a double peak.

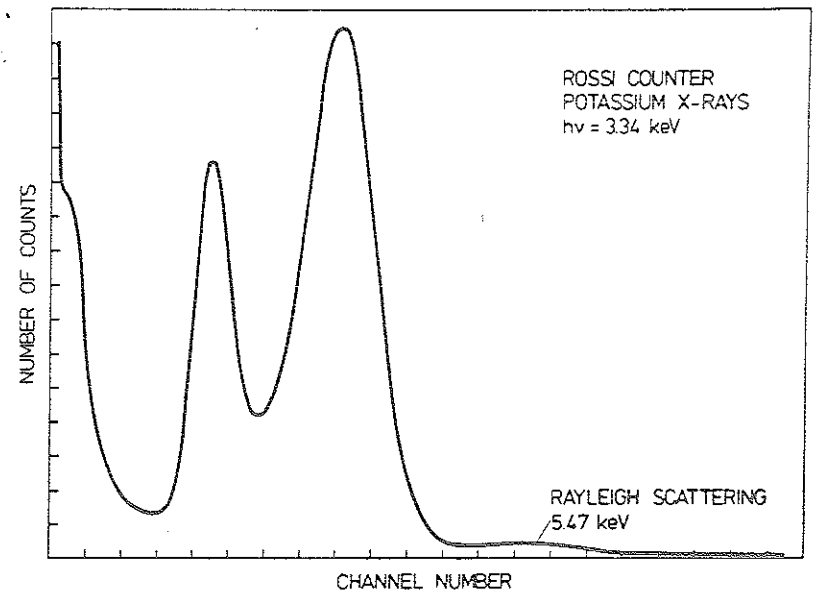

Figure 58
Energy spectrum for chlorine X-rays (2.63 keV), measured with a 2 inch spherical Rossi counter showing a double peak.

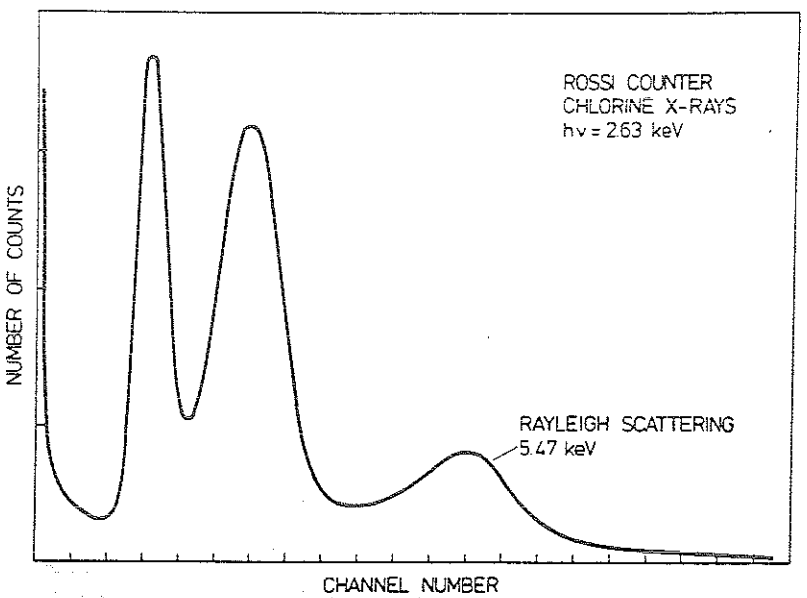

Figure 59
Peak separation between the double peaks relative to the upper peak position as a function of the gas gain.

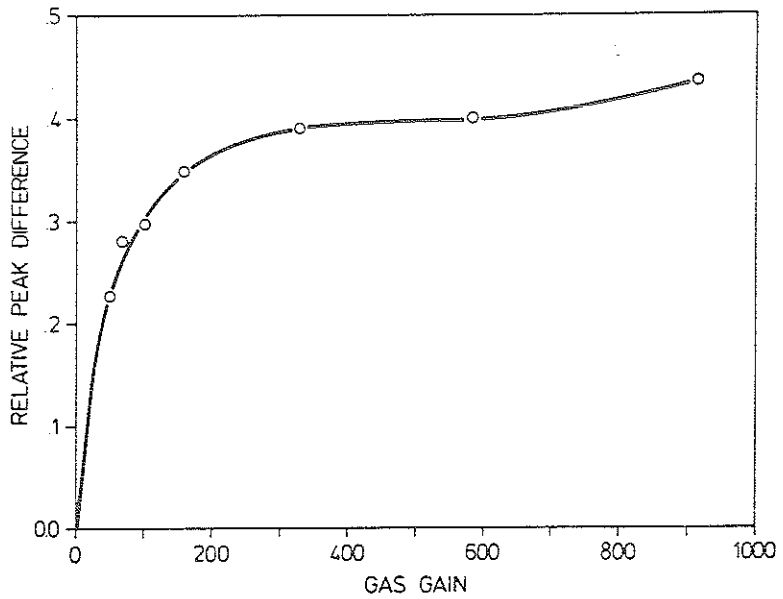

Figure 60
Energy spectrum for scandium X-rays (4.125 keV) measured with the Rossi counter with zero potential on the helix electrode.

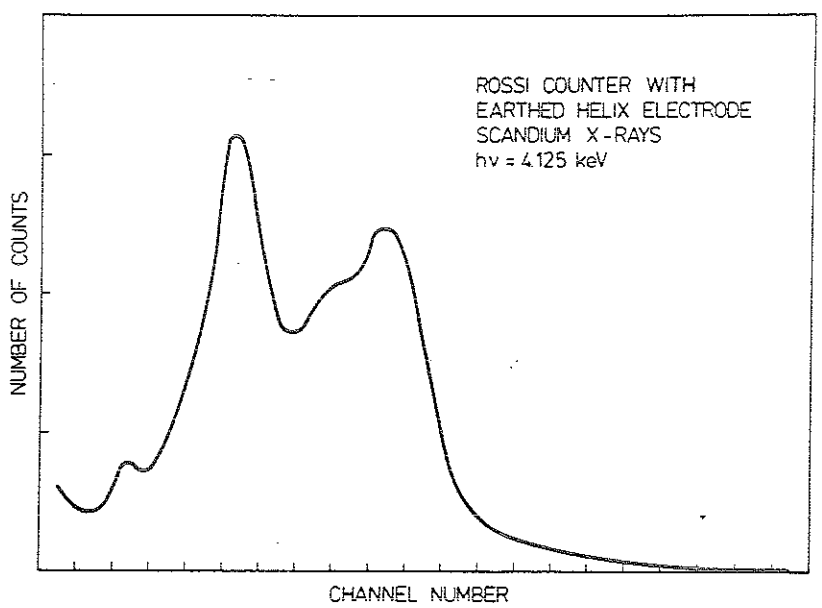

to an incorrect setting of the helix potential (see section 18.3). However, it could be shown that this was not the case. The double-peak effect was hardly affected by the helix potential (except for a small change in the gas gain), i.e. no helix potential could be found to give anything like the expected counter response in a range of helix potentials from 50% of the central wire voltage to 0%. In the latter case (figure 60) the helix electrode was well earthed so that any charge build-up on the helix could be rapidly neutralized. Apart from a worsening of the counter resolution the anomalous peak phenomenon remained.

The properties of the anomalous peaks still, however, tend to suggest that they result from a charge effect, probably around the helix electrode, which somehow distorts the electric field in the vicinity of the central counting wire thus giving rise to two discrete gas gain regions. This hypothesis was further investigated by performing a sequence of test experiments designed to reveal more about the cause of the double peaks.

15.2 Further investigations into double-peak phenomenon

To test whether the anomalous peaks are the result of the helix electrode a simple cylindrical counter was constructed with a single central wire electrode and measurements performed under the same set of experimental conditions : geometry, counter window, gas pressure, gas gain, scandium X-ray beam etc., as with the Rossi counter. Figure 61 compares the spectra obtained with the Rossi and cylindrical counters and shows that the double peaks i.e. peaks 2 and 4 are absent.

To confirm with certainty that the presence of the helix electrode is responsible for the anomaly, two further decisive experiments were carried out. First the helix electrode was removed from the Rossi counter and second, the Rossi-counter helix was inserted into the cylindrical counter. Figure 62 shows a spectrum obtained with the Rossi

Figure 61
Comparison of the scandium energy spectra as measured with the Rossi counter, (helix potential applied) and with a self constructed cylindrical counter.

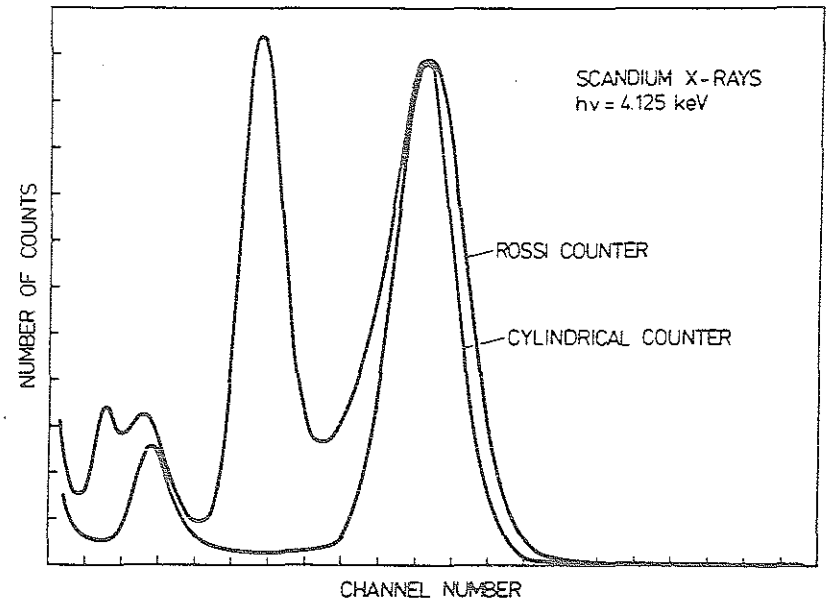

Figure 62
Scandium energy spectrum measured with a spherical Rossi counter, (figure 45) with the helix electrode removed.

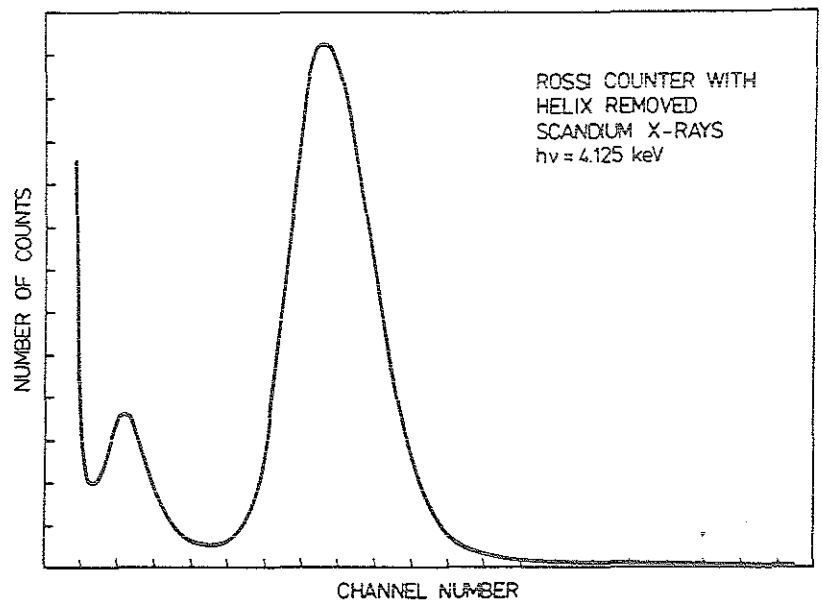

Figure 63
Scandium energy spectrum measured with the cylindrical counter, (figure 46) with an inbuilt helix electrode, demonstrating that the anomalous peak results from the presence of the helix electrode.

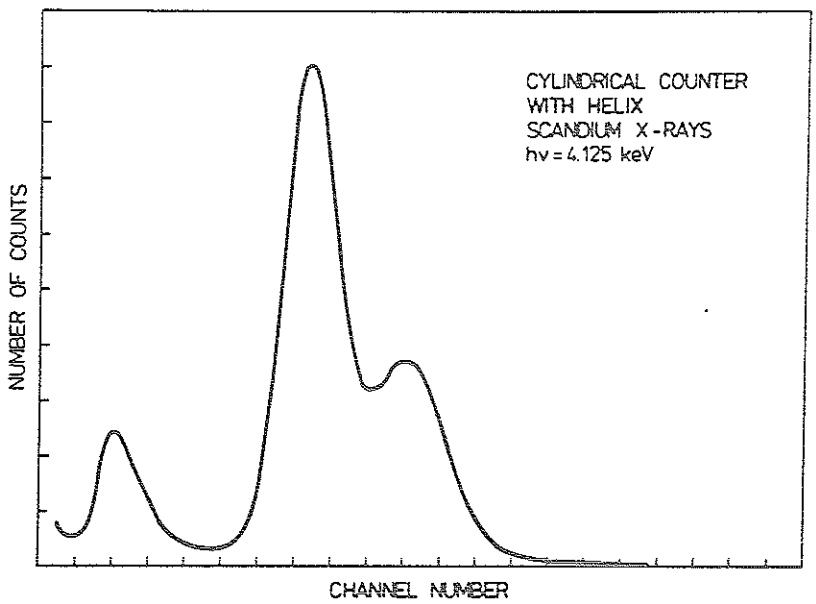

counter without helix, and confirms the hypothesis about the helix since the double peaks are no longer present [52]. The second confirmation comes from the measurement performed with the cylindrical counter with a helix (figure 63) where the anomalous peaks are now suddenly present.

The spectra measured with the cylindrical counter with helix differ from those measured with the Rossi counter in two respects : the relative intensities of the peaks are different and the distance between the peaks 1 and 2 are smaller (the asymptotic value for $[CN(1) - CN(2)] / CN(1)$ depicted in figure 59 for the Rossi counter measurements, was only 0.25 at a gas gain of 2,000, i.e. about half that obtained with the Rossi counter. This problem was not further investigated and thus the reason for this difference is not known. However, it could be related to the different helix geometries (pitch, diameter) which were 23 turns in 67 mm for the cylindrical counter and 23 turns in 50.8 mm for the Rossi counter. Such sensitivity to the helix geometry further suggests the possibility of space charge effects at the multiplication region.

Such space charge effects were reported by Campion, 1971, when using tissue-equivalent gas, methane [53] and ethylene counting gases which contained 1% of water vapour for low energy photon measurements. Indeed his spectra show some similarity to those reported here. However, Campion did not observe the effect when using methane quenched argon. In the experiments reported here the chamber was evacuated to 10^{-3} Pa for up to 3 days and then filled with highly pure P10 gas in order to especially advoid water vapour entering the chamber. However, since the double

[52] The bad resolution is the result of counter end effects since in a spherical counter the electric field is no longer cylindrically uniform around the central wire. It is for this reason that the helix electrode is necessary.

[53] Test measurements were also performed with methane gas in this work where the same double peak phenomenon arose even in the absence of such a high proportion of water vapour.

peak vanished upon removal of the helix electrode it can be concluded that the anomalous peaks do not originate from any gas impurities such as water vapour.

Although no definite conclusions can be drawn about the cause of the spurious double peaks when proportional counters are operated with helical grid electrodes, it is not unlikely that a region of a space charge is formed in the locality of the helix which distorts the electric field thus creating two different gas gain regions, perhaps by reducing the number of electrons produced at later stages in the avalanche. Such effects, known generally under the name of self-induced space charge effects, have been reported in the literature (see Knoll 1979 and Hendricks 1969). Such space-charge effects are sensitive to gas gain and counter geometry but independent of count rate which is in agreement with the discussed experimental findings.

15.3 Consequences for Microdosimetry

It is unusual that in such a well established measurement technique as microdosimetry that anomalous effects have remained unnoticed or unreported. Possibly, such problems have not arisen before because Rossi counters have so far been used exclusively for the measurement of energy-deposition spectra, i.e. measurements in which only a fraction of the incident particle energy is deposited in the sensitive volume. Under such conditions one obtains broad spectra of energy deposition and not sharp high-resolution peaks and therefore such anomalies can go unnoticed (figure 64 gives an example of an energy-deposition spectrum measured with the same Rossi counter with helix simulating a 1/um tissue equivalent diameter). Further, because of the common representation of such spectra as yd(y) versus log y, the presence of any space-charge effect becomes even more disguised so that any double peak either vanishes in the main peak or becomes visible only as a shoulder on the left (lower energy) side of that peak.

The results presented in this section represent experimental experiences of the author over a period of two years of systematic investigations in low-energy photon experimental microdosimetry. They should give incentive to scrutinize previous measurements performed with similar counters on energy-deposition spectra of low-energy photons and on the validity of calibration performed with low-energy photons. Further, special care should be taken to examine Rossi counters thoroughly to investigate the influence of this possible space-charge effect for energy deposition above the keV-range. Finally it is suggested that for future investigations in microdosimetry the use of a helix be advoided.

Figure 64
Energy deposition spectrum for 4.125 keV X-rays incident on a 2 inch Rossi counter (figure 45) filled with argon at a pressure simulating a tissue equivalent diameter of 1 µm.

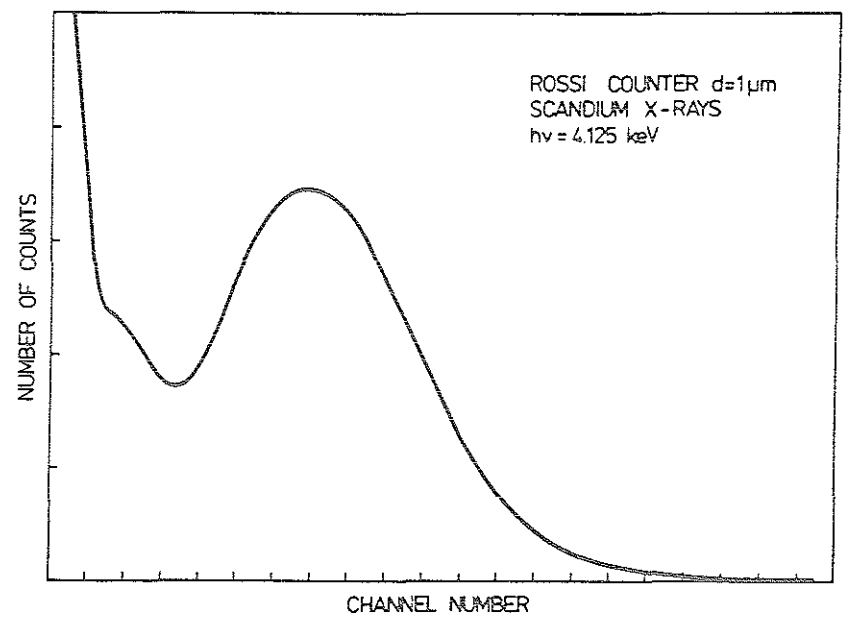

16 Path length distributions

An important factor determining the shape of an energy-deposition spectrum for particles of constant LET is the path-length distribution of the particles in the counting volume. Therefore energy-deposition spectra and their derived means depend on the geometry of the counter. In the past, microdosimetric measurements have mostly been performed with spherical counters but cylindrical counters have also been used. Also measurements have almost exclusively been performed with radiations such as neutrons or gamma rays producing secondary charged particles almost exclusively from the counter walls energetic enough to fully traverse the sensitive measuring volume. In such cases, assuming the secondary particle to travel straight lines isotropically across the counter, the path-length distribution of the energy depositing particles can be replaced by their chord-length distribution in the measuring volume. For a spherical cavity the chord length distribution is triangular in shape, (see Rossi 1968) and for a cylindrical counter the distribution contains sharp cusp-like peaks which vary according to the ratio of the cylinder height to diameter (for a variety of cylinder geometries, see Birkoff et al 1970, Hogeweg 1978).

In the special experimental geometry reported here, the secondary-energy depositing charged particles, the photoelectron and Auger electrons, are induced by photoelectric interactions along a diameter of the counting volume. It was therefore necessary to calculate the electron path-length distributions under the geometry employed in the measurement. For this purpose a special Monte-Carlo programme was developed simulating the electron path produced by 10,000 photoelectric interactions along the central diameter (figure 65) of a cylindrical counting volume [54].

[54] Under the same irradiation geometry as the experimental energy deposition measurements reported in section .

The calculation was based on 3 principal assumptions :

1) the probability of photon interactions is constant across the counter diameter, i.e. there is no attenuation of the photon beam,

2) the electrons generated in the counter travel in straight-line path between their point of origin and the counter wall,

3) the direction of emission of all electrons is isotropic with respect to the incident photon beam [55] .

The method of calculation proceeds as follows. First an interaction point is chosen at random along the chamber diameter, (random number generator GGUW - IBM Fortran library). Each interaction point is the source of a photoelectron and a series of Auger electrons, the number and energies of which depend on the transition pathways in the vacancy cascade during atomic de-excitation. From the work on simulated vacancy cascades following photoelectric interactions in argon, discussed in Part II, section 10, individual electron-energy spectra were written on tape for 10,000 individual interactions at the photon energies of interest here. This data could be employed by reading in successively one set of electron energies for each interaction point. For each electron of energy E the range was calculated using the range formula of Iskef and Watt 1982 [56].

$$\ln\left(\frac{Z}{A} \cdot R_{ex}\right) = -4.5467 + 0.31104\ \ln(E) + 0.07773\ (\ln E)^2 \qquad (45)$$

where R_{ex} is the extrapolated electron range in $\mu g/cm^2$

[55] This is true for Auger emission but not for the photoelectrons which, at such low photon energies, are emitted preferentially at 90° to the incident photon beam.

[56] The authors claim this range formula to be valid for electrons in the energy range from 20 eV to 10 keV with a standard deviation of the mean of around 25%.

Figure 65
Irradiation geometry for the cylindrical counter measurements.

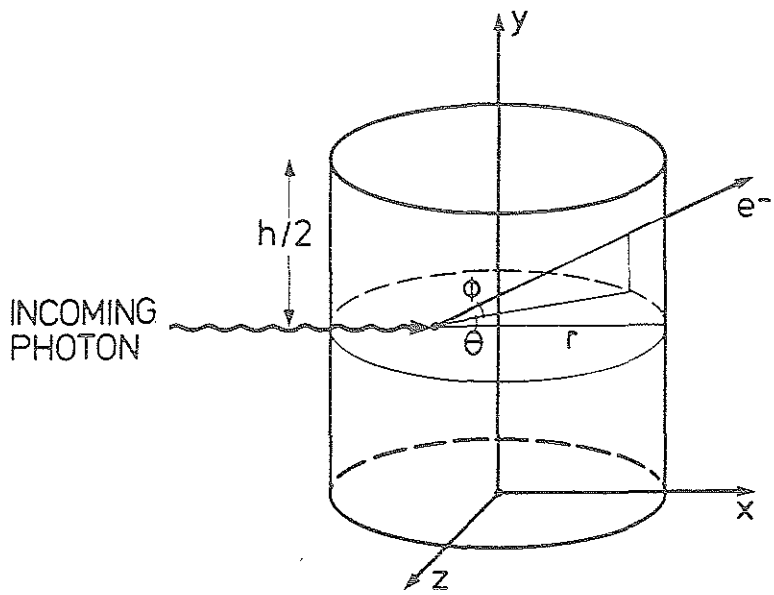

and Z/A the atomic number to mass ratio for the stopping medium.

Next for each individual electron a random isotropic direction of propagation is chosen using the method described by Sobol 1974. This method entails the generation of two random numbers R_1 and R_2 to fix the angles $\emptyset$ in the xz plane and $\emptyset$ in the xy plane (figure 65), the angles being determined by equations (46) and (47) [57].

$$\theta = 2\pi . R_1 \qquad (46)$$

$$\cos \emptyset = 1 - 2.R_2 \qquad (47)$$

Given the coordinates of the interaction point and the angles θ and $\emptyset$, the distance the electron would have to travel to the cylinder wall can be calculated in which consideration is taken of the cylinder ends. If the electron range is sufficient to carry the electron to the cylinder wall, the electron path length in the sensitive volume is equal to the distance the electron travels to the counter wall, otherwise it is equal to the electron range. In this way the path-length distribution of the individual electrons in the cylindrical counting volume is obtained.

If the path-length distribution of the individual electrons is plotted for cylinder diameters greater than 0.5 μm, the distribution is dominated by the large number of short-range, low-energy Auger and Coster-Kronig electrons emitted producing a series of peaks corresponding to the most frequently occuring electron ranges. Also the electron path-length distribution obtained is no longer related to the shape of the energy deposition spectrum as would be measured with a proportional counter, where electrons resulting from the same photoelectric interaction are not independently resolvable in time. Rather, the pattern

[57] Proof that these equations give an isotropic choice of direction is in Sobol 1974.

of energy deposition measured in the practical situation is more closely correlated to the total electron path length per photoelectric interaction. For this reason the electron path lengths produced by electrons resulting from a single interaction were summed and a distribution of the total electron path lengths per interaction plotted.

Figures 66 and 67 show the electron path length distributions per interaction for the incident photon energies 3.34 keV (potassium $K_{\alpha,\beta}$) and 2.63 keV (chlorine $K_{\alpha,\beta}$) X-rays respectively for cylinder diameters : 8/um, 1/um, 0.5/um and 0.1/um. On the abscissa the electron path length per interaction is plotted as a fraction of the cylinder diameter d and on the ordinate the relative path length probability per bin width of d/100.

For the volume diameters 8/um and 1/um, at these photon energies, the electron ranges are shorter than the cylinder dimensions i.e. practically all electrons become fully absorbed within a distance a fraction of the counter diameter. This results in sharp peaks in the distribution corresponding to the total fractional electron range per interaction in the counter. For the potassium X-rays a second peak arises due to fluorescence escape at a position determined by the total electron range minus that of the missing K Auger electron.

At volume diameters of 0.5/um and below, the ranges of the most energetic electrons (the K Auger electron for the potassium x-rays and the photoelectron for the chlorine X-ray energy) become comparable or greater than the cavity dimensions and the probability of electron impingement with the counter walls therefore increases. That determines the distribution form at these counter diameters is primarily the path length of the most energetic electron [58].

[58] On average 4 electrons are emitted per photoelectric interaction induced by a potassium X-ray photon. The K shell Auger electron from argon essentially determines the shape of the path length distribution, the other low energy electrons contributing only a constant modulation to the distribution so long as their ranges are small compared to the counter dimensions.

Figure 66
Calculated total straight line electron path length contributions for electrons released following 3.34 keV X-ray induced photoelectric interactions in an argon filled cylindrical counting volume simulating 0.1 /um, 0.5 /um, 1 /um and 8 /um tissue equivalent diameters.

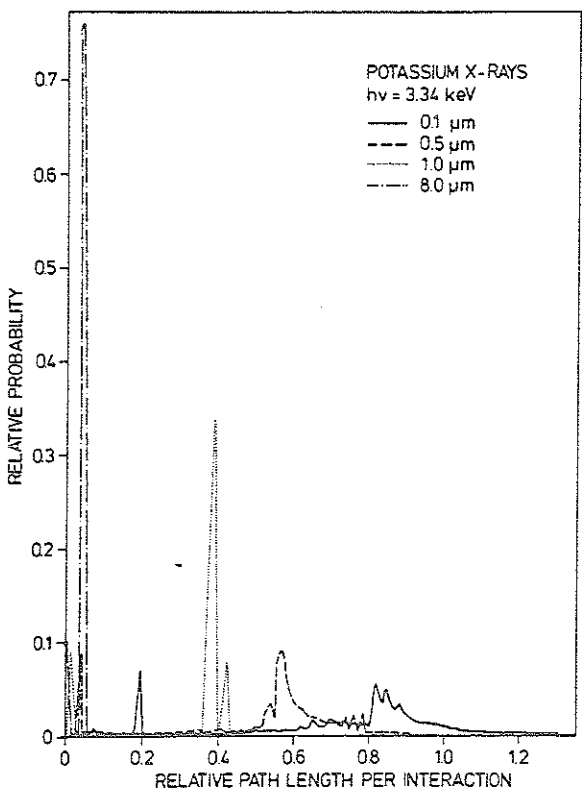

Figure 67
Calculated total straight line electron path length distributions for electrons released following 2.63 keV X-ray induced photoelectric interactions in an argon filled cylindrical counting volume simulating 0.1 /um, 0.5 /um, 1 /um and 8 /um tissue equivalent diameters.

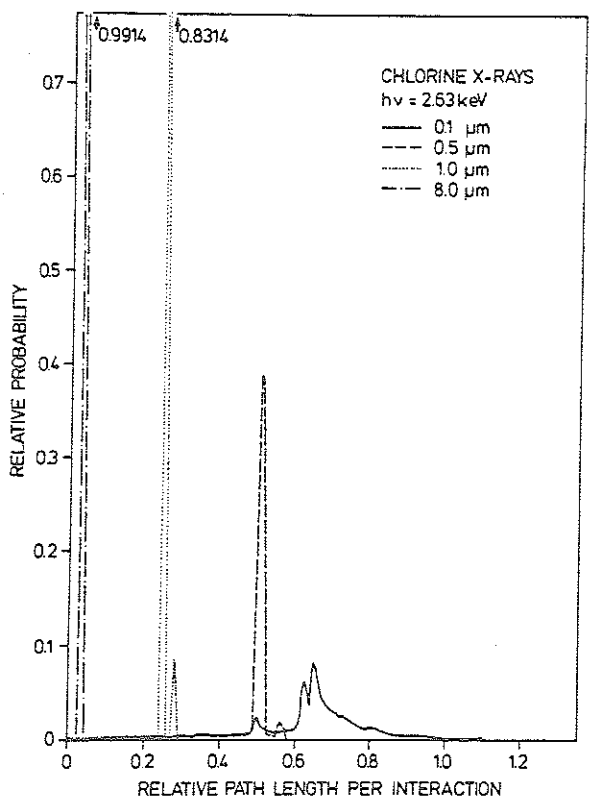

Electrons incident with the cylinder body give rise to a flat broad distribution stretching from zero to values slightly greater than the cylinder diameter. The peak at the upper end of the distribution results from electron incidence with the cylinder ends (where there is a higher density of paths of similar length). The sharp rise in the lower side of the peak is from electrons striking perpendicular to the cylinder ends. The more gradual falling upper side results from electrons emitted almost perpendicular to the photon beam but at ever decreasing angles giving rise to increasingly longer electron path lengths but with continually decreasing probability, as the solid angle between the interaction points along the photon path and the cylinder ends becomes increasingly smaller. The position of the peak is higher than the cylinder half height, h/2, by an amount corresponding to the total path length per interaction of the accompanying lower energy electrons.

The smaller the cylinder diameter the broader and more complex the distribution due to the continually increasing influence of lower-energy Auger electrons which no longer simply contribute a linear modulation to the total path length distribution. This influence starts to be visible at the 0.1 µm volume diameter.

A brief final comment requires mention regarding the choice of irradiation geometry applied in the measurements and for which the path length calculations, the subject of this section, were performed. Since at low photon energies an isotropic exposure of the chamber is not possible a thin X-ray beam geometry was employed, the photons entering the counter through a thin mylar window and traversing a diameter of the counter, whereby the problem arises that at low counter diameters (< 1 µm) the electron path length distribution, and hence the energy deposition spectrum, is dependent on the position where the photon beam traverses the sensitive volume. From the path length calculations it could be shown that, because the peaks in the distribution result from electron incidence with the cylinder end pieces, a distribution containing a single peak is only

then obtained when the photon beam traverses central and perpendicular to the cylinder axis where all secondary electrons have their origin at equal distances between the two cylinder ends. When this condition is not fulfilled and photo- and Auger electrons are produced at points other than on the central diameter of the counter, then an extremely complicated electron path length distribution results containing two peaks, corresponding to the differing electron path lengths to the two cylinder ends. The result of such an electron path length distribution would be to produce a far more complicated energy deposition spectrum and add to the difficulties in counter calibration.

17 Energy deposition spectra for low energy photons

17.1 Measurement variables

In this section energy-deposition spectra are presented for measurements performed with an argon filled cylindrical proportional counter irradiated with photons of energies just above (3.34 keV potassium $K_{\alpha,\beta}$) and just below (2.63 keV chlorine $K_{\alpha,\beta}$) the K edge of argon (3.2 keV). A further secondary target, scandium, was used to give a supplementary photon energy (4.125 keV) above the K edge of argon. For excitation of the secondary-target fluorescence radiation, both a chromium and molybdenum X-ray tube were employed. With the molybdenum primary beam additional energy-deposition spectra were measured using a lithium bromide secondary target giving X-rays of energy 12.087 keV producing somewhat higher energy photoelectrons in the measuring chamber.

Energy-deposition spectra were measured at five tissue equivalent volume diameters : 8 /um, 4 /um, 2 /um, 1 /um and 0.5 /um whereby the simulated diameter is referred to the actual diameter of the cylindrical counting volume (section 14.2). The primary chamber geometry used in this work was a cylinder of equal diameter and height, i.e. d = h, where the photon beam traverses central and perpendicular to the cylinder axis (see figure 65). However , further spectra were measured for the cylinder geometry h = 6d i.e. a long cylinder, where at the simulated volume diameters of interest here, electrons have insufficient energy to reach the cylinder ends.

The spectra shown in this work are plotted as direct energy deposition, ϵ , on the abscissa against number of counts on the ordinate on a linear-linear scale. At the 8 /um simulated tissue diameter the measured spectra represent, at all photon energies used here, energy spectra. However, at increasingly smaller simulation diameters the main energy peak will become less and less suitable for calibration purposes since some of the more energetic electrons will lose energy to the counter walls. The lowest

energy well resolved peak above the noise level obtained was the argon fluorescence escape peak from the scandium line, i.e. 4.125 - 2.975 = 1.15 keV. It was this peak together with the channel zero baseline which were used to calibrate the energy scale. For each simulated diameter the scandium spectrum was used not only for calibration but also for spectrum normalization.

For the scandium spectrum a region of interest was defined, with a lower level set at the minimum between the fluorescence escape peak and noise, and an upper level set at the minimum between the scandium main peak and the Rayleigh scattered chromium peak. The integral number of counts within this region of interest was used as the criterian for the collection time for each measurement, i.e. spectra were measured until the number of counts in the region of interest matched a predetermined integral amount. This meant that the area under all spectra, (except those measured with the bromine X-rays) were identical in the region of interest advoiding the necessity of a separate numerical normalization. With the bromide target the gain of the amplifier was reduced by three, (checked with a precision pulser) and so reducing the calibration in keV/channel also by three. The region of interest designated for the bromine spectrum differed from the other measurements and hence a separate normalization was carried out.

17.2 Energy deposition spectra and their mean values

The first set of energy deposition spectra are presented in figure 68 - 70 measured with a chromium X-ray tube with potassium and chlorine as secondary targets, and at tissue equivalent diameters of 8 µm, 2 µm, 1 µm and 0.5 µm [59].

At the 8 µm diameter, corresponding approximately to the average cell nuclear diameter, the spectra of energy

[59] A measurement performed at 4 µm equivalent diameter proved essentially the same as 8 µm and therefore was omitted to avoid additional complexity of the figures.

deposition in the counter are equivalent to energy spectra. Therefore the measured spectrum consists of a total energy peak equal to the energy of the incident photon, and for photon energies above the K edge of argon there is a second peak corresponding to fluorescence escape from the argon counting gas, equal to the incident photon energy minus the average photon transition energy for argon. For the potassium X-rays the fluorescence escape peak is not visible, its energy (365 eV) being too low to be discriminated from the noise level.

As the diameter of the simulated volume is reduced, the magnitude of the total energy peak decreases, as increasingly more and more electron energy is deposited outside of the counter sensitive volume. This decrease in the total energy peak intensity is complimented by an increase in the number of energy deposition events below the incident photon energy.

The spectra in figure 68 - 70 have equal areas between the noise level and the elastic scattering peak, so that a direct intercomparison of all spectra is possible. After calibration the total energy deposited in the chamber at any particular volume diameter is obtained by integrating the spectrum over the region of interest. The mean energy deposition per event $\bar{\epsilon}_F$ is then the total energy deposited divided by the total number of energy deposition events in this region. In table 21 are given the values of $\bar{\epsilon}_F$ for a chromium primary beam incident on the secondary targets : scandium, potassium and chlorine in tissue equivalent diameters (cylindrical counter d = h) from 8 /um - 0.5 /um.

The same series of measurements with the same secondary targets in tissue equivalent diameters from 8 /um - 1 /um were repeated using molybdenum in place of the chromium X-ray tube. The major differences with the molybdenum tube measurements are the higher operating tube potential producing a more intense primary beam, more bremsstrahlung and the molybdenum characteristic photon energy (17.8 keV) in place of the chromium line. This leads to a slight depreciation in the secondary beam

Figure 68
Energy deposition spectra for scandium X-rays, (4.125 keV) measured in a cylindrical counter for tissue equivalent diameters: 8 /um, 2 /um, 1 /um and 0.5 /um.

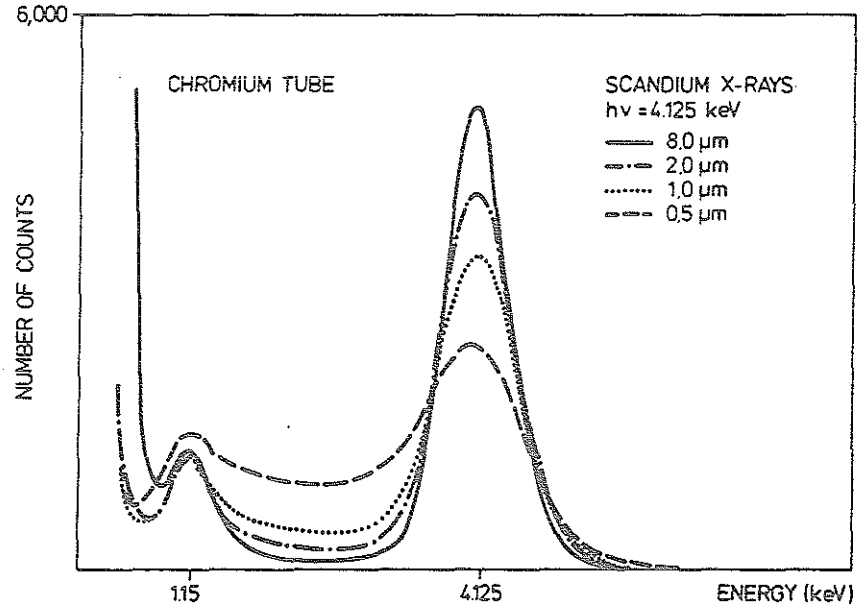

Figure 69
Energy deposition spectra for potassium X-rays, (3.34 keV) measured in a cylindrical counter for tissue equivalent diameters: 8 /um, 2 /um, 1 /um and 0.5 /um.

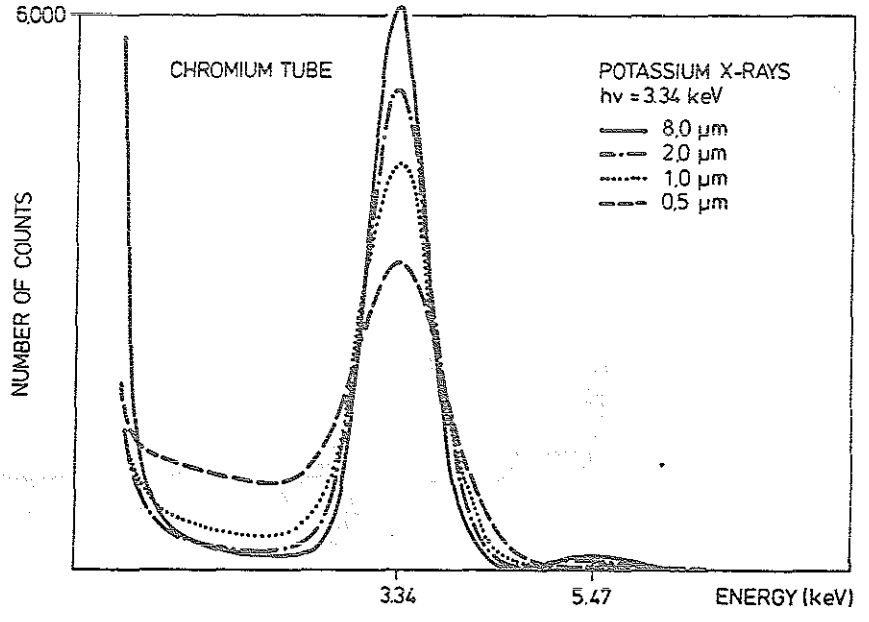

Figure 70
Energy deposition spectra for chlorine X-rays, (2.63 keV) measured in a cylindrical counter for tissue equivalent diameters: 8 /um, 2 /um, 1 /um and 0.5 /um.

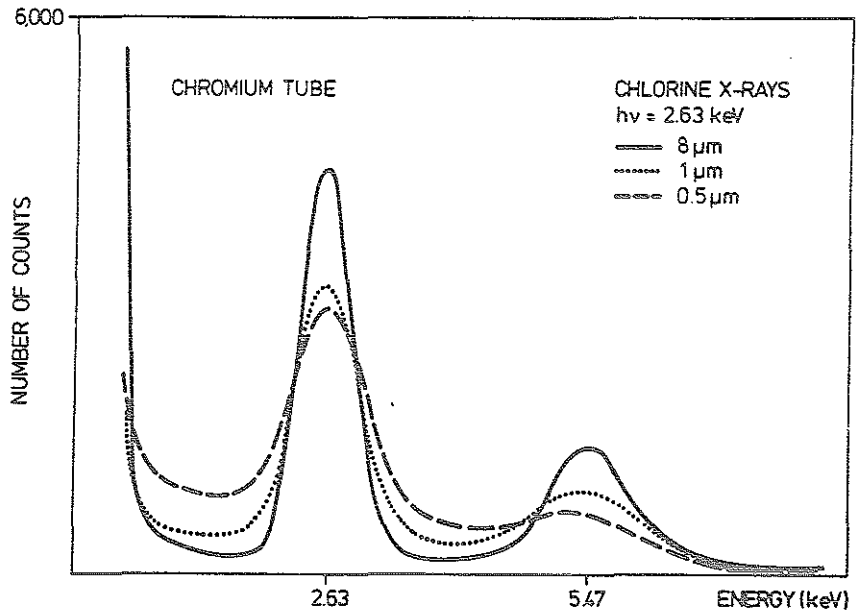

Figure 71
Energy deposition spectra for the scandium, potassium and chlorine X-rays produced by a molybdenum tube, (for comparison with the 8 /um measurements with X-rays induced by the chromium tube).

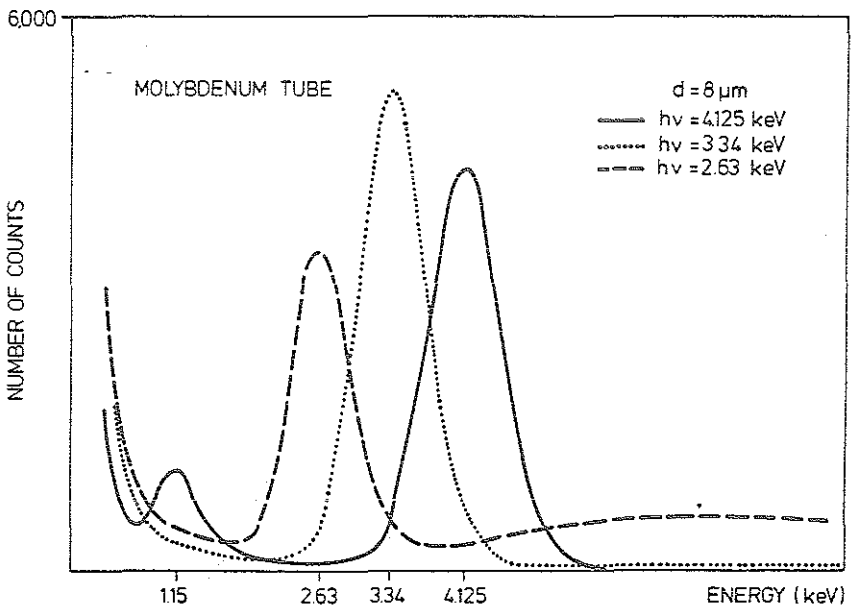

monochromaticity, however gave the opportunity to observe both the reliability of previous measurements with the chromium tube as well as allowing an additional photon energy of higher energy (the $K_{\alpha,\beta}$ photons of bromine [60] from a lithium bromide target) to be added to the measurements.

Table 21
Mean energy deposition $\bar{\epsilon}_F$ for low energy photons induced by a chromium X-ray tube, as measured by a cylindrical counter of dimensions d = h.

d(/um)	$\bar{\epsilon}_F$(keV)		
Photon energy(keV)	4.125(Sc)	3.34(K)	2.63(Cl)
8	3.680	3.214	2.587
4	3.620	3.212	2.587
2	3.578	3.201	2.587
1	3.462	3.091	2.556
0.5	3.076	2.852	2.489

The energy spectra as obtained for the scandium, potassium and chlorine secondary targets with the molybdenum tube are given at the 8/um tissue equivalent diameter in figure 71 [61]. The different primary beam characteristics give rise to a more polychromatic scattering off the secondary target most visible for the chlorine target. The values for the mean energy deposition as obtained with the molybdenum tube measurements are given in table 27 and are generally in better than 30 eV agreement to those obtained with the chromium tube. Also in table 27 are the $\bar{\epsilon}_F$ values from measurements with the higher energy bromine characteristic X-rays, the spectra for which are shown in figure 72 for tissue equivalent counter diameters : 8/um, 4/um, 2/um and 1/um. At the 8/um diameter a sharp total energy

60 The yield of bromine X-rays one can obtain with a chromium tube is very small since these can only be produced by the bremsstrahlung spectrum.

61 Figure 71 has been plotted on the same energy scale and with the same integral number of counts in the region of interest as the spectra in figures 68 - 70. They are therefore also directly comparable.

peak occurs at the bromine fluorescent photon energy of 12.087 keV. At 9.11 keV is the fluorescence escape peak (from the argon counting gas) sitting on a background of energy deposition events between 0 - 12 keV. As the tissue equivalent counter diameter is reduced the intensity of the total energy peak rapidly declines and the whole spectrum shifts to lower values of energy deposition a new peak arising at a value corresponding to the most probable energy deposition per interaction.

Table 22
Mean energy deposition $\bar{\epsilon}_F$ for low energy photons induced by a molybdenum X-ray tube.

d(μm)	$\bar{\epsilon}_F$(keV)			
Photon energy(keV) and target	4.125(Sc)	3.34(K)	2.63(Cl)	12.087(Br)
8	3.723	3.228	2.564	10.061
4	3.591	3.208	2.558	8.383
2	3.561	3.182	2.535	6.292
1	3.472	3.102	2.533	4.830

Finally a series of energy deposition measurements were performed in a cylindrical counter of sensitive volume dimensions h = 6d (cylinder height is 6 times its diameter). Of particular interest were the 1 um and 2 um volume diameters to see if any significant charge in the mean energy deposition occurred where electrons emitted perpendicular to the direction of the photon beam traversal would be in all cases fully absorbed in the sensitive volume. The spectra obtained at a 1 μm tissue equivalent cylinder diameter with photons energies 4.125 keV, 3.34 keV and 2.63 keV (the secondary targets excited with a chromium primary tube) are shown in figure 73. The $\bar{\epsilon}_F$ values for the counter diameters 1 μm and 2 μm are given in table 23.

The results show values of $\bar{\epsilon}_F$ comparable to those measured with the right cylindrical counter (table 21), the differences probably being the result of experimental inaccuracies rather than genuine differences in the amount of energy deposition.

Figure 72
Energy deposition spectra for bromine X-rays, (12.087 keV) in a cylindrical counter at the tissue equivalent diameters; 8/um, 4/um, 2/um and 1/um.

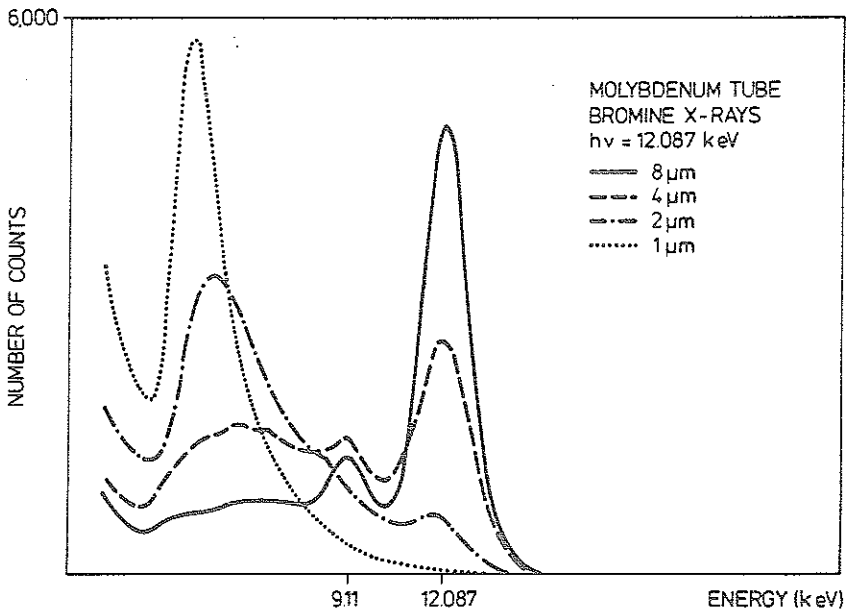

Figure 73
Energy deposition spectra for 4.125 keV, 3.34 keV and 2.63 keV X-rays measured in a cylindrical counter of dimensions; height = 6 X diameter where the tissue equivalent diameter is 1/um.

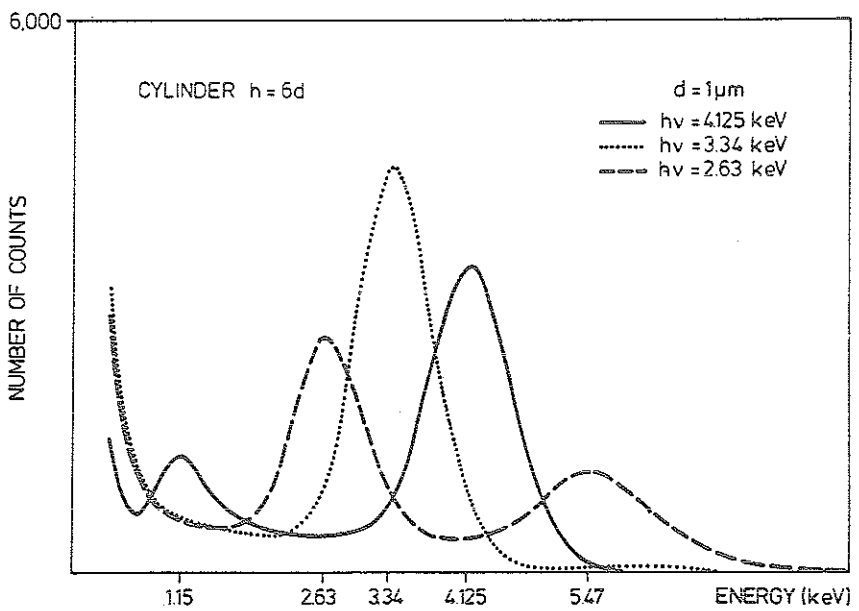

Table 23

Mean energy deposition $\bar{\epsilon}_F$ for low energy photons measured in a cylindrical counter of dimensions h = 6d

d(μm)	$\bar{\epsilon}_F$(keV)		
Photon energy (keV)	4.125(Sc)	3.34(K)	2.63(Cl)
2	3.561	3.192	2.589
1	3.464	3.080	2.549

The close agreement in all the results presented here tend to suggest that, at the cellular dimensions simulated in the counter, almost all the incident photon energy transformed to electron kinetic energy in the sensitive volume becomes absorbed there i.e. at least for photon energies below 5 keV. Any considerable change in the pattern of energy deposition would be expected, when measureable, first at tissue equivalent counter diameters less than 0.5 μm.

18 Summary and conclusions

It was the aim of this thesis to make a broad contribution to the understanding of the microdosimetry of Auger emitters.

Part I was concerned with the energy deposition processes resulting from incorporated radionuclide decay in which the emission of low energy Auger electrons form a predominant contribution to the high radiotoxicity. The radiobiological effectiveness of an incorporated radionuclide will depend firstly on the local pattern of energy deposition around the decaying radionuclide and secondly on the degree of overlap of this energy deposition pattern with the sensitive areas of the biological system. Part I of this thesis addresses in particular the first of these.

Four radionuclides of current relevance to radiation biology and medicine were investigated : ^{123}I, ^{125}I, ^{55}Fe and ^{64}Cu. Certainly all four of these radionuclides when incorporated in the cell nucleus deposit sufficient energy in the nucleus to produce a DNA double strand break (DSB). However, what is decisive is the concentration of the energy deposited at the critical sites.

For ^{123}I and ^{125}I, which can be incorporated directly into the DNA, the concentration of energy deposited within a site size of 2 nm (the distance between the 2 strands of the DNA) is high; calculations performed here show approx. 123 eV for ^{123}I and 211 eV for ^{125}I per decay. For ^{125}I this is probably sufficient for a DSB since from experiment it is known that ^{125}I incorporated into the DNA in the form $^{125}IUdR$ produces about one DSB per decay. For $^{123}IUdR$ incorporation no figures on DSB and SSB (single strand break) production are available. Of particular interest is whether ^{123}I is as effective in producing DSB's and SSB's as ^{125}I i.e. the energy deposition from ^{125}I is so high that there is saturation, or whether a reduction in the effectiveness occurs which is in proportion to the mean local energy deposition.

For the radioisotopes ^{55}Fe and ^{64}Cu the situation

is less clear. The 2 radioisotopes are present somewhere in the cell nucleus, probably randomly distributed with respect to the DNA unless some chemical complex is formed. The considerably smaller local energy deposition of these radionuclides plus their indirect position of incorporation in relation to the DNA sensitive target volume would imply a far smaller radiobiological effectiveness of both these isotopes in producing any biological endpoint unless non-radiological effects also play a role. The high radiotoxicity of ^{64}Cu found by Apelgot' et al is not to be explained by microdosimetry but must be in part supplemented by some chemical effect.

The choice of radionuclides presented in this thesis was orientated towards current work under discussion in radiation biology and medicine and does not in any way represent a limitation in the applicability of the technique. A continuation and development of this work together with more experimental data could lead to a far better understanding of incorporated radionuclide toxicity, the role of the Auger effect in this toxicity and ultimately to potential benefits in the application of Auger emitters to nuclear medicine.

In part II a computer code was developed to calculate from the element cross sections the photoelectric, Compton and total absorption coefficients for biological media in the range of photon energies between 100 eV - 1 MeV. This programme was used to analyse the magnitude of selective absorption at the K photoelectric absorption edge of both phosphorus and iodine in the DNA and as a constituent of the DNA in a cell nucleus. Jump ratios at the K edge of phosphorus of 1.81, for phosphorus in the DNA and 1.15 for a 2.64% weight percentage of phosphorus in the cell nucleus were obtained. For incorporated iodine in the DNA as a selective target in the cell nucleus, under the optimal conditions of 100% replacement of thymidine by IUdR, a more substantial selective absorption could be obtained than for phosphorus (a jump ratio of 1.60 is possible at the iodine K edge). However, this value represents a theoretical maximum by this incorporation method

and must be reduced according to the percentage weight of actual iodine present in the nucleus. Selective absorption is therefore increased the higher the relative weight percentage of the target element in the medium and the higher the atomic number of the target atom.

Even under the condition of low selective absorption in the target element i.e. small jump ratio, an element of atomic number higher than that of the usual constituent elements of biological material i.e. hydrogen, carbon, nitrogen and oxygen, may produce an inhomogeneity in the local absorbed dose which for atoms present in a critical sensitive biological structure, e.g. phosphorus in the DNA, could be sufficient to cause effective damage to the cell. For this reason a detailed study of photoelectric interactions in phosphorus was undertaken in which photoelectric interactions and the ensuing vacancy cascades were simulated for different incident photon energies above and below the K edge of phosphorus using a Monte-Carlo computer code. In this way electron spectra could be generated and then used to calculate the local energy imparted as a function of photon energy and site diameter in spherical volumes containing a homogeneous distribution of phosphorus atoms. The results of this work show that for the photon energies studied (from 278 eV - 4.55 keV) practically the entire incident photon energy is absorbed within a site diameter of 10 μm. Going to small site sizes below 10 nm, the mean energy deposition becomes about twice as great for photon energies above the K edge of phosphorus than for photon energies below.

Monte-Carlo calculations were also performed to simulate photoelectric interactions in argon, a gas which can be used as a good simulant of phosphorus for experimental microdosimetric studies of the energy deposition following photoelectric interactions at different photon energies. Calculated values are given for the mean energy deposition for a homogeneous distribution of argon atoms in a spherical volume of variable diameter irradiated with monochromatic photons of different energy. In addition the electron number distribution for argon irradiated

above and below the K edge compare to the experimentally measured distributions of Carlson and Krause with good agreement providing important confirmation of the theoretical approach.

Part III of this dissertation was concerned with experimental energy deposition measurements for low energy photons where the aim of the study was to measure the effect on the local energy deposition in an argon filled proportional counter of photon interactions of energies just above and below the K edge of argon. With the assumption that the de-excitation processes in argon following photoelectric interactions resemble those in phosphorus, any result obtained would have direct bearing on the energy deposition in a cell from photoelectric interactions in the phosphorus of DNA.

After a detailed description of the experimental method going through the individual system components, the experimental set-up and execution of the measurement, the results of energy deposition measurements are presented for the photon energies : 2.63 keV, 3.34 keV, 4.125 keV and 12.087 keV in a cylindrical counter at simulated tissue equivalent diameters of between 0.5 μm - 8 μm. The mean energy deposition $\bar{\epsilon}_F$ obtained at all simulated counter diameters, for which the measurement technique is applicable, yields values close to the calculated mean electron energy released as a result of photoelectric interactions in argon. This leads to the conclusion that if the sensitive biological target is of cellular dimensions then the radiobiological effect per photon interaction would be expected to be approximately proportional to the incident photon energy, (at least for photon energies between 2.6 keV and 5 keV). If from biological investigations this is not experimentally shown to be the case, and there is evidence that it is not so (Goodhead et al), than one would suspect that the critical target size is smaller than that for which the experimental technique can be applied.

Finally it has been shown, from energy spectra measurements with a spherical Rossi counter employing a

helix electrode to maintain cylindrical field uniformity around the central counting wire, that spurious peaks can arise leading to a serious distortion of the spectrum. It could be verified that the anomalous operation of the counter was connected with the presence of the helix electrode, whether applied with a potential or not, by performing a series of measurements with and without the helix present. It is the view of the author that the anomalous peaks are the result of self-induced space charge effects produced by the presence of the helix. The author would therefore like to see a further investigation of this effect and the scrutinizing of previously performed measurements with helix containing Rossi counters for the presence or absence of space charge effects often disguised in spectra of partial energy deposition and by the art of spectra representation.

REFERENCES

Alper T., Cellular Radiobiology. Cambridge University Press, 1979

Altman P.L. & Katz D.D. Eds., Cell Biology: Biological Handbooks. Federation of American Societies for Experimental Biology, Bethesda, Maryland, pp 363 - 400, 1976

Apelgot S. & Adloff J.D., Transmutation Effects of ^{32}P and ^{33}P Incorporated in DNA. Curr.Top.Radiat.Res. 13, pp 61 - 95, 1978

Apelgot S., Coppey J., Grisvard J., Guille E., Plissonier M., Sissoeff I., Effet Lethal de la Desintegration de ^{64}Cu Incorpore dans des Cellules de Mammiferes. Proc.7th Symp. Microdosimetry, Oxford/UK, Booz J., Ebert H.G. & Hartfiel H.D. Eds., Vol.II, pp 999 - 1011, 1980

Asaad W.N. & Burhop H.S., The K Auger Spectrum. Proc. Phys. Soc. 71, Pt.1, No.457, pp 369 - 382, 1958

Auger P., Sur les Rayons β Secondaires Produit dans un Gaz par des Rayons X. Comptes Rendus 180, pp 65 - 68, 1925

Bambynek W., Behrens H., Chen M.H., Crasemann B., Fitzpatrick M.L., Ledingham K.W.D., Genz H., Mutterer M. & Intemann R.L., Orbital Electron Capture by the Nucleus, Rev. Mod.Phys. 49, No.1, 1977

Band I.N., Kharitonov Y.I. & Trzaskoskaya M.B., Photoionization Cross Sections and Photoelectric Angular Distributions for X-ray Line Energies in the Range 0.132 - 4.509 keV. Targets $1 \leq Z \leq 100$. At.Dat.Nuc. Tables 23, pp 443 - 505, 1979

Bandekar J. & Sathyanarayana B.K., Copper (II) - Nucleic Acid Interactions - A Conformational Study. J.Theor.Biol. 79, pp 443 - 454, 1979

Bearden I.A. & Burr A.F., Reevaluation of X-ray Atomic Energy Levels. Rev.Mod.Phys. 19, No.1, pp 125 - 142, 1967

Behrens H. & Jänecke J., Numerical Tables for Beta Decay and Electron Capture. Landolf-Görnstein, Vol.4, Springer Verlag, 1969

Berger M.J., Some New Transport Calculations of the Deposition Energy in Biological Materials of Low Energy Electrons. Proc. 4th Symp. Microdosimetry, Booz J., Ebert H.G., Eikel R. & Waker A., Eds., EUR 5122, Commission of the European Communities, Luxembourg, pp 695 - 715, 1974

Berger M.J., Improved Point Kernels for Electron and Beta-Ray Dosimetry. NBSIR 73 - 107, Progress Report, 1973

Bertin E.P., Introduction to X-ray Spectrometric Analysis, Plenum Press, New York, p 24 & pp 128 - 132, 1978

Bevan J.S., Parameters Describing the Microdosimetric Distribution of Radiation Dose. Phys.Med.Biol. Vol. 11, No. 3, pp 405 - 409, 1966

Birkhoff R.D., Turner J.E., Anderson V.E., Feolo J.M. & Hamm R.N. The determination of LET Spectra from Energy - Proportional Pulse-Height Measurements I. Track-Length Distributions in Cavities. Health Phys.Pergamon Press, Vol. 18, pp 1 - 14, 1970

Booz J., Microdosimetric Spectra and Parameters of Low LET-Radiations. Proc. 5th Symp. Microdosimetry, Report No. EUR-5452, Booz J., Ebert H.G. & Smith B.G.R. Eds., Commission of the European Communities, Luxemburg, pp 311 - 345, 1976

Booz J., Humm J., Charlton D.E, Pomplun E. & Feinendegen L.E., Microdosimetry of the Auger Effect ; The Biological Significance of Auger-Electron Cascades of Phosphorus after Low Energy Photon Interaction with DNA. Radiation Protection, Proc. 8th Symp. Microdosimetry. Commission of the European Communities Report EUR-8395 EN. Booz J. & Ebert H.G. Eds., pp 625 - 638, 1982

Bruining H., Physics and Applications of Secondary Electron Emission. Pergamon Press, London, 1954

Burki H.J., Roots R., Feinendegen L.E. & Bond V.P., Inactivation of Mammalian Cells after Disintegration of ^{3}H or ^{125}I in Cell DNA at - 196°C. Int. J. Radiat.Biol. 24, pp 365 - 375, 1973

Campion P.J., Some Comments on the Operation of Proportional Counters. 2nd Symp. Microdosimetry, Stresa (Italy) Commission of the European Communities Report EUR-4810, Ebert H.G., Ed., pp 601 - 617, 1971

Campion P.J., The Operation of Proportional Counters at Low Pressures for Microdosimetry. Phys.Med.Biol. Vol. 16, No. 4, pp 611 - 616, 1971

Carlson T.A., The Nature of Secondary Electrons Created as the Results of Electron Shake-off and Vacancy Cascades. Rad.Res. 64, pp 53 - 69, 1975a

Carlson T.A., Photoelectric and Auger Spectroscopy. Plenum Press, 1975b

Carlson T.A. & Krause M.O., Experimental Evidence for Double Electron Emission in an Auger Process. Phys.Rev. Letters, 14, No. 11, pp 390 - 392, 1965a

Carlson T.A. & Krause M.O., Atomic Readjustment to Vacancies in the K and L Shell of Argon. Phys.Rev. Vol. 137, No. 6A, pp A1655 - A1662, 1965b

Carlson T.A. & Milford White R., Formation of Fragment Ions from CH_3Te^{125} and $C_2H_5Te^{125}$ following the Nuclear Decays of CH_3I^{125} and $C_2H_5I^{125}$. J.Chem.Phys. 38, No. 12, pp 2930 - 2934, 1963

Carlson T.A. & White R.M., Measurement of the Relative Abundances and Recoil-Energy Spectra of Fragment Ions Produced as the Initial Consequences of X-Ray Interaction with CH_3I, HI, and DI. J.Chem.Phys. Vol. 44, No. 12, pp 4510 - 4520, 1966

Casey W.R. & Albridge R.G., The L- and K- Auger Spectra of tellurium. Z.Phys. 219, pp 216 - 226, 1969

Charlton D.E. & Booz J., A Monte-Carlo Treatment of the Decay of I-125. Radiat.Res. 87, pp 10 - 23, 1981

Charlton D.E., Booz J., Fidorra J., Smit Th. & Feinendegen L.E., Microdosimetry of Radioactive Nuclei Incorporated into the DNA of Mammalian Cells. Proc. 6th Symp. Microdosimetry, Brussels/Belgium, Booz J. & Ebert H.G. Eds., Vol.I, pp 91 - 108, 1978

Chen M.H., Crasemann B. & Mark H., Relativistic Radiationless Transition Probabilities for Atomic K and L Shells. At.Nuc.Dat. Tables 24, pp 13 - 37, 1979

Chu Y.Y., Kistner O.C., Li A.C., Monaro S. & Perlman M.L., E2/M1 Ratios in the Isomeric Transitions of Te-121 and Te-123 and the Decay of the Te-121 Isomers to Sb-121, Phys. Rev. 133, No. 6B, pp B1361 - B1367, 1964

Chung M.F. & Jenkins L.H., Auger Electrons Energies of the Outer Shell Electrons. Surf.Sci. 22, pp 479 - 485, 1970

Citrin P.H., Rose J.E. & Christman S.B., Interatomic Auger Transitions in Ionic Compounds. Phys.Rev. B, Vol. 14, No. 6, pp 2642 - 2658, 1976

Coghlan W.A. & Clausing R.E., Auger Catalogue : Calculated Transition Energies Listed by Energy and Element. At. Data 5, pp 317 - 469, 1973

Cooper E.P., On the Separation of Nuclear Isomers. Phys. Rev. 61, pp 1 - 5, 1942

Dekker A.J., Solid State Physics. Mac Millan Press Ltd., London, 1975

Diehn B., Halpern A. & Stocklin G., Specific Inactivation of Bovine Carbonic Anhydrase as the Consequence of X-ray Resonance Absorption in the Constituent of Zinc Atom. J. Am.Chem.Soc. 98, p 1077, 1976

Diethorn W., A Methane Proportional Counter System for Natural Radiocarbon Measurements (Thesis). NYO - 6628, 1956

Dillman L.T. & Van der Lage F.C., Radionuclide Decay Schemes and Nuclear Parameters for Use in Radiation-Dose Estimation. NM/MIRD pamphlet No.10, Soc.Nucl.Medicine, 1975

Dyson R.D., Cell Biology : A Molecular Approach. Allyn & Bacon, Inc. Boston, 1978

Eickel R. & Booz J., Untersuchungen zur Energieübertragung von Röntgen- und Gammastrahlen an biologischen Modellstrukturen, Report Jul-1412, p 31, 1977

Emery G.T., Ionization through Nuclear Electron Capture and Internal Conversion, Chap. 4, pp 201 - 231. Atomic Shell Processes, Crasemann B. Ed. Academic Press, 1975

Ertl H.H. & Feinendegen L.E., Microdosimetry of I-125 with Reference to the Auger Effect. Proc. 2nd Symp. Microdosimetry, Stresa/Italy, EUR 4452, Ebert H.G. Ed., 1969

Ertl H.H., Feinendegen L.E. & Heiniger H.J., Iodine-125, a Tracer in Cell Biology : Physical Properties and Biological Aspects. Phys.Med.Biol. 15, pp 447 - 456, 1970

Evans R.D., The Atomic Nucleus Mc Graw-Hill, 1955

Evans R.D., X-ray and Gamma-ray Interactions, Chap. 3 Radiation Dosimetry, Vol. I, Attix F.H., Roesch W.C. Eds., Academic Press, London, pp 93 - 155, 1968

Fano U., Tables for the Analysis of Beta Spectra. Nat. Bur. Standards App.Math.Ser. 13, p. 61, 1952

Feinendegen L.E., Institut fur Medizin, Kernforschungsanlage, 5170 Julich, F.R.-Germany. Private Communication

Feinendegen L.E. & Cronkite E.P., Effects of Microdistribution of Radionuclides on Recommended Limits in Radiation Protection, A Model. Curr.Top.Radiat.Res. Quarterly 12, pp 83 - 99, 1977

Gavron Y. & Feige A., Microdosimetry of Auger Electrons. Rad.Res. Biomedical, Chemical and Physical Perspectives. Nygaard O.F., Adler H.T. & Sinclar W.K. Eds., pp 557 - 569, Academic Press, 1975

Goodhead D.T., Cox R. & Thacker J., Do Ultrasoft X-rays produce Lesions Characteristic of High LET or Low LET, or Neither? Proc. 7th Symp. Microdosimetry, Oxford/UK, Booz J., Ebert H.G. & Hartfiel H.D. Eds., Vol.II, pp 929 - 942, 1980

Goodhead D.T., Thacker J. & Cox R., Is Selective Absorption of Ultrasoft X-Rays Biologically Important in Mammalian Cells ?, Phys.Med.Biol. 26, No 6, pp 1115 - 1127, 1981

Hager R.S. & Seltzer E.C., Tables of Internal Conversion Coefficients, Nuclear Data A4, p 1, 1968

Halpern A. & Stocklin G., A Radiation Chemical Resonance Effect in Solid 5-Bromodeoxyuridine; Chemical Consequences of the Auger Effect. Rad.Res. 58, pp 329 - 337, 1974

Halpern A. & Stocklin G., Chemical and Biological Consequences of Beta Decay. Part I. Radiat.Environ.Biophys. 14, pp 167 - 183, 1977

Hegeweg B., Microdosimetric Measurements and some Applications in Radiobiology and Radiation Protection. Thesis, University of Amsterdam. W.D.Meinema B.V.-Delft 1978

Hendricks R.W., Space Charge Effects in Proportional Counters. Rev.Sci.Instr. Vol. 40, No. 9, pp 1216 - 1223, 1969

Hofer K.G., Keough G. & Smith T.M., Biological Toxicity of Auger Electrons : Molecular Fragmentation versus Electron Irradiation, Feinendegen L.E., Tisljar-Lentulis G.T. & Ebert H. Eds. Curr.Top.Radiat.Res. Quarterly 12, pp 335 - 354, 1977

Hubbel J.H., Photon Cross Sections, Attenuation Coefficients and Energy Absorption Coefficients from 10 keV to 100 GeV. NSRDS - NBS 29, 1969

Humm J., Pomplun E., Booz J. & Charlton D.E., Energy and Number Distributions of Electrons and Photons Emitted after Photoelectric Interaction of X-Rays with Phosphorus in DNA. Radiation Protection, Proc. 8th Symp. Microdosimetry. Commission of the European Communities Report EUR-8395 EN. Booz J. & Ebert H.G. Eds., pp 625 - 638, 1982

ICRU Report Microdosimetry published 1983

Iskef H. & Watt D.E. A Calorimetry Technique for Measurement of the Stopping Power of Low Energy Electrons (10 keV). Radiation Protection. Proc. 8th Symp. Microdosimetry, Julich. Commission of the European Communities Report EUR-8395 EN. Booz J. & Ebert H.G. Eds. pp 275 - 284, 1983

Kassis A.I., Adelstein S.I., Haydock C., Sastry K.S.R., Mc Elvany K.D. & Welch M.J., Lethality of Auger Electrons from the Decay of Br-77 in the DNA of Mammalian Cells. Rad. Res. 90, pp 362 - 373, 1982

Kellerer A.M., An Assessment of Wall Effects in Microdosimetric Measurements. Rad.Res. 47, pp 377 - 386, 1971

Kellerer A.M., Criteria for the Equivalence of Spherical and Cylindrical Proportional Counters in Microdosimetry. Radiat.Res. 86, pp 277 - 286, 1981

Kellerer A.M. & Rossi H.H., The Theory of Dual Radiation Action. Curr.Top.Rad.Res. Quarterly 8, pp 85 - 158, 1972

Knoll G., Radiation Detection and Measurement. John Wiley & Son, New York, 1979

Krause M.O., Atomic Radiative and Radiationless Yields for K and L Shells, I.Phys.Chem.Ref. Data 8, No. 2, 1979

Krisch R.E., Lethal Effects of I-125 Decay by Electron Capture in E.Coli and Bacteriophage T1. Int.J.Radiat.Biol. 21, pp 167 - 189, 1972

Krisch R.E., Krasin F. & Sauri C.J., DNA Breakage, Repair and Lethality after I-125 Decay in rec^{+} and rec A Strains of E.Coli. Int.J.Radiat.Biol. 29, No. 1, pp 37 - 50, 1976

Kronberg A., DNA Synthesis. Freeman W.H. & Co, 1974

Larkins F.P., Theory of Multiple Ionization Processes. Proceedings of the International Conference on Inner Shell Ionization Phenomena and Future Applications, Conf-720404. Vol. 2, pp 1543 - 1571, 1972

Learmonth G.P. & Lewis P.A.W., Naval Graduate School Random Number Generator Package LLRANDOM, NPSSSL W73061A, Naval Graduate School, Monterey, California, 1973

Lederer C.M. & Shirley V.S. Eds. Table of Isotopes 7th Edition. Wiley & Sons, 1978

Mantel J., The Beta Ray Spectrum and the Average Beta Energy of Several Isotopes of Interest in Medicine and Biology. Int.J.App.Radiat. Isotopes, Vol. 23, pp 407 - 413, Pergamon Press, 1972

Marmier P., Kernphysik 1. VMP Verlag, 1965

Marschall J.H., How to Figure Shapes of Beta-Ray Spectra, Nucleonics, pp 34 - 38, Aug. 1955

Martin R.F. & Haseltine W.A., Range of Radiochemical Damage to DNA with Decay of Iodine-125. Science 213, pp 896 - 898, 1981

Mc Guire E.I., Auger and Coster-Kronig Transitions. Atomic Inner-Shell Processes, Crasemann B. Ed. Vol. 1, Academic Press, pp 293 - 327, 1975

Mc Guire E.I., L-Shell Auger, Coster-Kronig and Radiative Matrix Elements, and Auger and Coster-Kronig Transitions Rates in j-j Coupling. Report No. SC-RR-71-0075, Sandia Labs. 1977

Mc Guire E.I., M-Shell Auger, Coster-Kronig and Radiative Matrix Elements, and Auger and Coster-Kronig Transitions Rates in j-j Coupling. Report No. SC-RR-71-0835, Sandia Labs. 1972

Mc Guire E.I., N-Shell Auger, Coster-Kronig and Radiative Matrix Elements, and Auger and Coster-Kronig Transitions Rates in j-j Coupling. Report No. SS-RR-75-0443, Sandia Labs. 1975

Mehard C.W. & Volcani B.E., Silicon in Rat Liver Organelles : Electron Probe Microanalysis, Cell Tiss.Res. 166, pp 255 - 263, 1976

Proceedings of the International Conference on Inner Shell Ionization Phenomena and Future Applications Vols 1 - 3, Crasemann B. Ed., Conf-720404. United States Atomic Energy Commission, Oak Ridge, Tennesee, 1972

Reincke U., Brookoff D., Burlington H., Cronkite E.P., Pappas N. & Zanjani E., Susceptibility of Hematopoietic Stem Cells (CFU-s) to Fe-55 Radiation Damage. Rad.Res. 74, pp 66 - 78, 1978

Reincke U., Burlington H., Cronkite E.P., Hillman M. & Laissue J., Selective Damage to Erythoblasts by Fe-55. Blood 45, pp 801 - 810, 1975

Rösel F., Fries H.M., Adler K. & Pauli H.C., Internal Conversion Coefficients for all Atomic Shells. At.Data & Nucl. Data Tables 21, pp 91 - 289, 1978

Rossi H.H., Microscopic Energy Distribution in Irradiated Matter. Radiation Dosimetry. Attix F.H. & Roesch W.C. Eds., Academic Press London, pp 43 - 92, 1968

Rossi H.H. & Rosenzweig W., A Device for the Measurement of Dose as a Function of Specific Ionization. Radiobiology 64, pp 404 - 411, 1955

Salem S.I., Panossian S.L. & Krause R.A., Experimental K and L Relative X-ray Emission Rates. At.Dat.Nuc.Dat. Tables 14, pp 91 - 109, 1974

Scofield J.H., Theoretical Photoionization Cross Sections from 1 to 1500 keV. UCRL - 51326, 1973

Segre E. & Helmholz A.C., Nuclear Isomerism, Rev.Mod.Phys. 21, No. 2, pp 271 - 304, 1949

Sevier K.D., Atomic Electron Binding Energies. At.Dat.Nuc. Dat. Tables 24, pp 323 - 371, 1979

Sevier K.D., Low Energy Electron Spectroscopy. Wiley Interscience, 1972

Shreider Yu.A. Ed., The Monte Carlo Method. Pergamon Press, 1966

Srdoc D., Experimental Technique of Measurement of Microdosimetric Energy Distribution in Irradiated Matter using Rossi Counters. Rad.Res. 43, pp 302 - 319, 1970

Storm E. & Israel H.I., Photon Cross Section from 1 keV to 100 MeV for Elements Z = 1 to Z = 100. Nuc. Data Tables A7, pp 565 - 681, 1970

Veigele W.M., Photon Cross Sections from 0.1 keV to 1 MeV for Elements Z = 1 to Z = 94. At.Dat. Tables 5, pp 51 - 111, 1973

Weast R.C. Ed., Handbook of Physics and Chemistry. 61st Edition, CRC Press, Inc. Boca Raton, Florida 33431, p E-69, 1980 - 81

Wexler S., Primary Physical and Chemical Effects associated with the Emission of Radiation in Nuclear Processes. Actions Chimiques et Biologiques des Radiations. Haissinsky M. Ed., pp 105 - 241, Masson, Paris, 1965

White-Grodstein G., X-ray Attenuation Coefficients from 10 keV to 100 MeV. NBS Circ. 583, 1957

Wilson B.T. Ed., The Radiochemical Manual. The Radiochemical Centre, Amersham, 1966

ACKNOWLEDGEMENTS

I would greatly like to thank my two supervisors: Dr.J.Booz from the Institut für Medizin, Kernforschungsanlage, Jülich and Dr.A.K.M.M.Haque, Polytechnic of the South Bank, London and also Prof.D.E.Charlton, Concordia University, Montreal for their persistant help, support and encouragement. I am especially indebted to Prof.L.E. Feinendegen for allowing me to perform this work in the Institut für Medizin and for his continual and stimulating interest in the progress of this work, and also to the Commission of the European Communities for financial support. I am indebted to Prof.G.Stöcklin and Dr.A.Halpern from the Institut für Chemie 1, Julich for allowing me to use their X-ray equipment.

Further thanks to Mr.T.Smit, Mr.R.Schlenter and Mr.D.Barthmann for their invaluable technical assistance, Dr.J.Fidorra for patient discussions on some of the problems and Mr.J.Knieper for his help on the radiation protection monitoring.

Finally a warm thanks for the continual support of my wife, Emilia, and for typing the manuscript.

Appendix 1

The shape of beta spectra

The formula for the shape of a beta spectrum is given by equation 1 (part I section 1.2). The sense in which a beta spectrum is required here is as input data for a Monte-Carlo programme which calculates the electron emission spectrum for individual decays of the isotope ^{64}Cu. For this purpose the spectrum has been divided up into 10 energy intervals of 60 keV width and the relative number of beta particles in each energy interval calculated with equation 1.

For the values of the Fermi function F(Z,W-V), Fano 1952, Z equals 28 for beta-plus decay and 30 for beta-minus decay. These values of Z then yield for V_0 , where $V_0 = 1.13\,\alpha^2|Z|^{4/3}$ the values 0.0051 for beta-plus decay and 0.0056 for beta-minus decay (mc^2 units). The steps in the calculation of the shape of the beta-plus spectrum are given in table 1a.

Table 1a
Calculation of the beta-plus spectrum

E(keV)	Mid.point	W	$(W-V_0)-1^2$	$(W-V_0).(W_0-W)^2$	$F(28,W-V_0)$	N(E)E
0- 60	30	1.0587	.332	1.577	.008	.004
60-120	90	1.1761	.609	1.432	.088	.077
120-180	150	1.2935	.812	1.259	.208	.213
180-240	210	1.4110	.988	1.067	.350	.369
240-300	270	1.528	1.149	.866	.510	.507
300-360	330	1.646	1.301	.664	.683	.590
360-420	390	1.763	1.446	.474	.873	.598
420-480	450	1.881	1.587	.302	1.075	.515
480-540	510	1.998	1.724	.161	1.292	.359
540-600	570	2.117	1.860	.004	1.522	.011
						3.243

The values N(W)dW are normalized so that $\sum_{0}^{600keV} N(W)dW$ is equal to the probability of beta decay (0.193), Dillmann and Van der Lage 1975.

The beta-minus spectrum is split up in the same way and normalized to 0.396, the probability for beta-minus decay. The two normalized fractions for beta-plus and beta-minus decay are added since for energy deposition purposes the charge difference can be neglected.

Table 1b
Relative intensities of the beta-plus, beta-minus spectra

E(keV)	$N_p(E)dE$	$N_e(E)dE$	$N_p(E)+N_e(E)dE$
0- 60	.0002	.0081	.0083
60-120	.0046	.0278	.0324
120-180	.0127	.0486	.0613
180-240	.0220	.0588	.0808
240-300	.0302	.0765	.1067
300-360	.0350	.0717	.1067
360-420	.0356	.0561	.1117
420-480	.0306	.0360	.0666
480-540	.0214	.0124	.0338
540-600	.0007	-	.0007
	.193	.396	.589

The relative intensities of the combined beta spectrum in column 4 of the table 1b are now in a convenient form as input data for the Monte-Carlo calculations, (see part I section 4.2).

Appendix 2

A given inner shell vacancy can usually be filled by a series of Auger transitions. The notation used to characterize individual Auger transitions is similar to that used for photon transitions in X-ray spectroscopy. For example, the Auger transition KL_1L_3 denotes an electron transition from L_1 to K with the emission of an electron from L_3. From the three sub-shell symbols the first gives the initial vacancy, the second the electron

shell from which the vacancy is filled and the third the shell from which an electron is released, the so called Auger electron.

Appendix 3

Table 3a
Electron transition probability and energy data
tellurium

Transition	p	E(keV)	Transition	p	E(keV)
1 3 0	.224	27.2	2 6 0	.0100	4.07
1 4 0	.456	27.5	2 7 0	.0160	4.12
1 6 0	.045	30.9	2 12 0	.0037	4.83
1 7 0	.087	31.0	2 3 10	.0382	.122
1 11 0	.013	31.7	2 3 11	.0302	.172
1 12 0	.014	31.7	2 3 12	.0477	.182
1 2 2	.0095	21.8	2 3 13	.0137	.264
1 2 3	.0154	22.1	2 3 14	.0249	.265
1 2 4	.0181	22.4	2 3 15	.0042	.302
1 2 5	.0038	25.8	2 3 16	.0028	.314
1 2 6	.0030	25.9	2 3 17	.0042	.315
1 2 7	.0025	26.0	2 4 10	.0658	.392
1 2 8	.0007	26.2	2 4 11	.0264	.441
1 2 9	.0007	26.2	2 4 12	.0658	.453
1 2 10	.0008	26.8	2 4 13	.0676	.533
1 2 11	.0008	26.8	2 4 14	.0875	.535
1 2 12	.0009	26.8	2 4 15	.0052	.572
1 3 4	.0359	22.7	2 4 16	.0017	.581
1 3 5	.0021	26.1	2 5 5	.0100	2.88
1 3 6	.0022	26.3	2 5 6	.0124	2.99
1 3 7	.0022	26.3	2 5 7	.1161	3.12
1 3 8	.0033	26.6	2 5 8	.0003	3.30
1 3 9	.0033	26.6	2 5 9	.0329	3.30
1 3 10	.0001	27.1	2 5 10	.0057	3.75
1 3 11	.0001	27.1	2 5 11	.0047	3.80
1 3 12	.0001	27.1	2 5 12	.0048	3.80
1 4 4	.0142	23.0	2 6 6	.0002	3.14
1 4 5	.0026	26.4	2 6 8	.0030	3.44
1 4 6	.0036	26.6	2 6 9	.0734	3.44
1 4 7	.0037	26.6	2 6 10	.0203	3.86
1 4 8	.0010	26.9	2 7 10	.0588	3.96
1 4 9	.0009	26.9	2 7 11	.0024	3.96
1 4 10	.0008	27.4	2 7 12	.0025	3.96
1 4 11	.0008	27.4	2 8 8	.0322	3.73
1 4 12	.0008	27.4	2 8 9	.0601	3.73
1 4 13	.0002	27.4	2 9 9	.0431	3.75
1 7 12	.0060	31.0			
	1.000			1.000	

Table 3a gives as an example the electron transition probability data-set to the K and L_1 shells of tellurium following either ^{125}I or ^{123}I decay. The terminology is as follows. The first three integers denote the transition where the number 1 represents the K shell, 2 the L_1 shell, 3 the L_2 shell and so on until 15 denoting the outermost O_3 shell of tellurium. Using this terminology a transition from L_3 to K with an electron ejected from M_1 would be represented by 1 4 5. Photon transitions are characterized by a zero in the third column. The fourth column gives the relative probability of the transition and the fifth the energy of the emitted photon or electron.

Appendix 4

Flow chart of the computer code

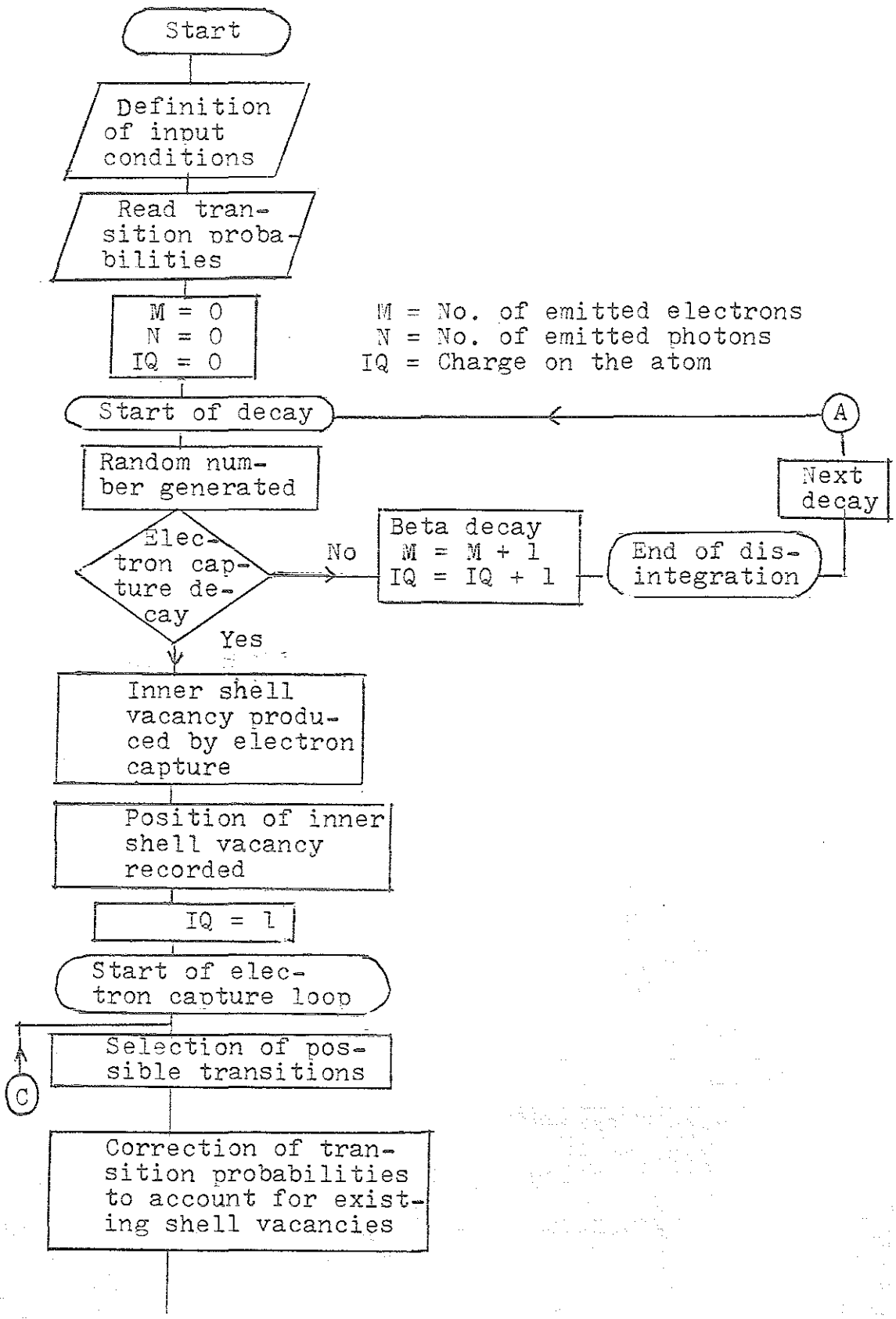

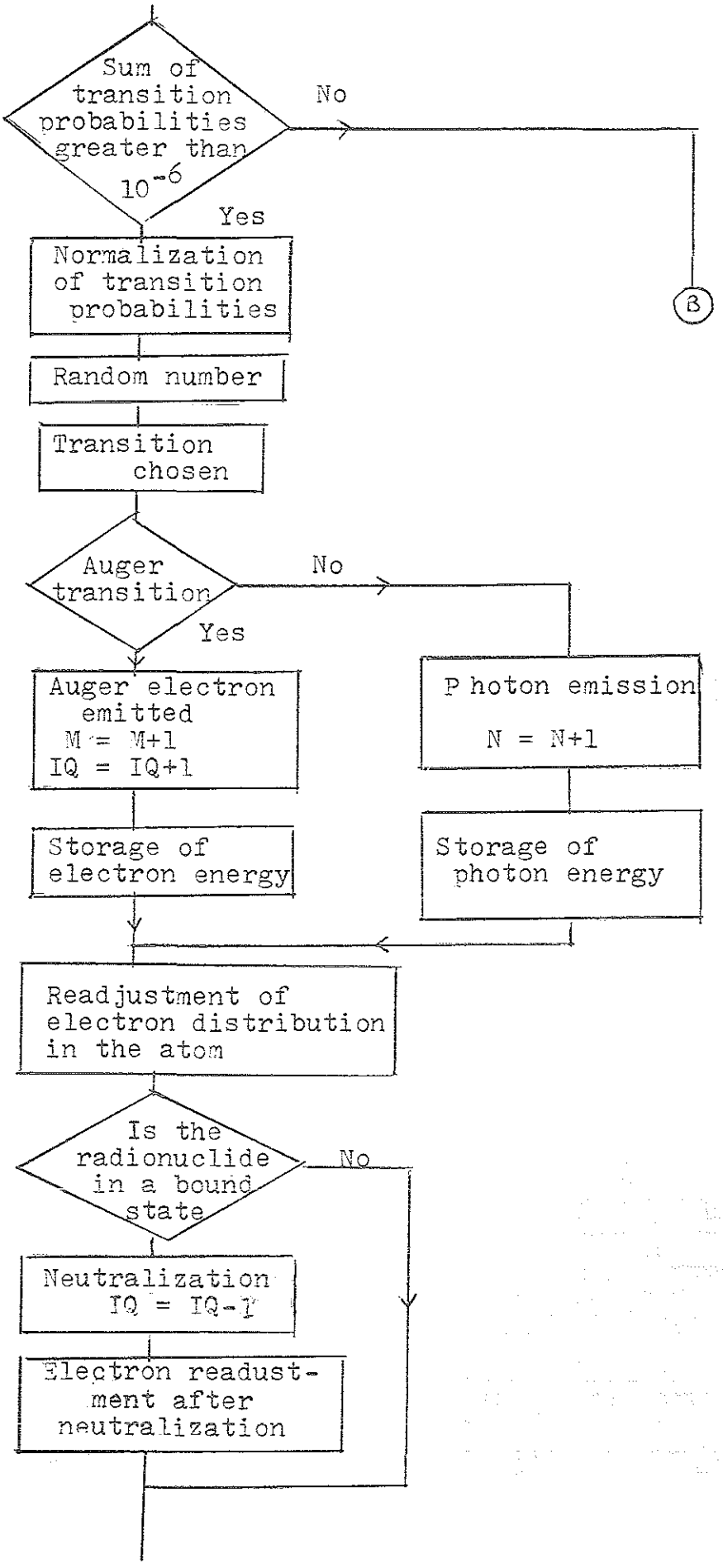
Sum of transition probabilities greater than 10^{-6}
No
Yes
Normalization of transition probabilities
B
Random number
Transition chosen
Auger transition
No
Yes
Auger electron emitted
M = M+1
IQ = IQ+1
Photon emission
N = N+1
Storage of electron energy
Storage of photon energy
Readjustment of electron distribution in the atom
Is the radionuclide in a bound state
No
Neutralization
IQ = IQ-1
Electron readjustment after neutralization

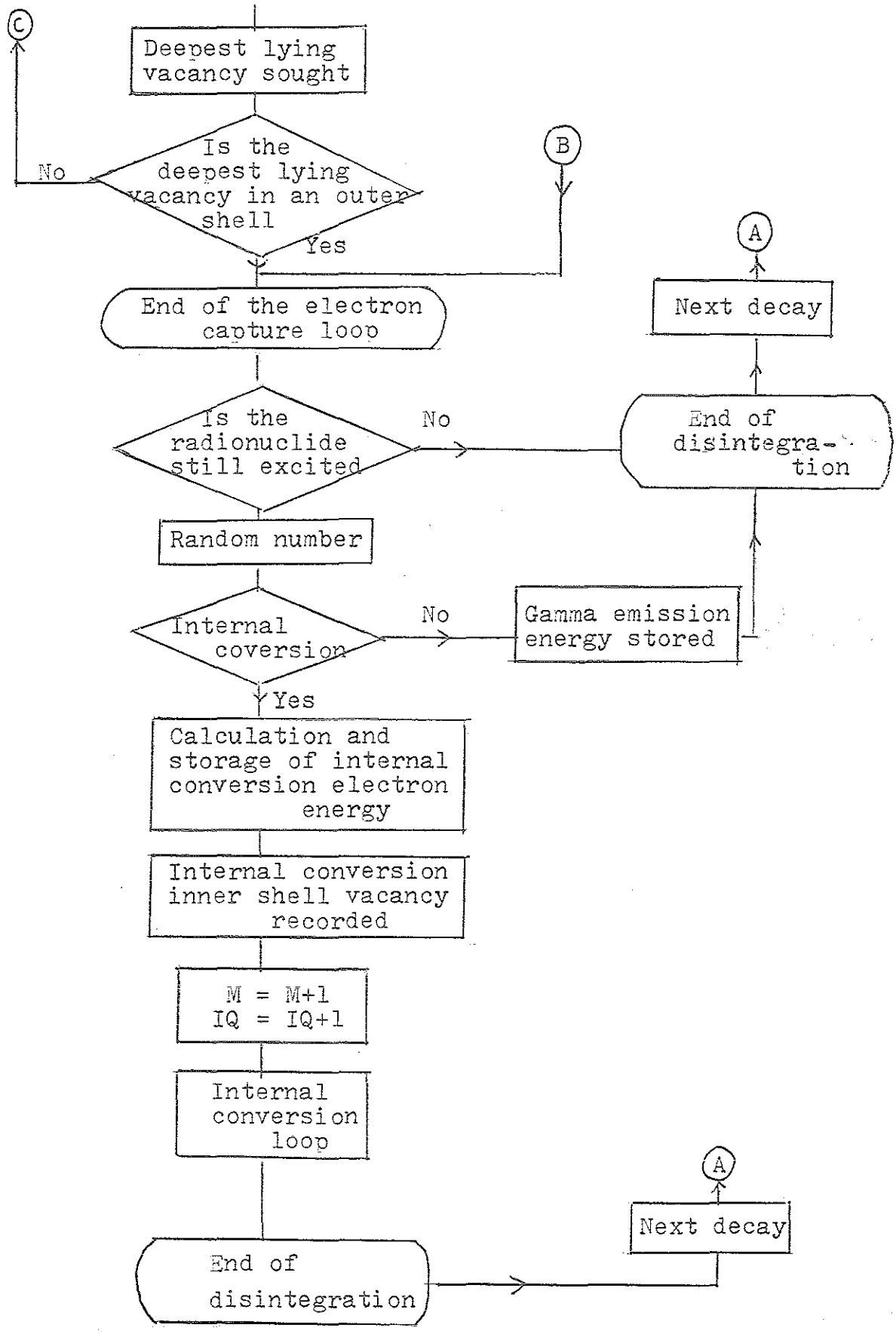
C
Deepest lying vacancy sought
Is the deepest lying vacancy in an outer shell
No
Yes
B
End of the electron capture loop
Is the radionuclide still excited
No
A
Next decay
End of disintegra-tion
Random number
Internal coversion
No
Gamma emission energy stored
Yes
Calculation and storage of internal conversion electron energy
Internal conversion inner shell vacancy recorded
M = M+1
IQ = IQ+1
Internal conversion loop
A
Next decay
End of disintegration

Appendix 5

Photoelectric interactions in the iodine of CH_3I

Following the decay of CH_3I^{125} the charge distribution on the tellurium atom is greatly smeared out by the statistical processes of the second cascade. Calculations of a single cascade process such as after photoelectric interactions in cold iodine would be therefore a more reliable test of the computational method.

Carlson and White 1966 irradiated CH_3I with 8 keV X-rays, i.e. just above the L_1 edge, and measured the charge distribution on the iodine as well as on the molecular fragments after the Coulomb explosion. Figure 5a compares their results for the charge distribution on the iodine with those of Monte-Carlo calculations simulating an 8 keV photoelectric interaction in the iodine of CH_3I and the thereby induced vacancy cascade. Again agreement is good with the experimental results. The calculations give a peak at 4, Carlson and White at 5. In the high and low charge regions between 1-3 and 5-10 agreement is excellent, the largest discrepency being around the peak values. Further agreement was obtained also with regard to the charge on the fragmented ligand, i.e. the number of neutralization electrons employed.

Both this result and that for CH_3I^{125} demonstrate that the number of electrons emitted as well as the number of active neutralization electrons is consistant with experiment for single and double cascade processes.

Figure 5a

Charge distribution on the iodine atom after an 8 keV photoelectric interaction with CH_3I. Comparison of the Monte-Carlo calculations with the experimental values of Carlson.

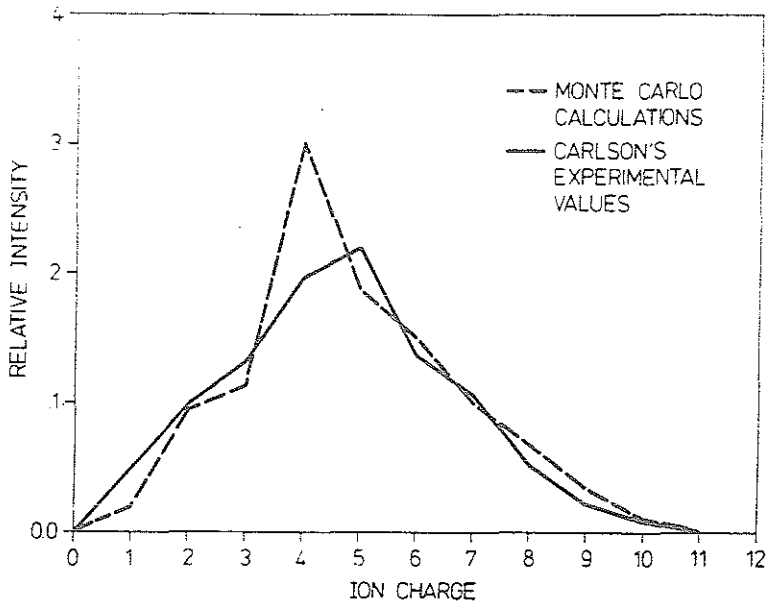

Appendix 6

Table 6a

Transition probability data and energy data for radiative and non-radiative transitions in phosphorus as used in these calculations.

Transition	Transition Probability	Energy (keV)
1 3 0	.019	1.991
1 4 0	.038	1.992
1 6 0	.001	2.122
1 7 0	.002	2.122
1 2 2	.0392	1.716
1 2 3	.1257	1.767
1 2 4	.1251	1.768
1 3 3	.1500	1.818
1 3 4	.2988	1.819
1 4 4	.1500	1.820
1 2 6	.0026	1.914
1 2 7	.0026	1.914
1 3 5	.0116	1.955
1 4 5	.0116	1.956
1 3 6	.0057	1.965
1 3 7	.0057	1.965
1 4 6	.0057	1.966
1 4 7	.0057	1.966
2 3 5	.3330	0.012
2 4 5	.3330	0.013
2 3 6	.0760	0.022
2 3 7	.0760	0.022
2 4 6	.0760	0.023
2 4 7	.0760	0.023
2 5 5	.0080	0.149
2 5 6	.0100	0.159
2 5 7	.0100	0.159
2 6 6	.0010	0.169
2 6 7	.0010	0.169
3 5 5	.0410	0.101
3 5 6	.1970	0.111
3 5 7	.1970	0.111
3 6 6	.1880	0.121
3 6 7	.1880	0.121
3 7 7	.1880	0.121
4 5 5	.0410	0.100
4 5 6	.1970	0.110
4 5 7	.1970	0.110
4 6 6	.1880	0.120
4 6 7	.1880	0.120
4 7 7	.1880	0.120